PHOTOVOLTAIC CELLS EMPLOYING POLYCRYSTALLINE AND SINGLE CRYSTAL CADMIUM SELENIDE/POLYSULFIDE LIQUID JUNCTIONS

by

Silvia Annelise Wessel

B.Sc. (Honours), Simon Fraser University, 1980

THESIS SUBMITTED IN PARTIAL FULFILLMENT OF

THE REQUIREMENTS FOR THE DEGREE OF

DOCTOR OF PHILOSOPHY

in the Department

of

Physics

SIMON FRASER UNIVERSITY

August, 1985

APPROVAL

Name: Silvia Annelise Wessel

Degree: Doctor of Philosophy

Title of thesis: Photovoltaic Cells Employing Polycrystalline and Single Crystal Cadmium Selenide/Polysulfide Liquid Junctions

Examining Committee:

Chairman: B. P. Clayman

K. Colbow
Senior Supervisor

J. C. Irwin

R. F. Frindt

S. R. Morrison

A. Heller
External Examiner
AT&T Bell Labs, New Jersey

Date Approved: 9. August 1985

PARTIAL COPYRIGHT LICENSE

I hereby grant to Simon Fraser University the right to lend my thesis, project or extended essay (the title of which is shown below) to users of the Simon Fraser University Library, and to make partial or single copies only for such users or in response to a request from the library of any other university, or other educational institution, on its own behalf or for one of its users. I further agree that permission for multiple copying of this work for scholarly purposes may be granted by me or the Dean of Graduate Studies. It is understood that copying or publication of this work for financial gain shall not be allowed without my written permission.

Title of Thesis/Project/Extended Essay

PHOTOVOLTAIC CELLS EMPLOYING POLYCRYSTALLINE AND SINGLE CRYSTAL CADMIUM SELENIDE/POLYSULFIDE LIQUID JUNCTIONS

Author:

(signature)

SILVIA ANNELISE WESSEL

(name)

19. August 1985

(date)

Abstract

The solar performance of electroplated, cold pressed and single crystal cadmium selenide/aqueous polysulfide photo-electrochemical solar cells was investigated by means of current-voltage characteristics, quantum efficiency-voltage dependence, and spectral response.

The electroplated cadmium selenide films of 10±2 μm thickness were deposited on titanium substrates by electrodeposition using an acid solution of cadmium sulfate, selenium dioxide and sulphuric acid. Etching and annealing of the electroplated films improved the solar performance considerably. The surface morphology revealed a "cauliflower" structure with small crystallites. Some microcracks were also observed after annealing.

Cold pressing of cadmium selenide powder was investigated as a technique for producing inexpensive, self-supporting photoanodes. Physical properties such as density, resistivity and surface morphology were determined and related to solar cell performance. Pellets pressed at higher pressures showed larger crystallites and improved quantum efficiency; pressures above 69 MPa produced fractures in the pellets. Pellets pressed at 46 MPa for 5 min were annealed at various temperatures. Annealing at 873 K for six hours revealed optimum solar performance.

Since single crystals of cadmium selenide often show poor solar response, the effect of annealing was investigated.

Annealing in cadmium atmosphere improved the overall solar response considerably, while annealing under vacuum produced a poor response for photon energies higher than 1.8 eV and high quantum efficiencies for near bandgap energies. Annealing in a selenium atmosphere resulted in very poor solar response. Simultaneous illumination of the electrodes with a helium-neon laser strongly enhanced the quantum efficiency for vacuum annealed crystals for near bandgap photons.

Surface treatments of cadmium selenide photoanodes may passivate grain boundaries and redistribute surface state energies. Dipping or boiling of pressed and electroplated samples in zinc chloride solution improved the open circuit voltage considerably. In contrast, electrodes dipped in mercuric chloride solution produced a deterioration in solar performance.

Dedicated to Hermann and Ilse Wessel, my parents.

ACKNOWLEDGEMENTS

I wish to thank Dr. K. Colbow for his encouragement and technical and financial support. My special thanks go to Alec Mackintosh who helped in many aspects of this work and spent many evenings in the darkroom developing and printing the figures. I sincerely thank Sara Swenson for editing and correcting the grammar. I would like to thank the secretarial and technical staff of the Physics and Chemistry departments and the personel in the machine, glass-blowing and electronics workshops for their assistance. I thank Dr. B. Heinrich for the SAM data and Monica Nasmyth of Cominco Ltd. for the emission spectroscopic analysis. I would like to thank Dr. J.C. Irwin and Dr. R.F. Frindt for their suggestions and advice, Dr. F. El Guibaly and Dr. S.R. Morrison for the helpful discussions, and Dr. A. Heller from AT&T Bell Labs for acting as my external examiner.

This work was supported by a grant from the B. C. Science Council and the Natural Science and Engineering Research Council. The financial support through scholarships from the Natural Science and Engineering Research Council and Simon Fraser University were very much appreciated.

TABLE OF CONTENTS

Approval ii

Abstract iii

Dedication v

Acknowledgements vi

List of Tables ix

List of Figures..... x

1. Introduction 1

    1.1 Object of research and structure of thesis 6

2. The electrochemical photovoltaic cell 9

    2.1 Principles and energetics 9

    2.2 Efficiency 18

    2.3 Stability 25

    2.4 Surface states 27

    2.5 The mathematical model 30

3. Cadmium Selenide Electrochemical Photovoltaic Cells ... 57

    3.1 Physical and chemical properties of CdSe 58

    3.2 Preparation techniques 59

    3.3 Redox couple electrolytes 64

    3.4 The CdSe/polysulfide electrolyte system 66

        3.4.1 Stability 66

        3.4.2 Surface etching 72

        3.4.3 Specific ion adsorption 74

        3.4.4 Lifetime 76

4. Materials and Methods 83

4.1 Electrodeposited CdSe electrodes 83

4.2 Cold pressed CdSe electrodes 86

4.3 Single crystal CdSe electrodes 87

4.4 Treatment of CdSe electrodes with Zn^{2+} and Hg^{2+} solutions 89

4.5 The test cell 89

4.6 Current-voltage characteristics 91

4.7 Quantum efficiency-voltage characteristics 91

4.8 Spectral response 92

4.9 Resistivity 93

4.10 Scanning electron micrographs 93

5. Results and Discussion 103

5.1 Electrodeposited CdSe electrodes 103

5.2 Pressure sintered CdSe electrodes 106

5.3 Single crystal CdSe electrodes 110

5.4 Comparison of electrodeposited, pressure sintered and single crystal CdSe electrodes ... 117

5.5 Ion surface treatments 120

6. Summary and Conclusions 158

Appendix A 161

Appendix B 164

Bibliography 167

List of Tables

Table		page
3.1	Flatband potentials and power conversion efficiencies for CdSe electrochemical photovoltaic cells with various aqueous redox couple electrolytes.	79
4.1	Solar performance of CdSe electrodes, electroplated on Ti substrate at various constant negative plating potentials.	94
5.1	The effect of annealing temperature and its duration on the solar performance of CdSe pressed pellet elctrodes.	123
5.2	The effect of pressure and its duration on the solar parameters of pressure sintered electrodes.	124
5.3	The quantum efficiencies at 2.00 eV and the peak response with and without laser pumping for CdSe single crystals with various treatments.	125
5.4	The effect of Zn^{2+} ion surface treatments on the solar performance of CdSe pressed pellet electrodes.	126

List of Figures

Figure		Page
1.1	Schematics of a photoelectrochemical cell.	8
2.1	Energy diagram for an n-type semiconductor/ redox electrolyte junction.	40
2.2	Illustration of the different types of space charge regions in an n-type semiconductor/ electrolyte system	41
2.3	Energy level diagram for an electrochemical photovoltaic cell with an n-type semiconductor electrode at equilibrium in the dark (A), and under illumination (B).	42
2.4	Charge flow diagram for an electrochemical photovoltaic cell.	43
2.5	Energy level diagram for an n-type semiconductor/redox electrolyte interface with distribution of energy bands of the electrolyte.	44
2.6	The current-Voltage characteristics for a typical photovoltaic cell.	45
2.7	Theoretical maximum attainable efficiency as a function of semiconductor bandgap energy and temperature.	46
2.8	Illustration of the semiconductor decomposition energetics for anodic and cathodic decomposition.	47
2.9	Pourbaix (Potential-pH) diagram for CdSe in aqueous electrolyte.	48
2.10	The effect of ion adsorption at an n-type semiconductor/electrolyte junction.	49
2.11	Energy diagram for an n-type semiconductor/ electrolyte interface under illumination.	50

2.12	Equivalent circuit of an electrochemical solar cell, including the series and the shunt resistance.	51
2.13	Calculated values of quantum efficiency vs. output voltage for different values of normalized surface transfer velocity.	52
2.14	Variation of quantum efficiency with applied voltage for experimentally observed values for a CdSe single crystal photoanode.	53
2.15	The effects of series and shunt resistance on the output I-V characteristics.	54
2.16	Computed current densities versus applied voltage for varying values of surface transfer velocity.	55
2.17	J-V characteristics in the light and in the dark.	56
3.1	The crystal structure of CdSe.	80
3.2	Band diagram at k = 0 of CdSe at room temperature.	81
3.3	Energy level diagram for CdSe with a surface layer of CdS.	82
4.1	Voltammogram of the deposition bath for electroplated CdSe.	95
4.2	The test cell.	96
4.3	Absorption spectrum of the sulfide/ polysulfide redox electrolyte for 10 mm pathlength.	97
4.4	The measuring apparatus with white light illumination to determine current-voltage characteristics.	98
4.5	The measuring apparatus to determine quantum efficiency-voltage characteristics.	99
4.6	The measuring apparatus to determine spectral response.	100
4.7	Circuit replacing the potentiostat in Fig. 2.4 - 2.6.	101
4.8	Circuit to determine resistivity.	102

5.1 The surface morphology of annealed and and unannealed electrodeposited CdSe. 127

5.2 Current-voltage characteristics of annealed and untreated electroplated CdSe photoanodes. 128

5.3 Current-voltage characteristics of the electroplated CdSe/Ti substrate contact. 129

5.4 Surface morphology of etched and non-etched electroplated CdSe thin films. 130

5.5 Current-voltage characteristics of etched and unetched electroplated CdSe electrodes. 131

5.6 Quantum efficiency-voltage characteristics of the electrodes shown in Fig. 5.5. 132

5.7 The effect of light intensity on the short circuit current of electroplated CdSe elctrodes. 133

5.8 The effect of light intensity on the open circuit voltage of electroplated CdSe electrodes. 134

5.9 Surface morphology of unannealed and annealed pressure sintered CdSe electrodes. 135

5.10 Effects of pressure and its duration on the density of pressed CdSe. 136

5.11 Electron micrographs showing the surface morphology of annealed pressed CdSe samples. 137

5.12 Current-voltage characteristics of pressed CdSe electrodes. 138

5.13 Dark current-voltage characteristics of the electrodes of Fig. 5.12. 139

5.14 Dependence of the short circuit current density and the open circuit voltage on the densities of pressed pellets after annealing. 140

5.15 Voltage dependence of the quantum efficiency at 6328 Å for pressed samples. 141

5.16 Spectral response of annealed CdSe photoannodes pressed for 2 h. 142

5.17 Current-voltage characteristics for annealed single crystal CdSe in Cd atmosphere and under vacuum. 143

5.18 Voltage dependence of the quantum efficiency at 6328 Å for single crystal CdSe annealed in Cd atmosphere and in vacuum. 144

5.19 Spectral response of single crystal CdSe for Cd annealed and vacuum annealed electrodes with and without laser pumping. 145

5.20 Short circuit current wavelength response of vacuum annealed CdSe with simultaneous laser pumping for different, relative laser intensities. 146

5.21 Spectral response of single crystal CdSe for etched electrodes and anodized electrodes. 147

5.22 Spectral response of untreated, Cd annealed , vacuum annealed and Se annealed single crystal CdSe electrodes. 148

5.23 Current-voltage characteristics for Cd annealed single crystal, pressed pellet, and electro-plated CdSe electrodes. 149

5.24 Electron micrographs of annealed CdSe for an electroplated sample and a pressed pellet. 150

5.25 Voltage dependence of the quantum efficiency at 6328 Å for single crystal (Cd annealed), pressed pellet, and electroplated CdSe. 151

5.26 Spectral response of Cd annealed single crystal, pressed pellet, and electroplated CdSe. 152

5.27 Bandgap determination plot of $(\eta h\nu)^2$ vs. photon energy $h\nu$ for single crystal, pressed pressed pellet, and electroplated CdSe. 153

5.28 Effect of $ZnCl_2$ dipping on the I-V characteristics of pressed pellet electrodes. 154

5.29 The quantum efficiency-voltage characteristics of the electrodes shown in Fig. 5.28. 155

5.30 Comparison of the I-V characteristics of a $ZnCl_2$ dipped and a $HgCl_2$ dipped pressed pellet with the untreated photoanode. 156

5.31 Effect of $ZnCl_2$ dipping on the I-V characteristics of an electroplated CdSe electrode. 157

Chapter 1

Introduction

Research in solar energy conversion has been accelerated by the need for alternate energy sources due to the energy crisis in the seventies and the gradual depletion of fossil fuels.

Solar energy has a definite advantage over other energy sources in that it is virtually inexhaustible and does not pollute the environment. The solar energy received by the earth each month exceeds the total energy contained in the world's supply of fossil fuel [1]. Man's global energy requirement for one year is equal to the energy received in one hour of solar radiation.

Approximately 30 % of the solar energy which reaches the earth's surface is reflected back into space, about 47 % heats the surface of the land and oceans of which most is re-radiated back into space. Nearly 23 % of the insolation is utilized by evaporation and precipitation processes, while only a small fraction (0.02 %) is stored as chemical energy by photosynthesis [2]. This solar energy storage process provides all of our food and fossil fuel.

The sun has radiated energy at a fairly constant rate for

over 500 million years and is expected to remain constant for the next 50 million years [3]. The rate at which energy is received on a unit surface, in free space at the earth's mean distance from the sun, perpendicular to the sun's direction is called the solar constant. The accepted value is 1322 Wm^{-2} [4].

For most solar calculations it is sufficient to assume that the sun is a black body radiator at 6000 K. As sun light passes through the atmosphere the spectrum changes considerably due to selective absorption by the atmosphere. Fortunately little change takes place in the visible spectral region where solar cells are highly responsive.

In an attempt to simplify the presentation of the varying conditions of the atmosphere and its effect on light intensity, the two terms w and air mass m (AMm) are widely used. The quantity w is measured in cm as the precipitable water vapor in a vertical column in the atmosphere [5], e.g. w=0 and w=2 represent no humidity and 50 % humidity, respectively. The definition of m is given by :

$$m = (\cos z)^{-1} \qquad (1.1)$$

where z is the angle between a line normal to the earth's surface and a line connecting the observer and the sun, e.g. AM1 represents the sun vertically overhead, AM2 60° from zenith and AM0 describes solar radiation in space. The solar intensity varies considerably with different atmospheric conditions. For AM1 and w=0, the solar irradiance at sea level is 1060 Wm^{-2},

while for AM2 and w=0 and for AM1 and w=2 the irradiance decreases to 880 Wm^{-2} and 890 Wm^{-2}, respectively [5]. On a cloudy day with the sun at zenith, the solar intensity at sea level was estimated to be 120 Wm^{-2}, using the AM1-modified distribution for a black body radiator at 7000 K [5].

Solar energy may be utilized in three major ways, as a source of heat, to produce electricity (photovoltaic solar cell), and in electrochemical reactions (electrochemical solar cell). Thermal conversion is a simple process which involves the heating of black surfaces by normal or concentrated light. In photovoltaic devices, two dissimilar materials (p- and n-type semiconductor, semiconductor and metal, or different semiconductors) form a junction-barrier; in electrochemical solar cells a junction is formed by immersing a semiconductor in an electrolyte. Illumination of the junction results in a photovoltage, generated between the two different materials, which may be used as a source of power.

The history of solar cells dates back almost 150 years to 1839 when Becquerel discovered the photovoltaic effect in an electrolytic cell. He immersed a AgCl electrode connected to a metal counter electrode into a NaCl solution and observed an increased current flow by shining light on the AgCl electrode. The current was dependent on the wavelength of the light. The photovoltaic effect in Se was observed 34 years later by Adams and Day, and within 10 years the first Se solar cell was described by Fritts. In 1904, Hallwachs noticed that a layered

Cu/CuO structure was photosensitive and in 1914 Goldman and Brodsky were the first to correlate the photovoltaic effect with the existence of a barrier layer. By 1941, Se devices were converting solar energy to electricity with 1 % efficiency. The same year, a new process called the p-n junction technique enabled the production of single crystal Si photovoltaic devices. Controlled diffusion of dopants in Si pushed the efficiency to 6 % by 1953 (Chapin, Fuller, Pearson and Prince at AT&T's Bell Lab, and Rappaport, Lofersky and Jenny at RCA). By 1958, the solar-powered space age had begun and a new industry emerged. However, the low density of solar light flux and the appreciable power fluctuations in daily and annual cycles, caused concern for large-scale terrestial utilization of solar energy.

The aim of solar energy research in the last 10 years was to convert sunlight into electricity on a large-scale basis, as well as to make solar cells cost-competitive with conventional generators. For comparison, the price for a Si module which produced 1 W of electricity under peak illumination at noon cost $ 20-30 in 1973. Six years later a module with identical performance, although with higher efficieny and longer life expectancy sold for $ 10-15 [6]. Today the most efficient solar cells for industrial applications are single crystal Si p-n junction solar cells with an efficiency of ~14.5 %. The cost however (~$ 8 per peak W, estimated at $ 0.60 per kWh) is so far not competitive with hydroelectric power ($ 0.06 per kWh) since

the production of single crystal Si modules is a very costly and wasteful process.

P-n junction solar cells are formed by thermal diffusion of specific dopant atoms into the semiconductor material to an optimum junction depth. The dopant is chosen to invert the type of the semiconductor. For efficient solar energy conversion the junction barrier must form at a precise depth below the semiconductor surface. The diffusion process generally cannot be applied to much cheaper polycrystalline materials, since the thermal diffusion rate in the bulk and at grain boundaries is vastly different. The rapid diffusion along grain boundaries will introduce shunting in the polycrystalline material.

The grain boundaries in polycrystalline Si have been passivated effectively by H, and large scale production of polycrystalline Si was set up recently in the USA (Solarex) and in West Germany (Wacker Chemie and Telefunken). As well, H-doped amorphous Si solar cells are produced in Japan (Sanyo) and are used in pocket calculators. These amorphous and polycrystalline solar cells are much cheaper but have only been employed in low power applications [7].

In recent years, many researchers have been attracted to photoelectrochemical (PEC) systems for conversion of of solar energy. These cells are cheap and easily made. They essentially consist of a semiconductor electrode connected through a load with a counter electrode, immersed in a redox couple electrolyte (Fig. 1.1). Illumination of the semiconductor

drives electrochemical reactions at both electrodes. A junction barrier is formed spontaneously when the semiconductor is brought into contact with the electrolyte, and therefore the use of polycrystalline rather than single crystal material makes these devices inexpensive. There is no need for additional doping and diffusion of the dopant. Also the front metallization and antireflection coatings needed in solid state cells are not required [8].

Photoelectrochemical cells can be separated into two different types, the wet photovoltaic cell, where energy is converted into electricity, and the fuel cell, which makes chemical products through a chemical change in the electrolyte or the semiconductor electrode. Especially water splitting has received much attention, since hydrogen is an important chemical product of ecological purity [9].

1.1 Object of Research and Structure of Thesis

The purpose of this thesis is to investigate and compare the solar performance of electroplated, pressure sintered, and single crystal n-CdSe photoanodes in a polysulfide redox couple electrolyte. Annealing, etching, and ion surface treatments of the electrodes were employed to study their effect on various cell parameters.

Chapter 2 describes the principles and energetics of liquid

junction solar cells. Factors determining the stability and efficiency of photoelectrochemical cells are discussed, and a model which analyzes the current-voltage characteristics is represented. Only n-type semiconductor/electrolyte systems are described, but the treatments and discussions are equally valid for p-type semiconductors with appropriate changes of carrier type.

The following chapter reviews electrochemical photovoltaic cells employing CdSe photoanodes. The physical and chemical properties of CdSe, methods of electrode preparation, and various suitable redox couple electrolytes are described. The stability and lifetime of CdSe/polysulfide junction cells is discussed in detail, and the effect of surface etching and specific ion adsorption on the cell performance is described.

Preparation of the various CdSe electrodes investigated in this research, construction of the photoelectrochemical cells, and the experimental methods used to measure the cell characteristics are described in Chapter 4.

Chapter 5 presents the results of this research and gives a detailed discussion of the observed solar performance. The summary and conclusions follow in Chapter 6.

Figure 1.1 Schematics of a photoelectrochemical cell. Photogenerated holes in the n-type semiconductor (WE) oxidize electrochemical species A to A^+ and electrons transported through the external circuit reduce A^+ to A at the metal counter electrode (CE). The species A and A^+ form a reversible redox couple.

WE = working electrode

CE = counter electrode

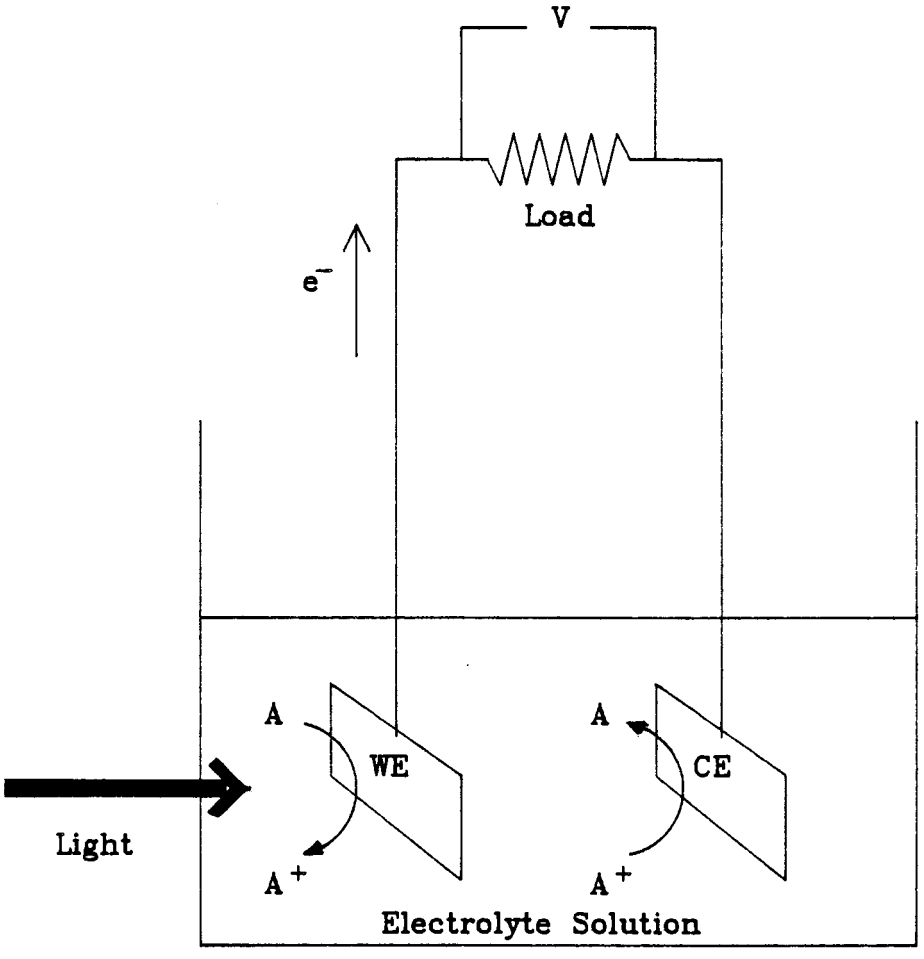
V
Load
e⁻
A
WE
A⁺
A
CE
A⁺
Light
Electrolyte Solution

Chapter 2

The Electrochemical Photovoltaic Cell

2.1 Principles and Energetics

The Bequerel effect [10] was not well understood until 1955 when Brattain & Garrett [11] associated the behaviour of an illuminated Ge electrode/electrolyte system with the formation of a liquid junction. Pioneering work towards understanding the kinetics and energetics of electron transfer across the semiconductor/electrolyte junction and the nature of the depletion region in the semiconductor are ascribed largely to Gerischer [12],[13],[14],[15],[16],[17], who stimulated increasing interest in semiconductor photoelectrochemistry.

The semiconductor/electrolyte junction is usually modelled as a Schottky barrier in which the electrolyte plays the role of the metal, a valid assumption for a highly conductive electrolyte. As the semiconductor is brought into contact with an electrolyte containing a redox couple, the Fermi level of the semiconductor (E_f) and the electrochemical potential of the solution (E_{redox}) equilibrate by electron transfer at the

interface, forming a barrier of height dependent on the nature of the solution species and the semiconductor as shown in Fig. 2.1.

The interface between the solid and the solution consists of three regions:

1. A space charge layer or depletion region (DR) formed in the semiconductor near the surface is depleted of free charge carriers. The width of the DR depends on semiconductor properties such as the dielectric constant and free carrier concentration.
2. The Helmholtz layer (HL) is formed in the electrolyte side between the solid and the outer Helmholtz plane (OHP). The HL arises from adsorption of solvated ions in the electrolyte on the surface of the solid, and its width will extend a few Å for ionic concentrations larger than 10^{-2} M [14].
3. The Gouy-Chapman layer forms in the solution adjacent to the OHP.

In Fig. 2.1, an energy diagram for an n-type semiconductor/liquid junction is shown. The Gouy-Chapman layer, extending from the interface into the interior of the electrolyte has been omitted, since the layer becomes extremely thin for concentrated electrolytes as used in photoelectrochemical cells [18]. As referred to in Fig. 2.1, the barrier height or bandbending (V_b) of the semiconductor may be

expressed in terms of the workfunction of the semiconductor (ϕ_{sc}) and the redox potential of the solution (ϕ_{redox}) and also as a function of the flatband energy (E_{fb}), i.e. the electrode potential energy at which the semiconductor bands are flat. The barrier height is given by

$$V_b = \phi_{sc} - \phi_{redox} \qquad (2.1)$$

$$qV_b = E_f - E_{fb} \qquad (2.2)$$

where E_f is the Fermi energy of the semiconductor. The effect of the Helmholtz layer on the bandbending is contained in the expression for the flatband energy, expressed with respect to the normal hydrogen electrode (NHE), i.e.

$$E_{fb}\ (NHE) = q\phi_{sc} + qV_H - 4.5 \quad [eV] \qquad (2.3)$$

where qV_H is the energy drop in the Helmholtz layer. The term 4.5 eV represents the difference between the NHE and the vacuum level.

The flatband potential is determined experimentally by photocurrent or capacitance measurements from the changing properties of the interface as the bands are made flat by illumination with intense light or forward bias. The flatband energy depends on the properties of the semiconductor, since E_f is controlled by bandgap and doping, and on the composition of the electrolyte, since the ionic double layer is formed by specific interaction with ions, which in turn changes the work

required for electron transfer from the semiconductor into the electrolyte.

The semiconductor/electrolyte interface may form four different types of barriers [18], depending on the redox potential with respect to the semiconductor Fermi level, applied voltage, and surface properties of the semiconductor. Figure 2.2 shows the depletion layer, accumulation layer, inversion layer, and deep depletion layer [18]. Minority carriers are essentially absent in the non-illuminated semiconductor and the depletion layer (Fig. 2.2a) is depleted of majority carriers. The accumulation layer (Fig. 2.2b) originates when carriers are injected from the surface of the semiconductor, so that the excess majority carriers form a space charge at the surface. This situation occurs when an n-type semiconductor is made extremely negative with respect to the counter electrode, so that the conduction band at the surface dips below the Fermi energy. An inversion layer (Fig. 2.2c) results when an excessive number of majority carriers is extracted at the interface, resulting in large bandbending and causing inversion of n-type to p-type at the semiconductor surface. This situation may arise in reverse bias, or when E_{redox} lies below the intrinsic Fermi level of the semiconductor. The deep depletion layer (Fig. 2.2d) depicts a non-equilibrium situation and results from application of a high reverse bias to the semiconductor.

For efficient photoelectrochemical cells, the semiconductor

should be depleted or weakly inverted since the minority carriers are drained away from the surface by transfer to the electrolyte. In fact, the necessary condition for efficient operation is that the rate of carrier transfer is equal to or larger than their rate of arrival at the semiconductor surface, which results in weak inversion or depletion [19].

Figure 2.3A depicts the energetics of an n-type semiconductor electrode in contact with a redox couple at equilibrium in the dark. For n-type semiconductor electrodes, the redox potential must be larger than the flatband potential and therefore E_{redox} should be situated between the conduction and valence bands of the semiconductor in such a manner as to maximize the barrier height. In the dark, the device behaves ideally like a diode with break-down at a forward applied voltage equal to V_b.

Figure 2.3B depicts the interface energetics of an electrochemical solar cell with an illuminated photoanode. When the semiconductor electrode is illuminated with light of energy $h\nu \geq E_g$, i.e. the bandgap of the semiconductor, the photons absorbed in the depletion region generate electron-hole pairs. The built-in electric field separates the charges and thereby reduces the barrier height, causing the band edges in the bulk to assume new values E_c^* and E_v^*. In the absence of recombination, the holes rise to the top of the valence band by thermal equilibrium and are then filled by an electron from the solution reductant, oxidizing species A to A^+. The excited

electrons drop to the bottom of the conduction band, travel downhill in the electric field through the bulk of the semiconductor and the external circuit. They are injected into the solution at the counter electrode to reduce A^+ to A. At the semiconductor, the electrochemical reaction is the reverse of that at the counter electrode, and the net chemical change of the entire system is zero.

During illumination of the cell, the potential difference between the semiconductor and counter electrode is equal to the change in bandbending, assuming that the voltage drop across the Helmholtz layer is independent of bias. Thus the photovoltage is determined by the displacement of E_f^* of the illuminated semiconductor relative to E_f of the dark electrode. The highest obtainable photovoltage, i.e. the open circuit voltage (V_{oc}), may result under strong illumination and is given by:

$$qV_{oc} = E_{redox} - E_{fb} \quad . \qquad (2.4)$$

Under closed circuit conditions E_{redox} and E_f equalize, and the photovoltage is zero even though a net charge flows, giving rise to a photocurrent (I_{sc}). Ideally, the holes react at the interface exclusively with the electrolyte, oxidizing the electron donors (Red) of the redox system.

The charge flow of the illuminated photoelectrochemical cell is summarized in Fig. 2.4. In the semiconductor the charge flow is partly due to both electron and hole transport, and in the metal, to electron transport only. The charge flow in the

electrolyte is characterized by ion transport via diffusion, drift and convection. In the semiconductor/liquid interface and in the metal/liquid interface the charge flow occurs by hole and electron transfer, respectively. The slowest rate of charge flow will determine the photocurrent. Ideally, pair generation is the rate limiting process, although under strong illumination, electrochemical systems with high ionic redox electrolyte concentrations often reveal the transfer across the semiconductor/electrolyte interface to be rate limiting [19], resulting in suppression of the photocurrent.

The transfer across the interfaces is believed to occur by tunnelling [19]. Tunnelling takes place from a filled state to an empty one at roughly the same energy. For high transfer rates across the interface the energy level of the acceptor ion must be located near the Fermi level of the counter electrode and the energy level of the donor ion must be near the minority carrier band edge at the surface.

Figure 2.5 shows the energy level diagram for an n-type semiconductor/electrolyte interface with a distribution of energy bands of oxidized and reduced species. The electronic levels of the redox species in polar solvents are broadened with Gaussian distribution due to the polarization of the solvent molecules surrounding the ions [18]. This polarization will affect the equilibrium potential of the ion with respect to the semiconductor. Thermal fluctuations in the polarization at the surface of the ion will cause the energy levels to fluctuate

about the most probable energy value.

Charge transfer by electrons or hole injection across the semiconductor/electrolyte junction can only occur when the unoccupied redox states (A^+) are at the same energy level as the occupied semiconductor states or when the occupied redox states (A) are at the same energy level as the unoccupied semiconductor states respectively.

The most probable displacement of oxidized and reduced species from E_{redox} is equal to the reorganizational energy λ, i.e. the work required for reorientation of the dipoles of the solvent (see Fig. 2.5). For a typical ion, λ is on the order of 1 eV [18].

In summary, the following criteria should usually be satisfied by the semiconductor electrode, the counter electrode, and the redox couple electrolyte, for efficient operation in an electrochemical photovoltaic cell:

1. The semiconductor must efficiently convert the absorbed light into electricity. Only photon energies of $h\nu \geq E_g$ are useful, thus the semiconductor must be chosen to have a bandgap that optimizes the conversion efficiency with respect to the solar spectrum.
2. The optical absorption depth (α^{-1}) of the semiconductor should be on the order of the depletion layer thickness in order to absorb most of the light in the DR. For direct bandgap transitions the depletion layer depth (W) depends

on the doping level and the dielectric constant of the semiconductor. For polycrystalline materials, the grain dimensions must exceed the absorption length and light must be absorbed in the top layers of the grains [20].

3. Photogenerated holes beyond the depletion region are transported by diffusion. Within their lifetime, the non-equilibrium carriers cover a distance on the order of their diffusion length (L_p). Thus minority carriers generated even deeper in the semiconductor, i.e.

$$\alpha^{-1} > W + L_p \quad , \qquad (2.5)$$

recombine before they have a chance to reach the semiconductor surface and thus do not contribute to the photocurrent. Most efficient charge separation is attained when the photogeneration region of the minority carriers lies entirely within the depletion region.

4. The location of the semiconductor energy bands relative to the electrolyte redox potential is an important factor since it determines the maximum open circuit voltage (V_{oc}) and the biasing requirements for the semiconductor electrode.

5. The most critical property is the stability of the semiconductor against decomposition reactions, i.e. photocorrosion and chemical dissolution. The energy position of the redox couple relative to the semiconductor band edges will determine the electrode's thermodynamic

stability in a particular redox system. However, some thermodynamically unstable semiconductors appear stable if the rate of decomposition is slow enough.

6. The counter electrode must provide fast charge transfer to secure reversibility of the photoelectrode's reaction.
7. The counter and the semiconductor electrode should be separated by a thin solution layer to facilitate fast transport of oxidized and reduced species of the redox system between the cathode and the anode, and to reduce light absorption in the electrolyte, which often contains colored redox couples.
8. The redox system must provide good reversibility, so that no net chemical change exists within the cell. The electrolyte must be of low ohmic resistance, which is provided by electrolyte concentrations of greater than 10^{-2} M.

2.2 Efficiency

The photoresponse of a solar cell may be chacterized by the power conversion efficiency η and/or the quantum efficiency η_q. The power conversion efficiency η represents the fraction of incident illumination that is converted into electrical power, i.e.

$$\eta = \frac{I_m V_m}{A P_i} \qquad (2.6)$$

where I_m and V_m are the current and voltage at the point of maximum power, respectively, of the solar cell, A is the illuminated area of the photoelectrode and P_i is the incident solar flux integrated over the entire solar spectrum. The power conversion efficiency depends on the current-voltage (I-V) characteristics of the solar cell as shown in Fig. 2.6, and thus η describes the quality of the solar cell.

Equation (2.6) can be rewritten in terms of the short circuit current (I_{sc}), the open circuit voltage (V_{oc}), and the fill factor (ff) of the cell, i.e.

$$\eta = \frac{I_{sc} V_{oc} ff}{A P_i} \quad . \qquad (2.7)$$

The optimum fill factor (ff = 1) describes a rectangular I-V characteristics of the solar cell. The fill factor (ff) is given by:

$$ff = \frac{I_m V_m}{I_{sc} V_{oc}} \quad . \qquad (2.8)$$

The quantum efficiency η_q of the solar cell represents the ratio of photocurrent density and incident photon intensity of energy $h\nu$.

The photoresponse of photoelectrochemical cells may be analyzed as a two step process:

1. Minority carriers generated in the DR and transported to the interface
2. Electrochemical reactions occuring at the semiconductor/electrolyte interface

The first step is controlled by the properties of the semiconductor; the second step is dependent on both semiconductor and electrolyte. For most semiconductor/ electrolyte systems, one of these steps will be the rate limiting factor. The predominant process can be determined by finding the photocurrent response as a function of light intensity. A linear behaviour is observed if the transport of minority carriers to the semiconductor surface is the rate-limiting process under the assumption that the charge carriers are not trapped in the space charge layer and do not recombine. A saturating photocurrent under high light intensities indicates that the electrochemical kinetics is the rate limiting process. For a large number of wet photovoltaic cells under AM1 insolation, the redox reaction kinetics play only a small role; thus the solar cell behaves like a solid state Schottky barrier system.

For solid state solar cells, the most important factor determining the efficiency is controlled by the threshold excitation energy (E_g) of the semiconductor. The theoretical

maximum attainable power conversion efficiency as a function of E_g and temperature for AM1 and w=0 illumination i.e., the sun at zenith and no humidity respectively, is shown in Fig. 2.7 [21]. The maximum solar-to-power conversion efficiency [5] is given by:

$$\eta_{max} \simeq \frac{q\, n_{ph}\, V_m}{N_{ph}\, E_{av}} \qquad (2.9)$$

where q is the electronic charge, n_{ph} is the number of photons that generate electron-hole pairs in the semiconductor with bandgap E_g, V_m is the voltage at the point of maximum power point, and N_{ph} and E_{av} are the number of incident photons and their average energy, respectively. With increasing E_g, η_{max} decreases due to the smaller number of absorbed photons. In addition η_{max} increases through V_m as the bandgap increases, due to the decrease in dark current. The increase in η_{max} with decreasing temperature arises from the temperature dependence of the dark current.

Semiconductors with a bandgap between 1.1 and 2.1 eV are efficient solar energy converters with optimum theoretical conversion efficiency of 25 - 30 % for AM1 and w=0 illumination at room temperature [5].

The simplest model to determine the operational quantum efficiency (η_q) of the solar cell is described by Gärtner [22] and Butler [23]. This model assumes that the photocurrent density arises only from carriers generated in the depletion

region (J_{DR}) and carriers generated in the bulk of the semiconductor which diffuse into the depletion region (J_{Diff}). Recombination and trapping of charge carriers, and reaction kinetics at the semiconductor/electrolyte interface are not accounted for in this model. The photocurrent density (J_{ph}) is given by:

$$J_{ph} = J_{DR} + J_{Diff} \quad . \tag{2.10}$$

The current density arising from electron-hole pair generation in the DR is given by:

$$J_{DR} = q\int_{0}^{W} g(x)\ dx \tag{2.11}$$

where q is the electronic charge, x is the distance from the semiconductor surface into the depletion region, and W is the depletion layer width. The electron-hole generation rate g(x) is given by:

$$g(x) = \phi\alpha \exp(-\ \ x) \tag{2.12}$$

where ϕ is the photon flux. The absorption coefficient of the semiconductor is of the form:

$$\alpha = A\ \frac{(h\nu - E_g)^{1/2}}{h\nu} \tag{2.13}$$

for near bandgap photon energies and direct bandgap transitions [24],[25]; A is a constant. The depletion layer thickness W is

given by:

$$W = W_o \, (V - V_{fb})^{1/2} \qquad (2.14)$$

where V is the applied voltage and V_{fb} the flatband potential; both measured relative to a reference electrode. The term W_o is given by:

$$W_o = \left(\frac{2 K \varepsilon_o}{q \, N_D} \right)^{1/2} \qquad (2.15)$$

assuming only the presence of donor impurities. The dielectric constant of the semiconductor is represented by K , N_D is the donor density, ε_o is the permittivity of free space, and q is the electronic charge.

The current density J_{DR} at an applied voltage V is obtained by substituting eq. (2.12) into eq. (2.11) and integrating, which results in:

$$J_{DR} = q\phi \, [1 - \exp(-\alpha W)] \quad . \qquad (2.16)$$

The current density arising from holes diffusing into the depletion region (J_{Diff}) is given by:

$$J_{Diff} = q\phi \, \frac{\alpha L_p}{1 + \alpha L_p} \, \exp[-\alpha W] \qquad (2.17)$$

where L_p is the diffusion length of the minority carriers. The derivation of J_{Diff} is shown in Appendix A. Combining eq. (2.16)

and eq. (2.17) yields the total photocurrent:

$$J_{ph} = q\phi \left(1 - \frac{\exp[-\alpha W]}{1 + \alpha L_p} \right) \quad . \qquad (2.18)$$

The quantum efficiency η_q may be found from:

$$\eta_q = \frac{J_{ph}}{q\ \phi} \qquad (2.19)$$

If $\alpha W << 1$ and $\alpha L_p << 1$, η_q can be approximated by $\eta_q \simeq \alpha W$. Thus the Gärtner/Butler model can be used to find the flatband potential of the semiconductor. A plot of $(\eta_q)^2$ as a function of applied voltage results in a straight line; the intercept on the voltage axis yields V_{fb}. The Gärtner/Butler model can also be used to find E_g for direct bandgap semiconductors by using the expression for α given in eq. (2.10) together with the above conditions ($\alpha W << 1$, $\alpha L_p << 1$), and plotting $(\eta_q h\nu)^2$ as a function of photon energy $h\nu$.

In summary, the quantum efficiency η_q of the solar cell, as described by the simple Gärtner/Butler model, depends on the dielectric constant, absorption coefficient, minority diffusion length, free carrier density, and flatband potential of the semiconductor. The variation of η_q on E_g results from the wavelength dependence of α. Although the above analysis ignores surface states, recombination and trapping of charge carriers, and the internal cell resistance, it provides a good fit to

experimental results at low forward bias and low light intensities.

2.3 Stability

The stability of the semiconductor electrode is a major concern for practical applications of electrochemical solar cells. The electrode must be stable against dissolution, electrolytic decomposition, and photocorrosion. The predominant factor is the intrinsic thermodynamic stability of the semiconductor. Gerischer [26],[27] and Bard and Wrighton [28] have proposed simple models for the thermodynamic stability of the photoelectrode. Photodecomposition occurs when minority charge carriers generated by illumination accumulate at the surface of the semiconductor to such an extent that oxidation or reduction of the semiconductor becomes possible. Corrosion of the electrode can also arise in the dark by accumulation of majority carriers at the surface with a suitable voltage applied to the semiconductor [11].

The position of the semiconductor bandedges at the semiconductor/electrolyte interface relative to the decomposition potential, provides direct information about the thermodynamic stability of the photoelectrode. Figure 2.8 illustrates the various energy correlations between the semiconductor band edges and the decomposition Fermi levels for

holes ($_pE_d$) and electrons ($_nE_d$). The (absolute) stable situation in Fig. 2.8a and the energetics susceptible to cathodic decomposition in Fig, 2.8d have not been encountered in combination with aqueous electrolytes. All efficient solar cells seem to be thermodynamically prone to anodic photodecomposition in aqueous electrolytes [27] and can be represented by the situations depicted in Fig. 2.8b and Fig. 2.8c.

A fast and convienient method to investigate the thermodynamic stability of a particular semiconductor electrode in an aqueous electrolyte was presented by Park and Barber [29]. They calculated Pourbaix (potential energy/pH) diagrams, which illustrate semiconductor stability and decomposition products over a wide pH range for various semiconductor/aqueous electrolyte systems. The Pourbaix diagram for CdSe is shown in Fig. 2.9.

The occurrence of photodecomposition depends largely on kinetics. A relatively high degree of stability of thermodynamically unstable semiconductors can be achieved if a redox couple electrolyte is chosen with appropriate energetics and kinetics. If the decomposition energy of the semiconductor is more positive than the reversible redox couple energy, the electrode will be unstable; it will be stable if the decomposition energy is more negative than E_{redox} [28].

Miller and Heller [30] and Ellis et al. [31], [32] were the first to demonstrate the stability of n-CdS with polysulfide

redox electrolytes, and obtained conversion efficiencies of 1 - 2 % . Studies on CdS, CdSe, and CdTe employing chalcogenide redox electrolytes (S^{2-}/S_n^{2-}, Se^{-2}/Se_2^{2-}, Te^{2-}/Te_2^{2-}) revealed that only CdTe in S^{2-}/S_n^{2-} is highly unstable [29],[30]. Observed conversion efficiencies with CdSe and CdTe single crystal electrodes are on the order of 8 % . Semiconductor electrodes of GaAs, GaP, and InP have also been studied with chalcogenide electrolytes [33],[34]. An efficiency of 8 % was reported for a single crystal n-GaAs/ Se^{-2}/Se_2^{-2} /C cell [35].

Coating an unstable small bandgap semiconductor surface with a thin layer of a more stable, higher bandgap semiconductor oxide was attempted by Wagner et al. [36] This approach offers potential for greater stability of the photoelectrode. If the electron affinity of both materials are appropriate, i.e. $\chi_{sc(small\ E_g)} < \chi_{sc(larger\ E_g)}$, then a higher V_{oc} may result. The authors observed an increased efficiency by a factor of 1.5 for n-GaAs electrodes with a 25 μm surface layer of CdS [36].

2.4 Surface States

An electronic energy level (E_{ss}) located at the semiconductor surface is called a surface state. If E_{ss} lies within the bandgap of the semiconductor, the surface state can act as a donor or acceptor level and trap and recombine photogenerated electrons and holes. This reduces the efficiency

of the solar cell. A surface state can also function as an intermediate state in the electron transfer between semiconductor bands and ions in solution. Capture of carriers at surface states is a dominant step in photodecomposition processes.

Surface states can arise from a weakened bond by interuption of the periodicy at the semiconductor surface, from lattice dislocation, and from grain boundaries in polycrystalline materials [37]. They also originate from adsorbed impurity species at the semiconductor surface, and in fact, nonadsorbed ions sufficiently close to the semiconductor surface for electron transfer with the bands, can act as surface states [18].

Occupation of the surface states by electrons or holes depends on their position relative to the semiconductor Fermi level at the surface, and thus a variation in bandbending can lead to a change in the occupation of the surface states. If a surface state lies between E_{fb} and the bulk conduction band energy, a reduction in bandbending by illumination of or voltage applied to the electrode can cause electrons from the bulk of the semiconductor to tunnel to the surface state (Fig. 2.10a). With a perfect shunt, the photovoltage of the solar cell cannot exceed $E_{ss} - E_c$, and thus the open circuit voltage is reduced. Imperfect shunting results in a reduced fill factor.

A high density of surface states located near the center of the bandgap may pin the Fermi level of the semiconductor. This

results in a fixed potential drop in the semiconductor. The concept of Fermi level pinning is known from solid state Schottky barrier systems, in which the bandbending of a semiconductor in contact with a variety of metals is essentially independent of the work function of the metal. Most group III-V semiconductors, as well as CdSe and CdTe, in contact with a metal are known to exhibit Fermi level pinning [38],[39],[40] . Bard et al. [41] associated Fermi level pinning with semiconductor/electrolyte systems in which the bandbending of the semiconductor is essentially independent of the solution potential. The authors showed that a surface state density of 10^{16} m^{-2} is sufficient to result in pinning of the Fermi level. Several semiconductor/electrolyte systems have been found to exhibit Fermi level pinning, for example n- and p-GaAs [42],[43],[44] and MoX_2 semiconductors, with X = S, Se, Te [45].

Adsorption of ions on the semiconductor surface can influence the position of the surface states and thus the performance of the solar cell. Heller et al. [8] proposed the following model illustrated in Fig. 2.10b,c: Weakly adsorbed ions split the surface energy level into two energy states slightly displaced from E_{ss}. As before electrons from the bulk of the semiconductor can tunnel to these states. Tunneling to E_{ss-ion} will further reduce the open circuit voltage since E_{ss-ion} lies closer to E_c than E_{ss}. However, strong ion interaction results in large splitting of the surface state, locating E_{ss-ion}^* near the conduction band edge at the surface

and locating E_{ss-ion} below or more positive than the conduction bandedge of the bulk. In this case tunnelling becomes unlikely, and thus strongly chemisorbed species will result in an open circuit voltage determined by $E_{fb} - E_{redox}$.

The above model was supported experimentally with a single crystal n-GaAs/ (Se^{2-}/Se_2^{2-})/OH^-) /C solar cell [46]. Strongly chemisorbed ions of Ru^{3+} and Pb^{2+} increased the efficiency of the cell from 7 % to 12 % . Ions such as Ca^{2+}, Sr^{2+}, and Ba^{2+} were not adsorbed, and weakly adsorbed Bi^{3+} caused deterioration in cell performance. Experiments with polycrystalline GaAs have shown that diffusion of strongly interacting Ru^{3+} ions into grain boundaries increased the efficiency by a factor of four [47]. Dipping the polycystalline GaAs electrode into the aqueous cation solutions resulted in passivated grain boundaries in the top 10^3 A light absorbing region and proved to be adequate for maximum improvement of V_{oc} [37].

2.5 The Mathematical Model

Several authors [48],[22],[23],[49],[50] have analyzed the current-voltage (I-V) characteristics of the semiconductor/ electrolyte solar cell. However, no model included all the important parameters that affect the performance of the device. Reiss [48] derived an analytical model for the I-V characteristics, neglecting recombination in the depletion

region (DR). The Gärtner/Butler expression [22],[23] is only applicable under reverse and low forward bias, and ignores the reaction kinetics at the surface , as well as carrier recombination in the DR. Wilson [49] included reaction kinetics at the interface in terms of a constant charge transfer velocity for minority carriers and surface recombination velocity. However, his model only considered the photogenerated current without including the opposing dark current, and also neglected recombination in the DR. Reichman [50] included a discussion of carrier recombination in the depletion region, but did not consider recombination at the surface.

El Guibaly and Colbow [51],[52] presented models which incorporated the above-mentioned processes in addition to the effects of series resistance and shunt resistance of the cell on the observed quantum efficiency variation with voltage. The model assumes that the surface recombination current is proportional to the excess hole concentration at the surface, with the recombination velocity as the proportionality constant [51],[53]. This results in the assumption that the quasi-Fermi level for holes and electrons, E_{Fp} and E_{Fn}, respectively, are flat throughout the DR as shown in Fig. 2.11.

The quasi-Fermi levels vary with photon flux and applied voltage, but can be considered flat under the following conditions [53]: For high doping levels ($>10^{24}$ m^{-3}), E_{Fp} will be flat throughout the DR. E_{Fn} will be constant in the depletion region if the electron current density in the bulk (J_n) is much

larger than the exchange current density with the conduction band at equilibrium, and if the electron current density due to illumination of the semiconductor (J_{l_n}) is much smaller than the electron current density with applied voltage in the bulk, i.e. $J_{l_n} \ll J_n \exp(qV/kT)$. Experiments have shown that for Si and GaAs, the variation of E_{Fn} in the depletion region was negligible ($<kT/q$) for an applied voltage comparable to the open circuit voltage [54].

The model presented below [52],[53],[55] assumes that the quasi-Fermi level for both, holes and electrons is flat throughout the DR. It ignores coupling between electrons and holes caused by recombination centers. The model includes reaction kinetics at the interface, electron and hole recombination at the surface and in the depletion layer, and the effects of the series and shunt resistances of the cell on the performance characteristics.

Figure 2.11 shows an electron energy level diagram near the semiconductor surface [55]. The photoanode is illuminated and a forward bias V is applied across the depletion region. The electrolyte concentration is assumed to be sufficiently high so that the capacitance of the Helmholtz layer (HL) is at least an order of magnitude larger than the depletion region capacitance. Thus, the voltage drop across the HL is independent of bias, and the applied voltage appears entirely across the DR and the series resistance (R_s) of the cell.

The equivalent circuit for the electrochemical photovoltaic

cell is shown in Fig. 2.12 [55]. The photocurrent is represented by a current source $I_l(V)$ and the current of the forward biased diode junction is given by $I_d(V)$. Series resistance of the cell is represented by the fixed resistor R_s and is assumed to arise from the bulk resistivity of the semiconductor. The back contact of the cell is assumed to be ohmic, and the electrolyte should offer negligible resistance to current flow. The shunt resistance R_{sh} may result from surface leakage along the edges of the cell and/or by small electrolytic bridges along microcracks.

From Fig. 2.12, the terminal current (I_o) and voltage (V_o) can be written as:

$$I_o = I_l - I_d - \frac{V_o}{R_{sh}} \quad . \tag{2.20}$$

and

$$V_o = V - (I_l - I_d)R_s \tag{2.21}$$

For a given forward bias (V) applied across the DR, the total and dark junction currents per unit area, J_l and J_d, respectively, are:

$$J_l = q\,\phi\,\frac{S_c}{S}\left(1 - \frac{\exp(-\alpha W)}{1 + \alpha L_p}\right) \tag{2.22}$$

and

$$J_d = J_{po}\frac{S_t}{S}\exp\left(\frac{qV}{kT}\right) + B\exp\left(q\,\frac{V - U/2}{kT}\right) + J_{no}\left[\exp\left(\frac{qV}{kT}\right) - 1\right] \quad (2.23)$$

where

$$S = S_t + S_r + \exp\left(-q\,\frac{V_D - V}{kT}\right) + B\exp\left(-q\,\frac{V_D - V + U/2}{kT}\right) \quad . \quad (2.24)$$

The width of the depletion layer (W) was defined by eq. (2.14) and eq. (2.15) on page 22. The incident photon flux, ϕ, is corrected for losses due to reflection and electrolyte absorption. The hole diffusion length L_p depends on the diffusivity D and hole lifetime τ in the bulk of the semiconductor, i.e. $L_p = (D\tau)^{1/2}$. The reverse saturation flux due to hole diffusion in the bulk J_{po} is given by $J_{po} = p_o D / L_p$, where p_o represents the equilibrium hole density in the bulk and J_{no} describes the electron exchange flux at equilibrium. The term $S_t = s_t / (D/L_p)$ is the normalized hole surface transfer velocity s_t with respect to the "diffusion velocity" D/L_p. The normalized recombination velocity at the semiconductor/electrolyte interface S_r is given by $S_r = s_r / (D/L_p)$. The bandbending potential in the dark is represented by V_D, and the separation between the quasi-Fermi levels is given by U.

The expression for S in equ. (2.24) contains various terms, corresponding to normalized velocities. The first term on the

right hand side corresponds to the ease of communication between the electrolyte and the valence bandedge at the surface of the semiconductor. The other three terms describe the various loss mechanisms that result in deterioration of the output parameters of the cell. The second term corresponds to the loss of photoexcited holes through recombination at the interface, and depends on the density and energy distribution of surface states [49],[51]. The third term describes loss of photoexcited holes by diffusion into the bulk of the semiconductor instead of diffusion towards the interface. The last term depicts loss of photoexcited holes through recombination in the depletion layer and it involves the parameter B which describes the recombination in the DR; B is given by:

$$B = \frac{C}{[1/2(E_g - qU) - \Delta]^{1/2}} \qquad (2.25)$$

where

$$C = \frac{kT}{8\,q}\,\frac{\tau}{\tau_t}\,\frac{\alpha W}{\alpha L_p}\exp\frac{E_g/2 - \Delta}{kT} \qquad (2.26)$$

The potential difference between the two quasi-Fermi levels is represented by U, where:

$$qU = E_{fp} - E_{fn} \quad . \qquad (2.27)$$

The fact that the minority carrier concentration in the DR is

larger in the illuminated semiconductor than in the bulk yields a separation between the quasi-Fermi levels (U) which is larger than the forward applied voltage (V). For a given photoanode material U depends greatly on the illumination intensity and the surface transfer velocity S_t. El Guibaly and Colbow have shown that for a CdSe photoanode U never exceeds V by more than 0.2 V for light intensities smaller than AM1 [55].

The separation between the semiconductor Fermi level in the bulk and bottom of the conduction band is represented by Δ. The hole lifetime in the bulk is given by τ and τ_t is the effective hole lifetime in the DR given by:

$$\tau_t = \frac{1}{\sigma v_{th} N_t} \quad . \qquad (2.28)$$

The capture cross section for electrons or holes (assumed to be equal) for recombination centers of density N_t with energy level at or near the intrinsic Fermi level E_i is given by σ and v_{th} is the carrier thermal velocity. The terms k and T are the Boltzmann constant and the absolute temperature, respectively.

The function S increases with forward applied voltage mainly due to the exponential increase of the third and fourth terms with bias; S may also increase due to increasing S_r, which is brought about by filling the surface states with electrons. The expression for photocurrent in eq. (2.22) is similar to the Gärtner/Butler expression on page 24, with the exception of the

extra term S_t/S, which gives the number of holes arriving at the interface to contribute to the photocurrent. When the term S increases with applied voltage, the ratio S_t/S will quickly decrease, causing deterioration in the photoresponse of the cell. Figure 2.13 [52] illustrates the variation in the quantum efficiency, i.e. $\eta_a = J_l / q0$, of the cell with output voltage V_o for various values of hole transfer velocity S_t for a CdSe photoanode. From Fig. 2.13, it is apparent that the photoresponse of the cell decreases rapidly after V_o reaches a threshold value, which is dependent on the ratio S_t/S. The S-shape behaviour of the photocurrent with forward bias is observed experimentally.

The diode current in equ. (2.23) is opposite to the photocurrent and contains three components; the hole injection-diffusion term, the hole recombination-generation term, and the electron exchange current. The last component of J_d is generally several orders of magnitude larger than the other two terms, since the concentration of electrons at the surface is much larger than the hole concentration. In addition, for n-type semiconductors the overlap between the conduction band and the energy states of oxidized species of the electrolyte is greater than the overlap between the valence band and the energy states of the reduced species [17].

Figure 2.14 [51] represents a fit of El Guibaly and Colbows's model to the experimentally observed quantum efficiency dependence on applied voltage for a single crystal

n-CdSe/ (S^{2-}/S_n^{2-})/OH^- /Pt cell (curve a) [44]. Calculated quantum efficiencies for the same values of αW_o and αL_p from the Reiss model (curve b) and the Gärtner/Butler model (curve c) do not exhibit the experimentally observed S-shape behaviour.

The effect of the series resistance (R_s) of the electrochemical photovoltaic cell on the I-V characteristics is illustrated in Fig. 2.15a. The series resistance (R_s) does not affect the open circuit voltage, but the fill factor and the power conversion efficiency are seen to be appreciably reduced. There is also a slight reduction in short circuit current due to the voltage drop across the series resistance. The forward bias reduces the photocurrent in eq. (2.22) through the term $\exp(-\alpha W)$.

Figure 2.15b shows the effect of shunt resistance (R_{sh}) on the output I-V characteristics; R_{sh} has no effect on the short circuit current, but reduces the cell's open circuit voltage, fill factor, and power conversion efficiency.

In an analysis of the cell performance, it is often assumed that the dark current determines the shape of the I-V characteristics. This behaviour is called the superposition principle. Figure 2.16 [56] illustrates the dependence of the I-V curves on the surface transfer velocity S_t. The superposition principle appears to hold well only for large transfer velocities as shown in Fig. 2.16a. The situation shown in Fig. 2.17 [56] illustrates the effect of surface states on the superposition principle. These surface states act as

trapping sites, but in addition, they may become ionized upon illumination, causing a reduction in bandbending of the semiconductor. As a result, the photocurrent approaches zero before the dark current becomes appreciable.

Figure 2.1 Energy diagram for an n-type semiconductor/redox electrolyte junction.

χ = electron affinity

ϕ_{sc} = semiconductor workfunction

V_b = bandbending potential

E_{fb} = flatband potential

E_c = bulk conduction bandedge of the semiconductor

E_f = Fermi energy

E_v = bulk valence bandedge of the semiconductor

E_g = semiconductor bandgap

W = depletion layer width

OHP = outer Helmholtz plane

E_{redox} = energy of the redox system

ϕ_{redox} = potential energy of the redox system

V_H = Helmholtz potential

SS Scale = solid state energy scale

NHE Scale = electrochemical potential scale relative to the normal H electrode

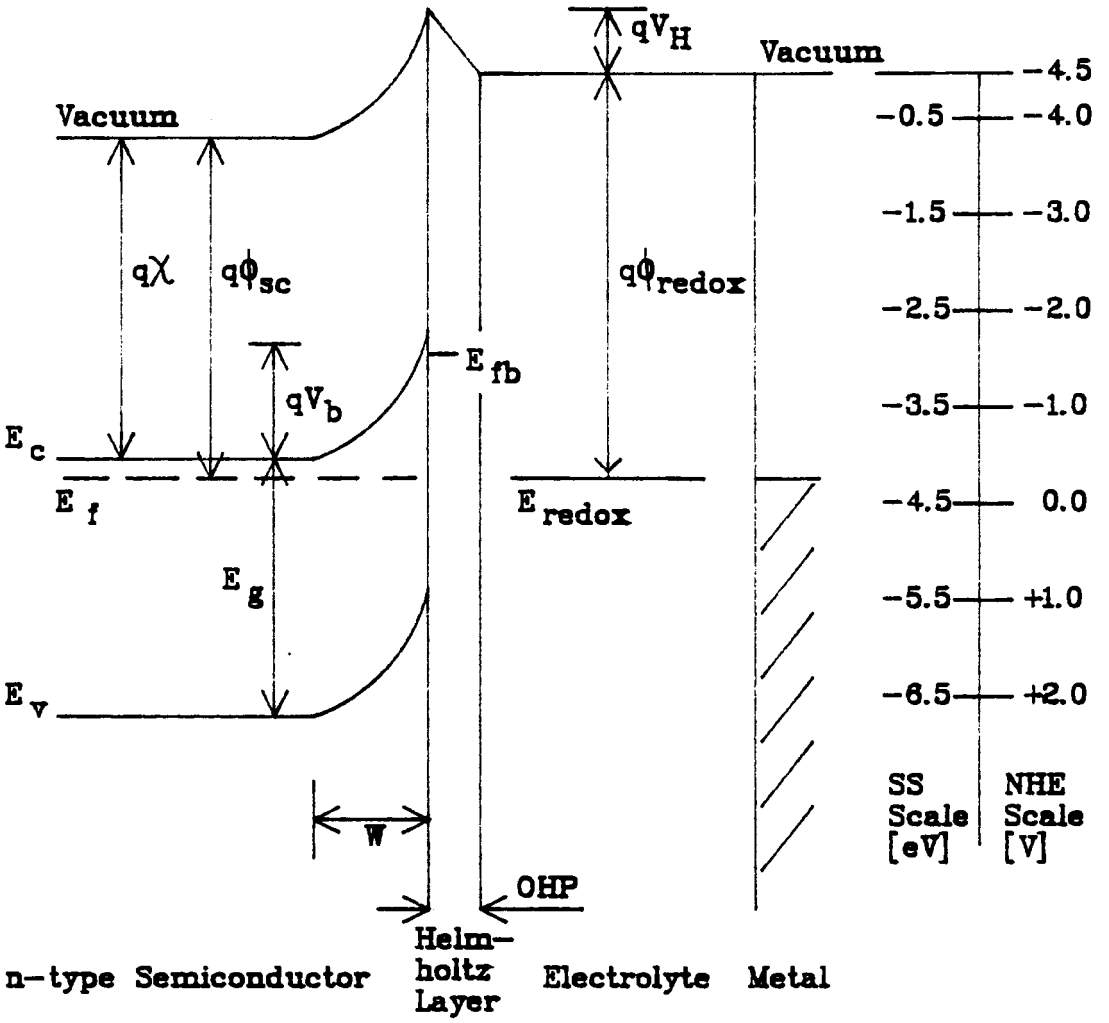
qV_H
Vacuum
Vacuum
qχ
qφ_sc
qφ_redox
E_fb
qV_b
E_c
E_f
E_redox
E_g
E_v
W
OHP
Helm-
holtz
Layer
n-type Semiconductor
Electrolyte
Metal
-4.5
-0.5
-4.0
-1.5
-3.0
-2.5
-2.0
-3.5
-1.0
-4.5
0.0
-5.5
+1.0
-6.5
+2.0
SS
Scale
[eV]
NHE
Scale
[V]

Figure 2.2 Illustration of the different types of space charge regions in an n-type semiconductor/electrolyte system:

(a) depletion layer

(b) accumulation layer

(c) inversion layer

(d) deep depletion layer

(For abbreviations, see Fig. 2.1.)

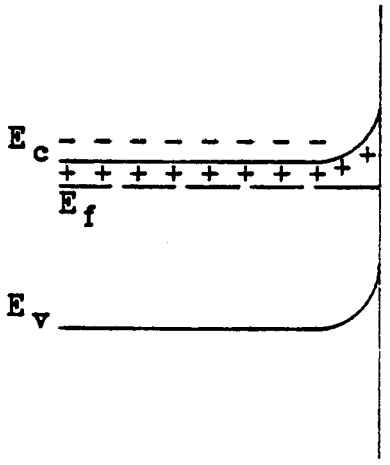

a

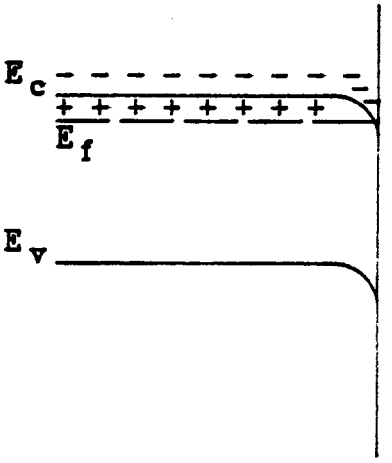

b

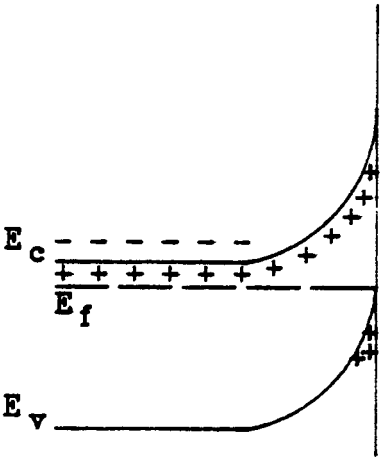

c

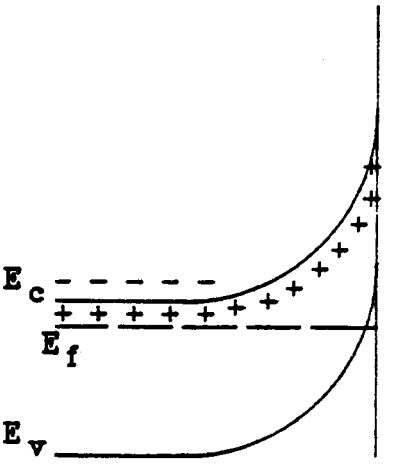

d

Figure 2.3 Energy level diagram for an electrochemical photovoltaic cell with an n-type semiconductor electrode at equilibrium in the dark (A), and under illumination (B).

E_{c_s} = conduction band energy at the semiconductor surface

E_{v_s} = valence band energy at the semiconductor surface

$h\nu$ = photon energy ($\geq E_g$)

e^- = photogenerated electron

h^+ = photogenerated hole

E_c^* & E_v^* = new assumed conduction and valence bandedges in the bulk of the semiconductor due to illumination of the photoanode with $h\nu \geq E_g$.

(For abbreviations, see Fig. 2.1.)

A

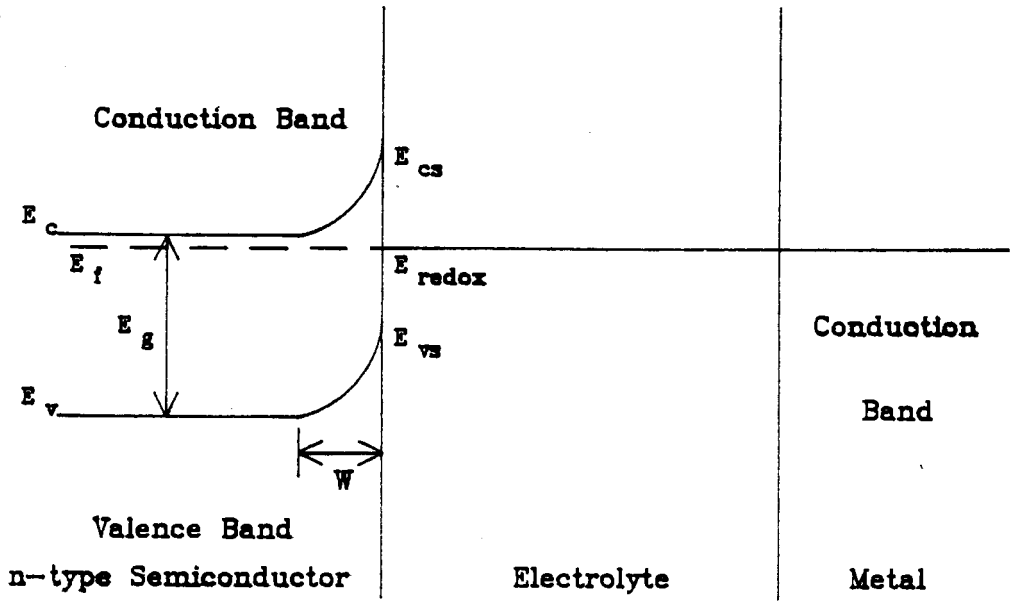
Conduction Band
E cs
E c
E f
E redox
E g
E vs
E v
Conduction
Band
W
Valence Band
n-type Semiconductor
Electrolyte
Metal

B

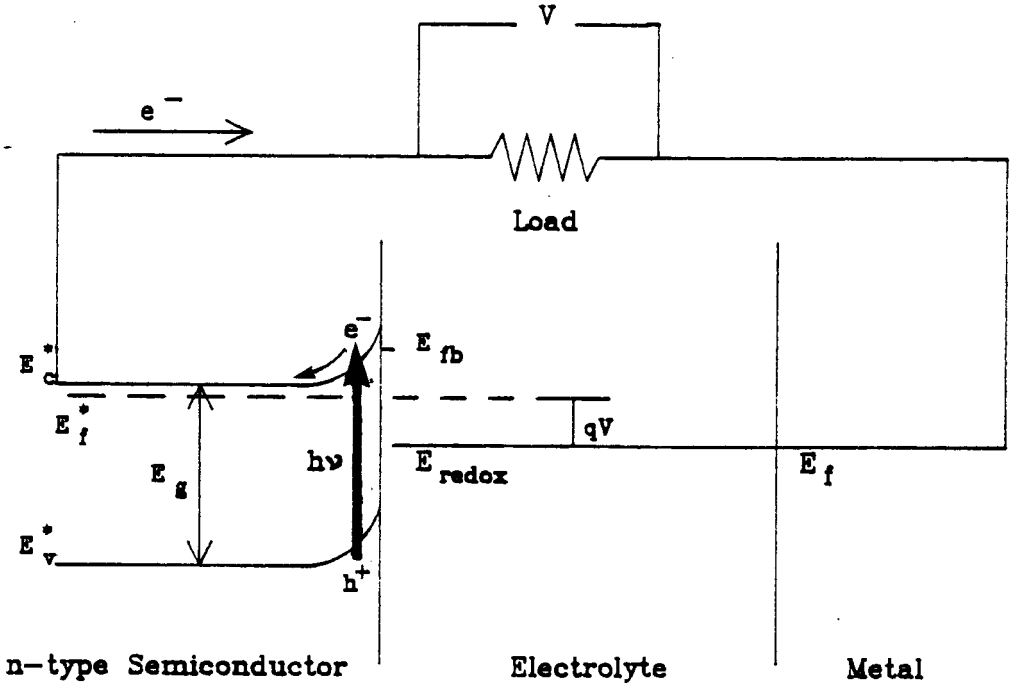
V
e −
Load
e−
E fb
E* c
E* f
qV
hν
E redox
E f
E g
E* v
h+
n-type Semiconductor
Electrolyte
Metal

Figure 2.4 Charge flow diagram for an electrochemical photovoltaic cell.

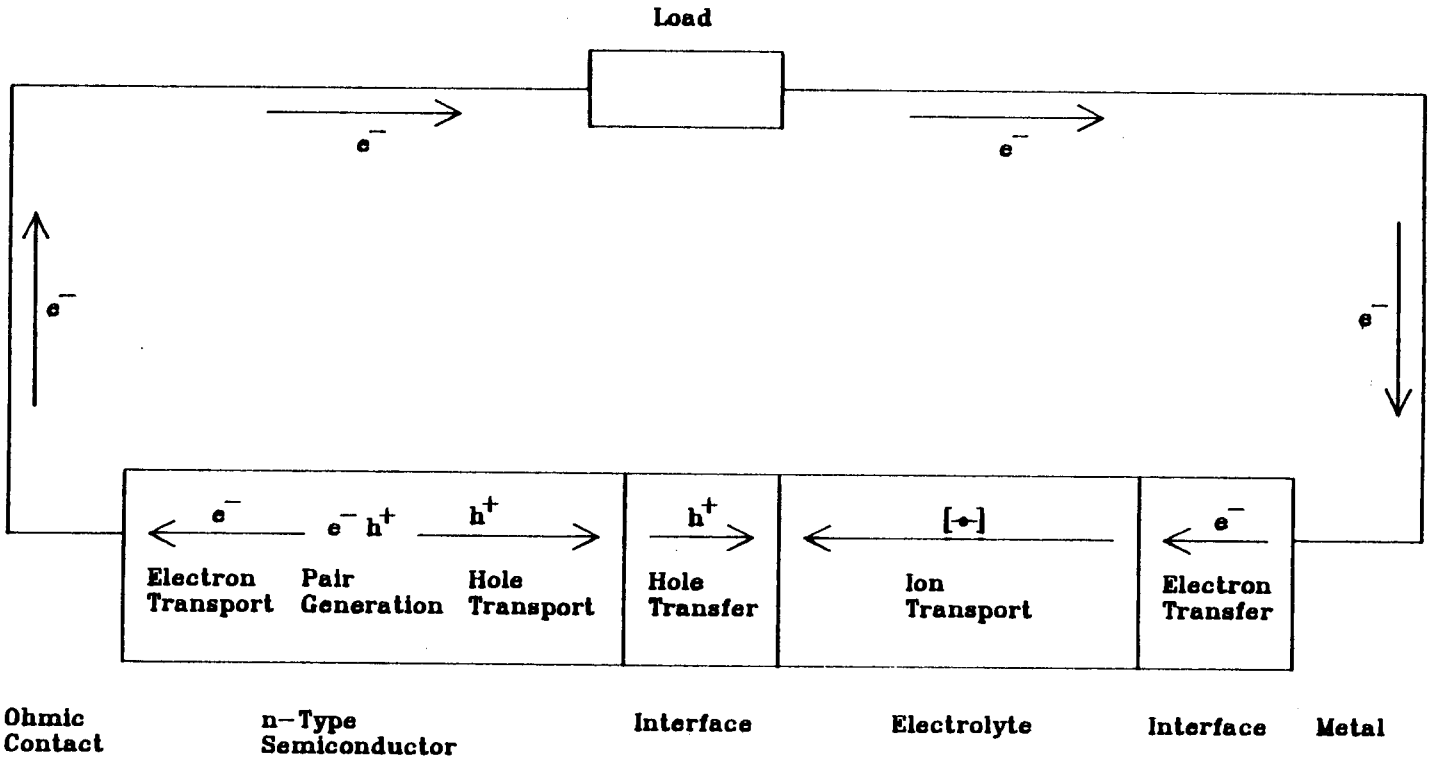
Load
e⁻
e⁻
e⁻
e⁻
e⁻
e⁻ h⁺
h⁺
h⁺
[-•-]
e⁻
Electron Transport
Pair Generation
Hole Transport
Hole Transfer
Ion Transport
Electron Transfer
Ohmic Contact
n-Type Semiconductor
Interface
Electrolyte
Interface
Metal

Figure 2.5 Energy level diagram for an n-type semiconductor/redox electrolyte interface. The distribution of energy bands of the electrolyte E_{redox} arise from solvated ions. The separation of 2λ between the two most probable states of reduced and oxidized species (E_{red} and E_{ox}, respectively) arises from polarization differences of the solvent.

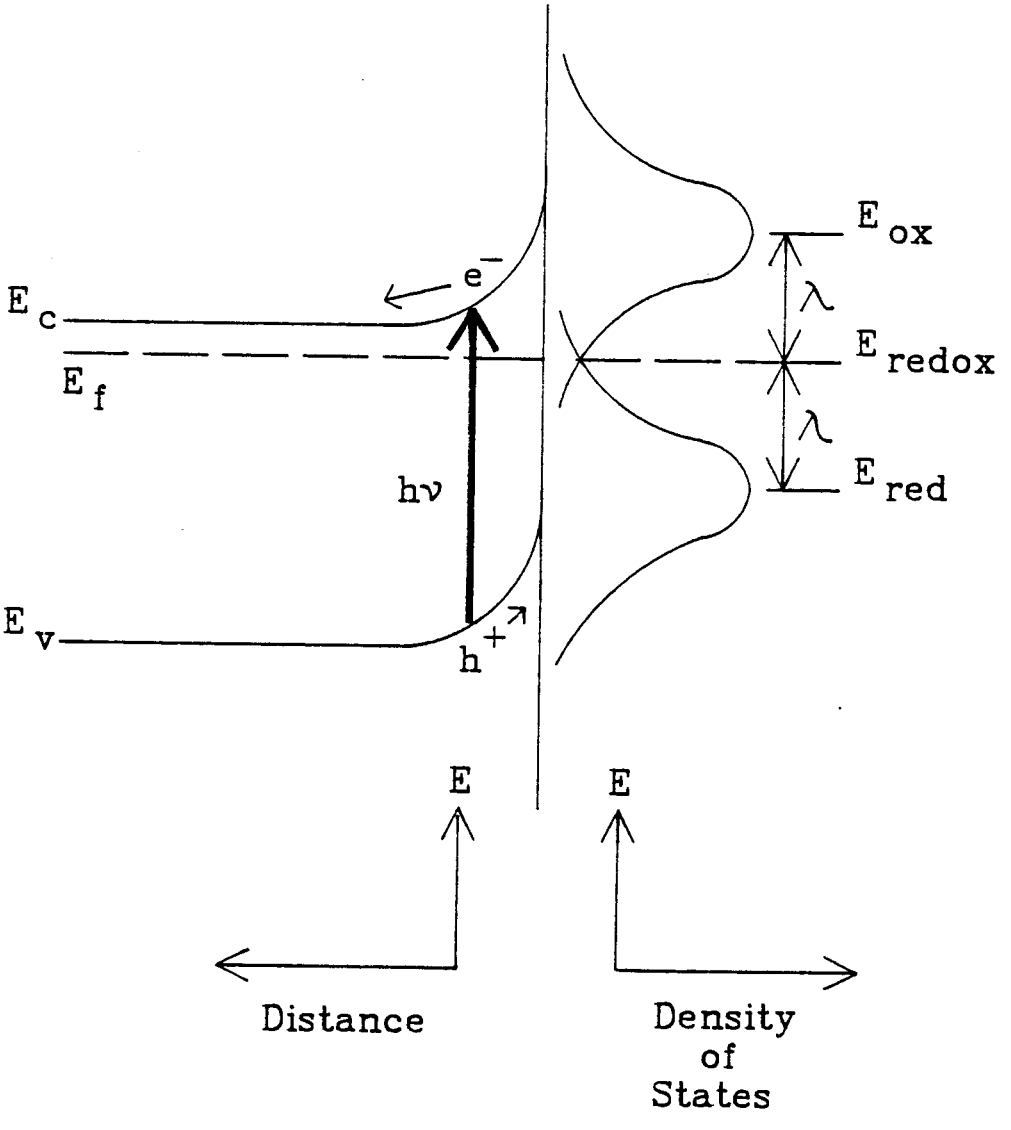
E ox
λ
E redox
λ
E red
e⁻
E c
E f
hν
E v
h⁺
E
E
Distance
Density
of
States

Figure 2.6 The current-Voltage characteristics for a typical photovoltaic cell.

I_{sc} = short circuit current

V_{oc} = open circuit voltage

I_m = current at the point of maximum power

V_m = voltage at the point of maximum power

P_m = point of maximum output power

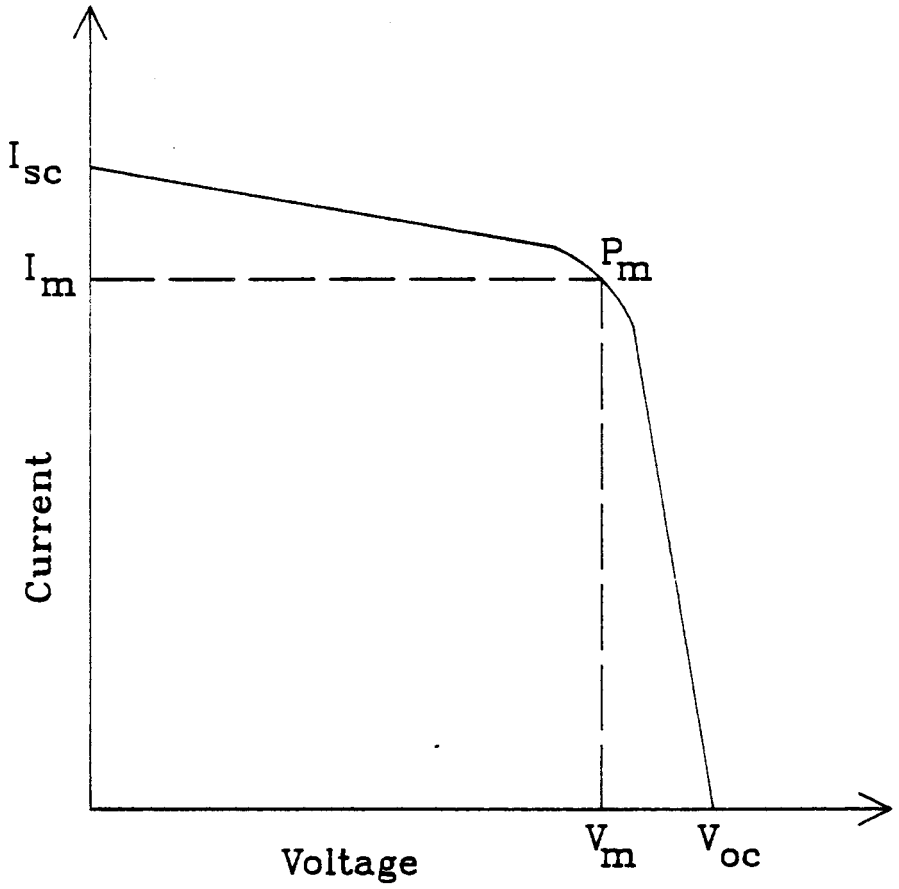
I_{sc}
I_m
P_m
Current
Voltage
V_m
V_{oc}

Figure 2.7 Theoretical maximum attainable efficiency as a function of semiconductor bandgap energy and temperature

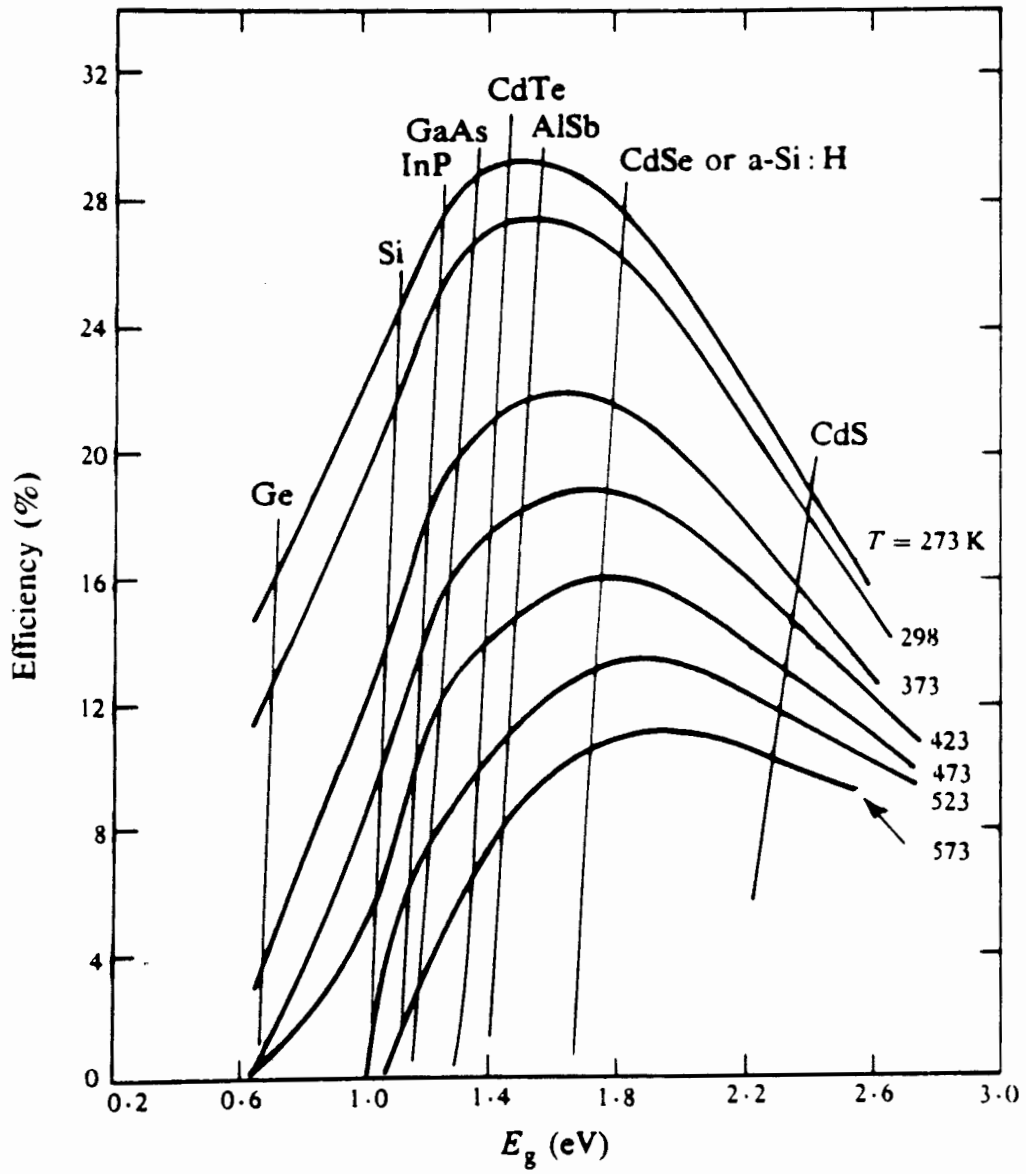
Efficiency (%)
32
28
24
20
16
12
8
4
0
0·2
0·6
1·0
1·4
1·8
2·2
2·6
3·0
E_g (eV)
CdTe
GaAs
InP
AlSb
CdSe or a-Si : H
Si
Ge
CdS
T = 273 K
298
373
423
473
523
573

Figure 2.8 Illustration of the semiconductor decomposition energetics for anodic and cathodic decomposition (pE_d and nE_d, respectively)

(a) stable against both anodic and cathodic decomposition

(b) unstable against both anodic and cathodic decomposition

(c) unstable against anodic, and stable against cathodic decomposition

(d) reverse of (c), stable against anodic, and unstable against cathodic decomposition

(For abbreviations, see Fig. 2.1.)

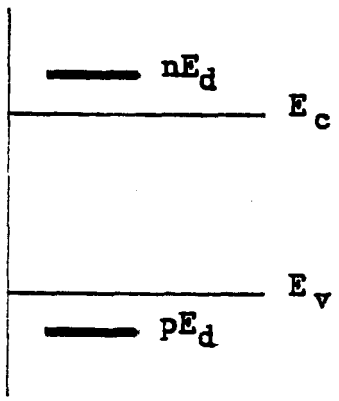

a

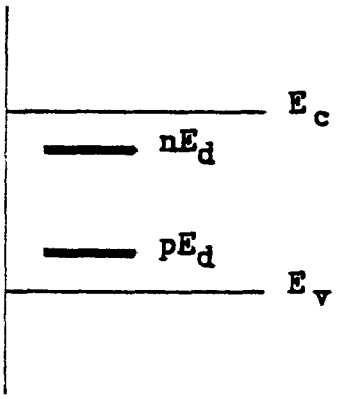

b

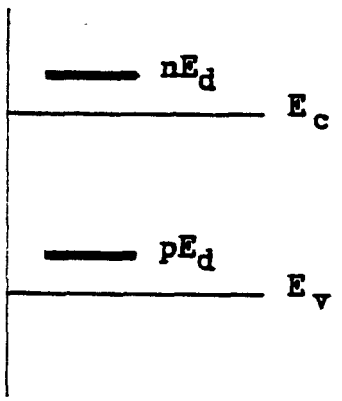

c

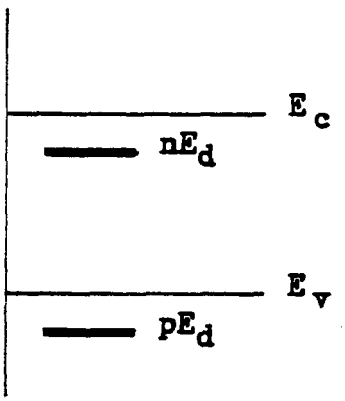

d

Figure 2.9 Pourbaix (Potential-pH) diagram for CdSe in aqueous electrolyte. The indicated flatband potentials (E_{fb}) correspond to pH 7 [17] and pH 14 [57].

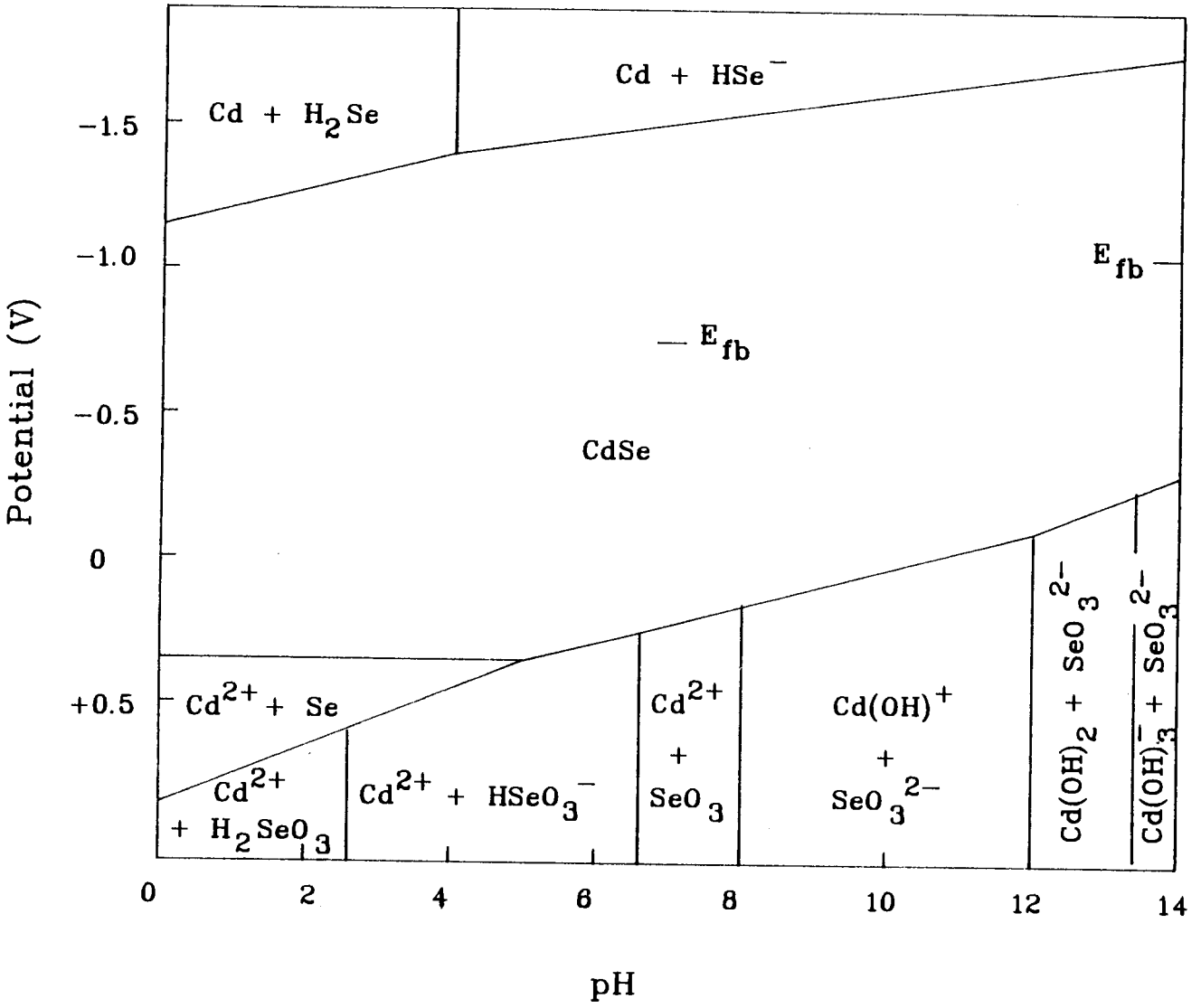
Cd + H2Se
Cd + HSe−
−1.5
−1.0
−0.5
0
+0.5
Potential (V)
Efb
— Efb
CdSe
Cd2+ + Se
Cd2+ + H2SeO3
Cd2+ + HSeO3−
Cd2+ + SeO3
Cd(OH)+ + SeO3 2−
Cd(OH)2 + SeO3 2−
Cd(OH)3− + SeO3 2−
0
2
4
6
8
10
12
14
pH

Figure 2.10 The effect of ion adsorption at an n-type semiconductor/electrolyte junction. A surface state near the conduction band (a) may split into two levels, E_{ss-ion} and E_{ss-ion}^{*}, by weak ion adsorption (b), and strong ion interaction (c).

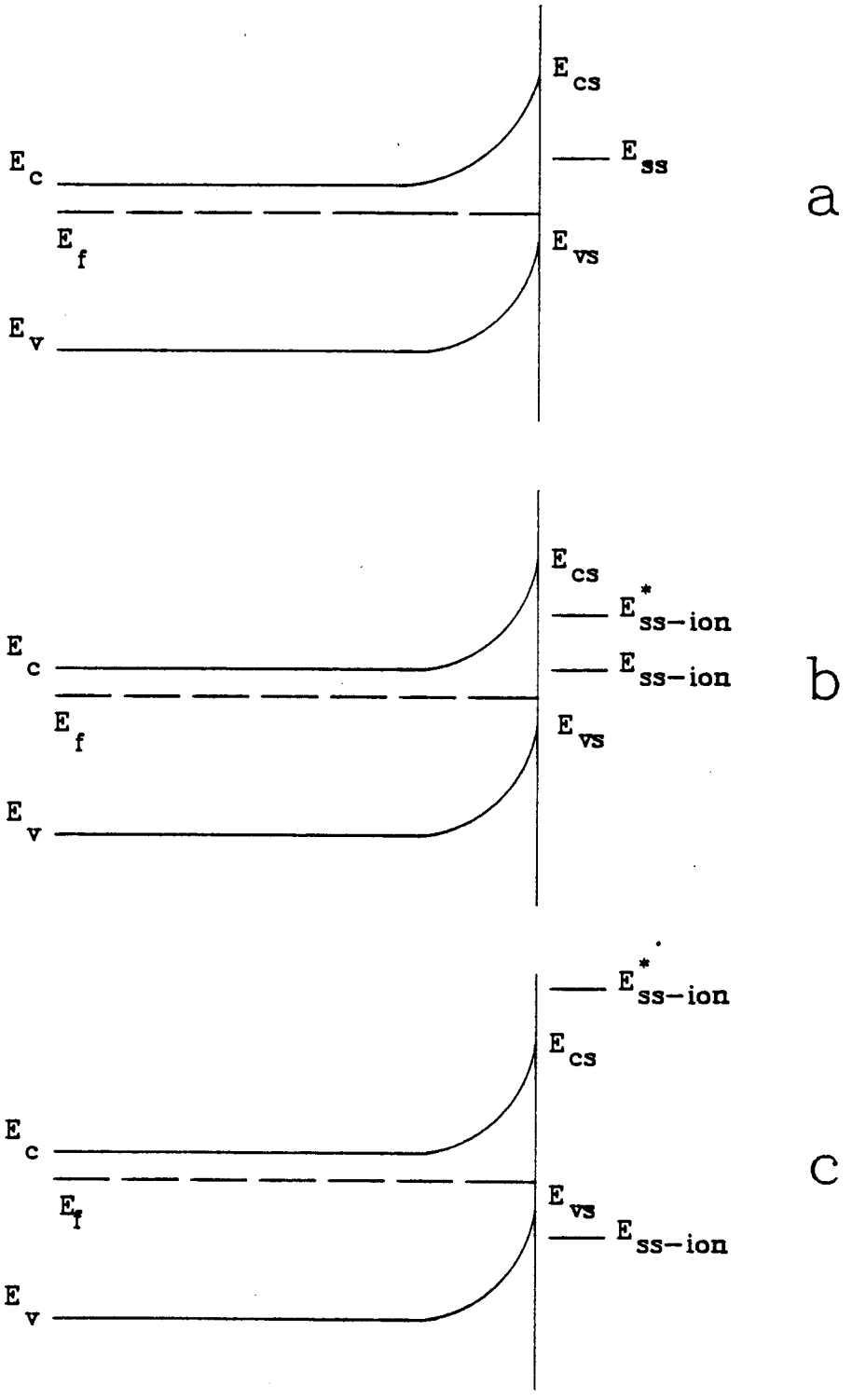
E_{cs}
E_{ss}
E_c
E_f
E_{vs}
E_v
a
E_{cs}
E^*_{ss-ion}
E_{ss-ion}
E_c
E_f
E_{vs}
E_v
b
E^*_{ss-ion}
E_{cs}
E_c
E_f
E_{vs}
E_{ss-ion}
E_v
c

Figure 2.11 Energy diagram for an n-type semiconductor/ electrolyte interface. The photoanode is assumed to be under illumination, and a forward bias V is applied which reduces the bendbending from qV_b to $q(V_b - V)$.

V_b = equilibrium bandbending voltage

E_c = conduction band energy

E_v = valence band energy

E_g = semiconductor bandgap

E_i = intrinsic-Fermi level

E_{Fn} = quasi-Fermi level for electrons

E_{Fp} = quasi-Fermi level for holes

Δ = separation between E_{Fn} and E_c

qU = separation between the semiconductor Fermi level in the bulk and the bottom of the conduction band

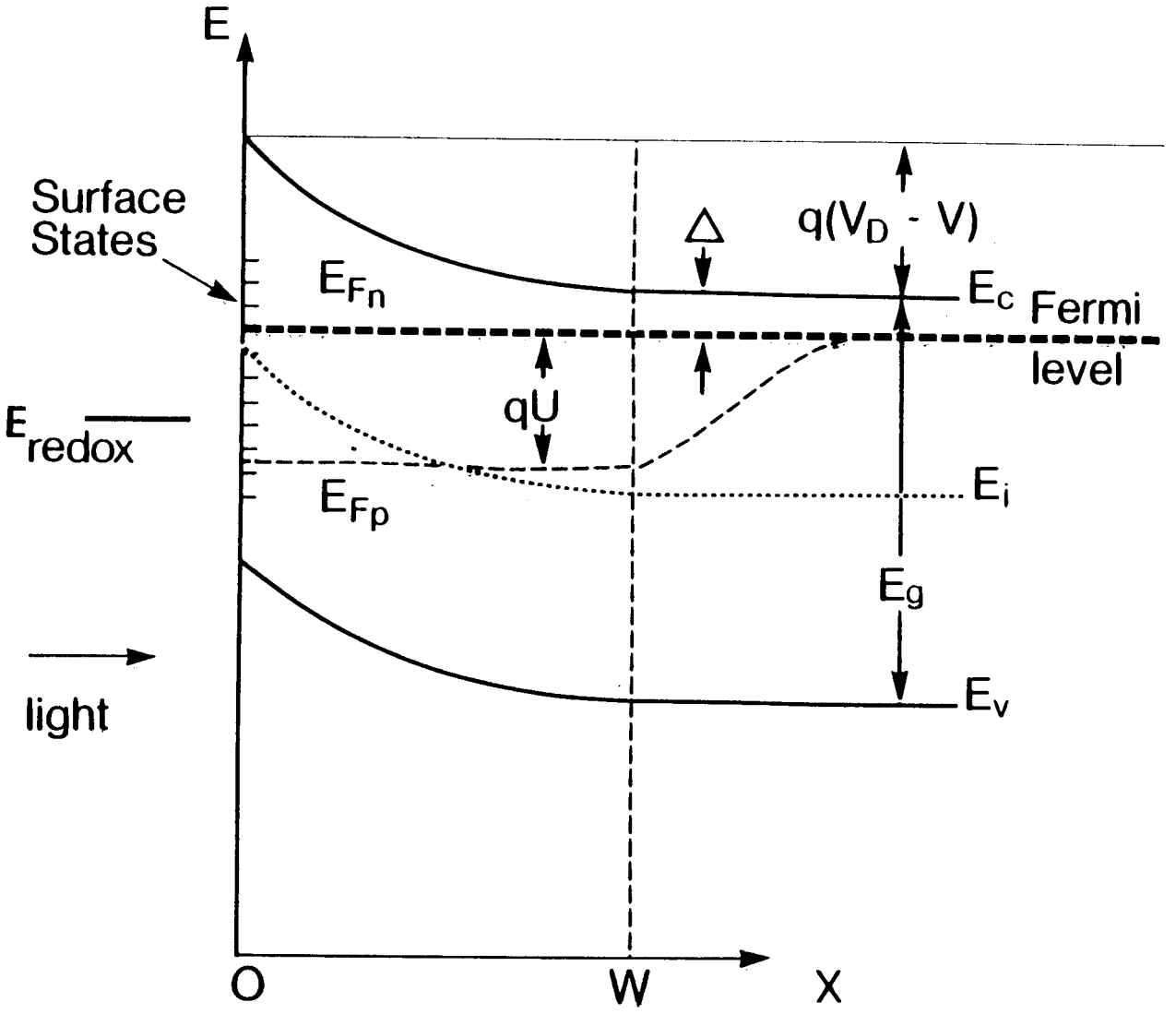
E
Surface
States
E_{Fn}
Δ
$q(V_D - V)$
E_c
Fermi
level
qU
E_{redox}
E_{Fp}
E_i
E_g
light
E_v
O
W
X

Figure 2.12 Equivalent circuit of an electrochemical solar cell, including the series and the shunt resistance, R_s and R_{sh}, respectively.

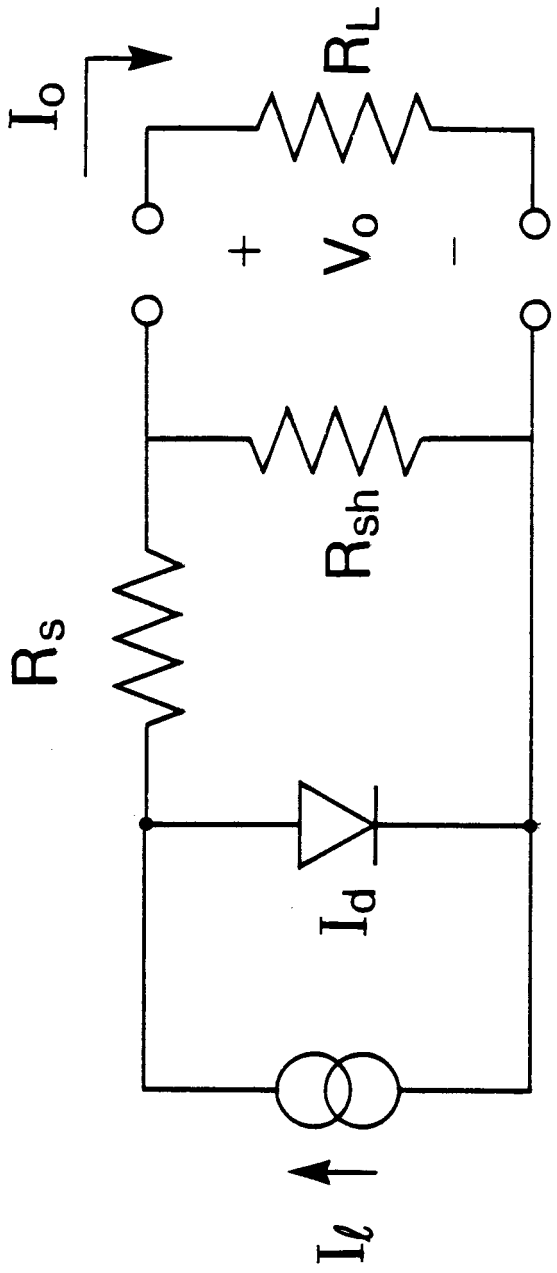
I_o
R_L
+
V_o
−
R_{sh}
R_s
I_d
I_ℓ

Figure 2.13 Calculated values of quantum efficiency vs. output voltage for different values of normalized surface transfer velocity S_t. From left to right; S_t = 0.01, 0.1, 1, and 10. Other parameters used are E_g = 1.72 eV, V_D = 0.7 V, αW_o = 0.2 $V^{-1/2}$, αL_p = 0.5, J_{po} = 10^{-14} Acm^{-2}, J_{no} = 0.1 $nAcm^{-2}$, C = 10^7, Δ = 0 eV, S_r = 0, R_s = 0 , R_{sh} = $\infty\Omega$, and kT/q = 25.8 mV. The illumination intensity was 1000 Wm^{-2} with monochromatic light of wavelength 620 nm.
(The parameters are described on page 33 in the text.)

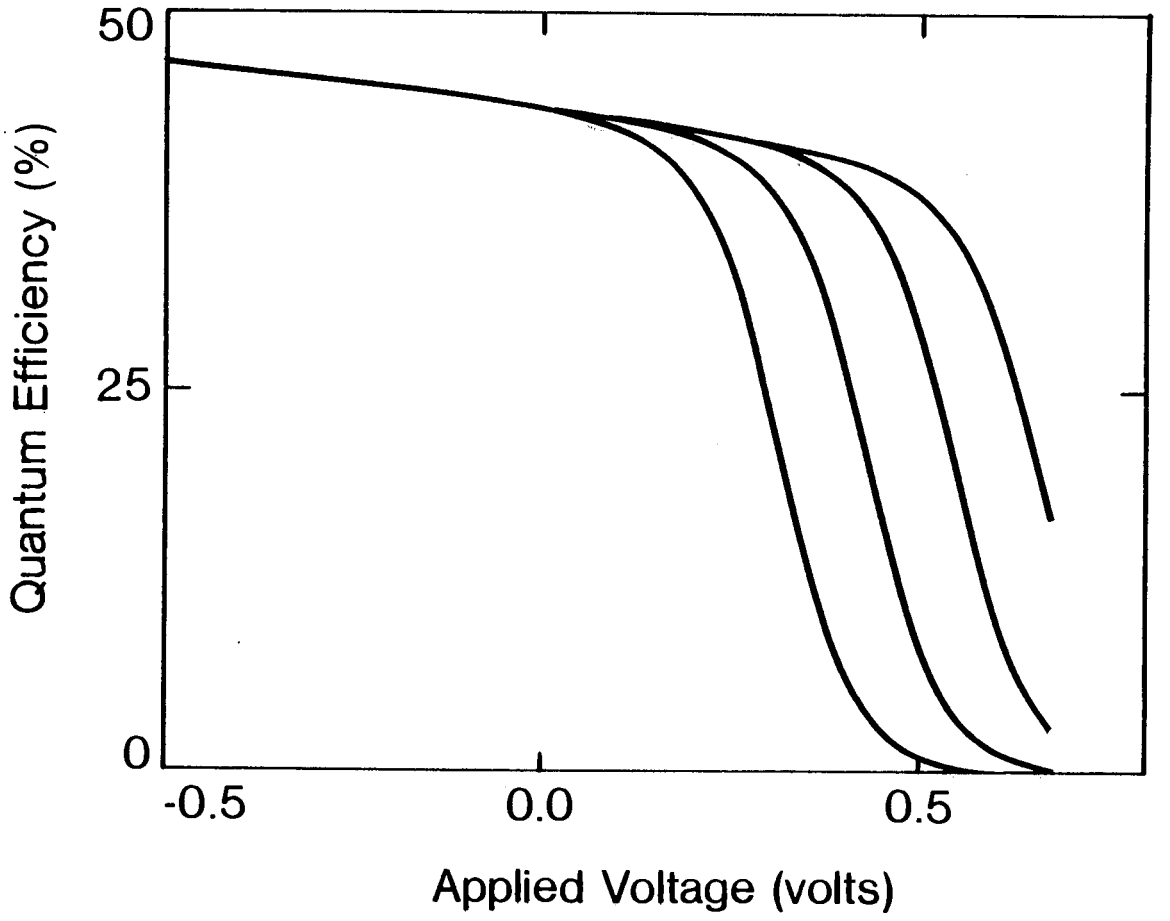
50
25
0
Quantum Efficiency (%)
-0.5
0.0
0.5
Applied Voltage (volts)

Figure 2.14 Variation of quantum efficiency with applied voltage. The circles indicate the experimental values for a 0.3 Ωcm CdSe single crystal photoanode with an illumination intensity of 0.35 mWm^{-2} at 720 nm.
The solid line is a fit of the El Guibaly model (page 33) with
E_g = 1.72 eV, V_D = 0.6 V, αW_o = .16 $V^{-1/2}$, αL_p = 0.47, J_{po} = 1 $pAcm^{-2}$, J_{no} = 10 $nAcm^{-2}$, B = 10^3, $R_s \sim 10^3 \Omega$, S_t = 0.1, and S_r = 0.2. Curves (b) and (c) were calculated from the Reiss and the Gärtner/Butler model, respectively, using the same values for αW_o and αL_p.

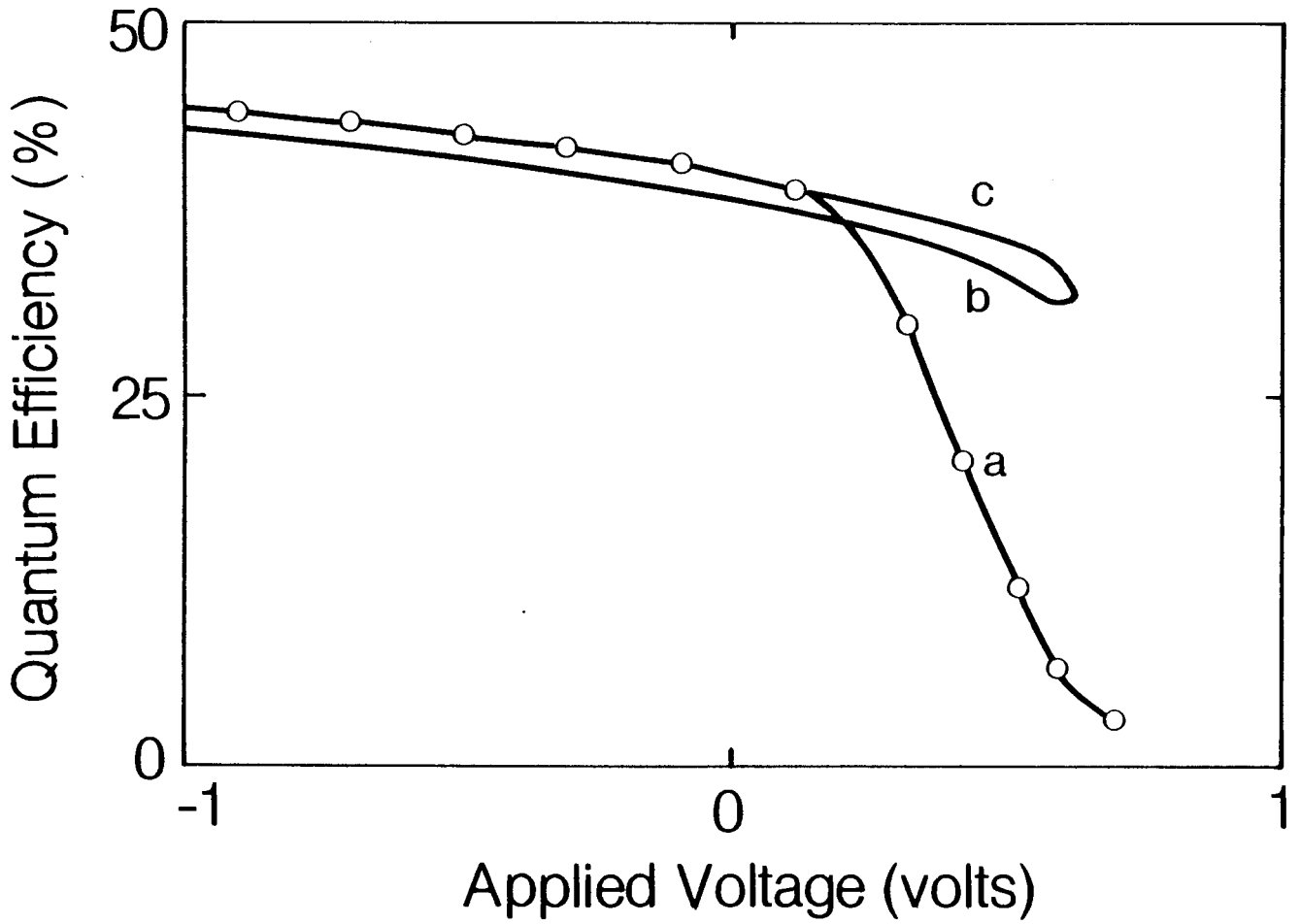
50
25
0
-1
0
1
Quantum Efficiency (%)
Applied Voltage (volts)
a
b
c

Figure 2.15 The effects of series and shunt resistance on the output I-V characteristics.

From left to right:

(a) R_s = 10, 5, 1, and 0Ω, with R_{sh} = ∞Ω for all curves,

(b) R_{sh} = 10, 50, 100, and ∞Ω, with R_s = 0Ω for all curves.

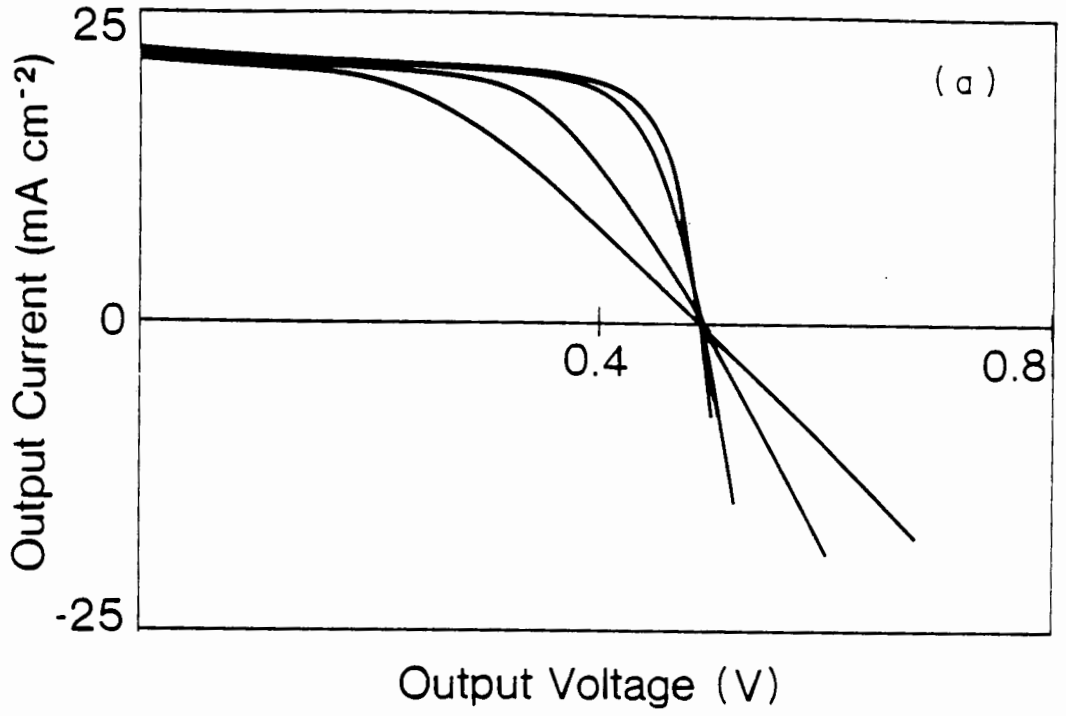
25
0
-25
0.4
0.8
(a)
Output Current (mA cm-2)
Output Voltage (V)

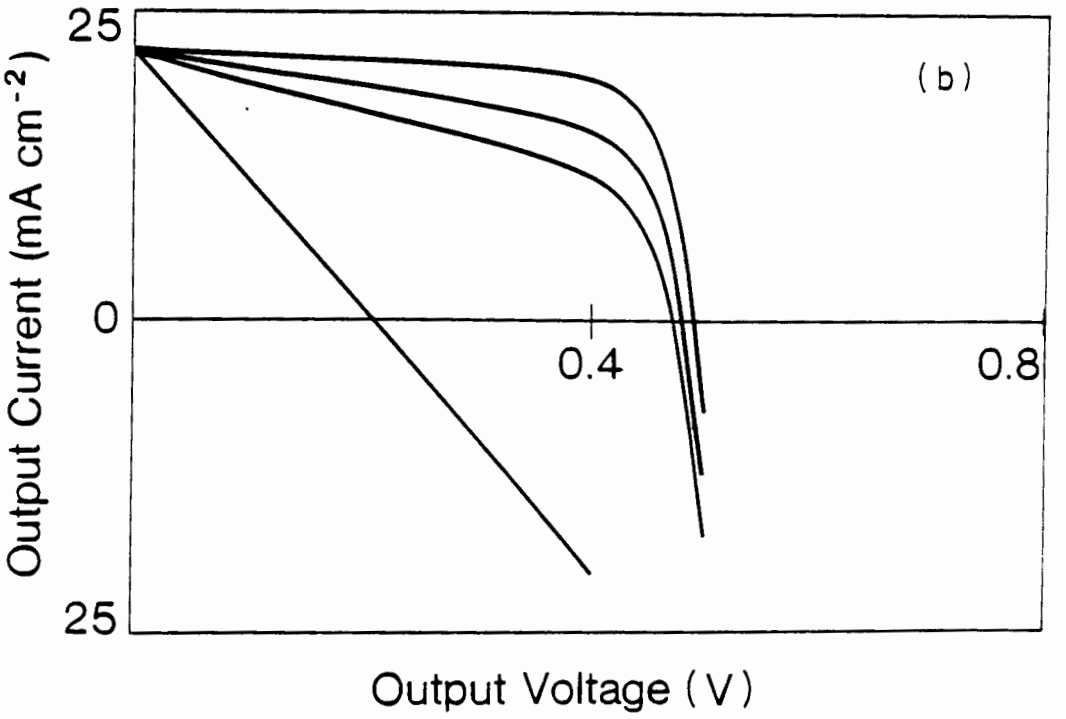
25
0
25
0.4
0.8
(b)
Output Current (mA cm-2)
Output Voltage (V)

Figure 2.16 Computed current densities versus applied voltage for varying values of surface transfer velocity S_e:

(a) $S_e = 10$,

(b) $S_e = 0.1$

(c) $S_e = 10^{-3}$.

All other parameter values are the same as in Fig. 2.14.

The current densities are normalized relative to the short circuit current density. The solid lines correspond to the net current density flowing in the cell; the squares represent current densities in the dark; the circles represent photocurrent densities.

Normalized Current (J/J$_{sc}$)
1
0
-1
0.5
Applied Voltage (volts)
a
0.5
Applied Voltage (volts)
b
0.5
Applied voltage (volts)
c

Figure 2.17 J-V characteristics in the light (solid line) and in the dark (dashed line). The current densities are normalized relative to the short circuit current density under illumination. S_e = 10, and $\gamma\Phi$ = 0.1q $cm^{-2}s$, where $\gamma\Phi$ is the decrease in bendbending due to surface states with incident photon flux Φ.

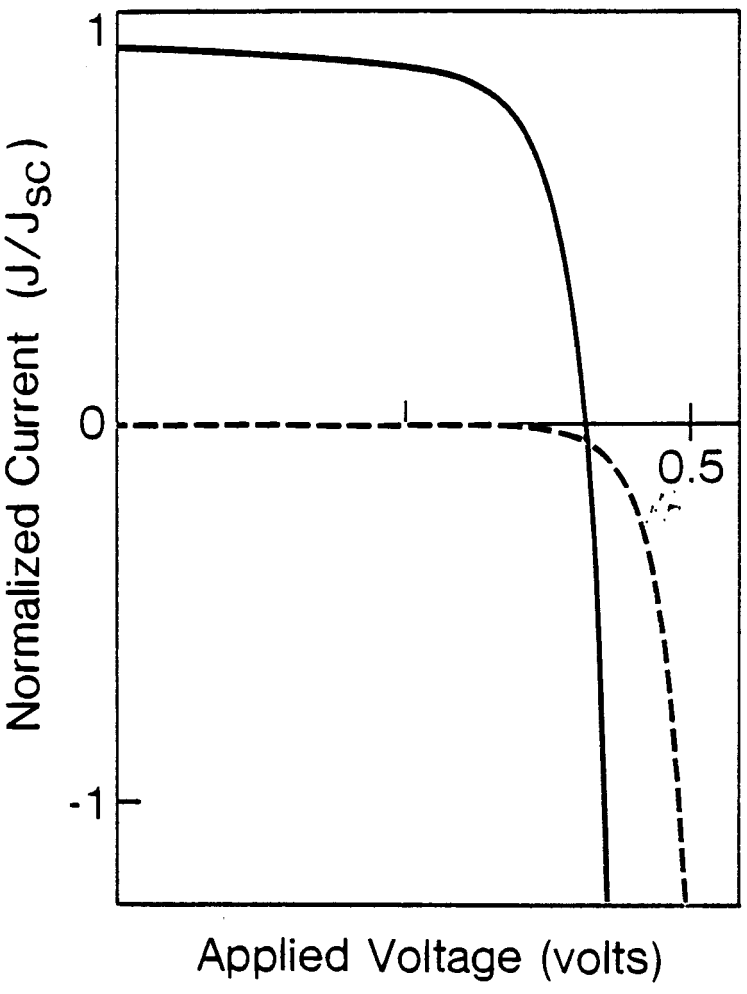
1
0
-1
0.5
Normalized Current (J/J$_{SC}$)
Applied Voltage (volts)

Chapter 3

Cadmium Selenide Electrochemical Photovoltaic Cells

Photoelectrochemical cells employing n-CdSe photoelectrodes have been under intensive study for the past eight years. Cadmium selenide photoanodes offer the possibility of high power conversion efficiencies, exhibit good stability, and show promise in achieving long lifetimes [58]. In addition, CdSe electrodes can be easily formed by various methods as thin films, at low cost and with efficiencies close to that of the single crystals. Haneman et al. [58] estimated a cost of less than $ 10 per peak watt for large-scale production of polycrystalline CdSe photoanodes with an efficiency of 5 % .

The properties and preparation techniques of polycrystalline CdSe will be summarized in this chapter. The dependence of solar performance and stability of the CdSe electrochemical photovoltaic cell on various parameters, such as electrolyte composition, light intensity, substrate material, surface texture, and semiconductor surface treatments, is analyzed.

3.1 Physical and Chemical Properties of CdSe

Cadmium selenide is an opaque, dark grey, direct bandgap semiconductor with a melting point of 1623 K [59], a density of 5.74 gcm^{-3}, and a static dielectric constant of 10 [40]. An electronegativity of 0.8 for CdSe [59] indicates that the character of the Cd-Se bond is 15 % ionic.

Cadmium selenide crystallizes in the hexagonal wurzite structure with parameters of a = 4.30 Å and c = 7.02 Å [59]; however, a zincblende structure with parameter a = 6.05 Å was reported [60] to form by vapour deposition of thin film CdSe, which then reforms under heating to the hexagonal form. Cadmium selenide occurs naturally and is called cadmoselite, which crystallizes with wurzite type of parameters a = 4.271 Å and c = 6.97 Å, and has a density of 5.8 gcm^{-3}.

The wurzite structure illustrated in Fig. 3.1a consists of two interpenetrating hexagonal close-packed lattices of Cd and Se, with a tetrahedral arrangement of four equidistant nearest neighbors, as shown in Fig. 3.1b. The lattice belongs to the type of compounds with sp^3 bonds. The conduction band of CdSe arises from the 5s orbitals of the Cd cations, and the valence band arises from the 4p orbitals of the Se anions. The valence band is split at k = 0 by crystal field and spin orbit interaction into three subbands [61], as illustrated in

Fig. 3.2. The conduction band and the valence band energy are located at -5.0 eV and -6.7 eV relative to the vacuum level, respectively [62].

The bandgap of CdSe measures 1.74 eV at room temperature for polarized light with the electric vector vibrating parallel to the c-axis of the CdSe crystal (E∥c), and 1.72 eV for E⊥c [61,63]. The bandgap increases with decreasing temperature according to 46×10^{-5} eVK^{-1} in the temperature range of 90 to 400 K for both polarizations [63].

Doping of CdSe with group III or group VII impurities results in an n-type material; group I or V materials act as p-type dopants. The failure to detect p-CdSe was associated with large activation energies (> 0.5 eV) of p-type impurities and defects [61].

Crystal defects play a major role in the photoconductivity properties. Annealing of CdSe in Cd vapor increases the dark conductivity as well as the photosensitivity; heating CdSe in Se vapor reduces the conductivity [64].

3.2 Preparation Techniques

Electrodeposition and chemical deposition of CdSe are the most widely used preparation methods, since they are low cost and have application to large-scale fabrication. Cadmium selenide electrodes prepared by other techniques such as

evaporation, coevaporation, spray pyrolysis, slurry painting, electrophoresis, and pressure sintering show promising results.

Hodes, Manassen and Cahen [65],[66] prepared polycrystalline CdSe photoanodes for electrochemical solar cells by electrolytic codeposition from an aqueous acidic solution of $CdSO_4$ and SeO_2, and obtained good solar response of the thin films after annealing for 15 min at 823 K. Chandra and Pandey [67] investigated CdSe electroplated from the same deposition bath, and found that although the concentration of $CdSO_4$ was not crucial, the concentration of SeO_2 was critical for good film quality.

Electrodeposition of CdSe from an NH_4Cl buffered plating bath containing $CdSO_4$ and SeO_2 [68] produced less favourable photoanodes than those prepared from the acidic bath. This was mainly due to much thinner CdSe layers, resulting from lower current densities at plating potentials needed for good stoichiometry.

An acidic deposition bath containing $CdCl_2$ and SeO_2 for electrodeposition of CdSe onto Ti and Ni substrates was investigated by Miller and Haneman [69]. They showed that annealing of the thin films for 2 h at 733 K had a pronounced effect on the power conversion efficiency (η increased 7-fold), while the fill factor remained unchanged. They also observed that the solar performance for the Ti substrate films was better than that of Ni. The superiority of the Ti substrate may be ascribed to the fact that the thermal expansion mismatch between

the CdSe film and the Ti substrate is less severe than between Ni and CdSe; thus, annealing will cause substantial cracking of the CdSe/Ni substrate films.

Houston et al. [70] investigated the effects of deposition potential on the solar performance of CdSe photoanodes. They found that for electroplated CdSe electrodes from an acidic $CdCl_2/SeO_2$ bath, the short circuit current and power conversion efficiency exhibit a peak-like behaviour with respect to the plating potential, while the open circuit voltage remained constant.

Cocivera et al. [71] obtained a good solar response with CdSe films electrodeposited from a bath containing Na_2SeSO_3 and Cd-nitrilo-triacetate. These films did not show the cauliflower structure observed for films electroplated from inorganic Cd^{2+} solutions. The adhesion of the CdSe to Ti substrate did not reveal any flaking, which is often observed for electroplated CdSe films.

An electrodeposition bath of KSeCN and Cd^{2+}-EDTA was used by Kazacos [72]. The photoresponse was obtained only for unannealed CdSe films and showed that I_{sc} and V_{oc} were similar to that of unannealed CdSe films prepared from acidic $CdSO_4/SeO_2$ solutions [69].

Chemical deposition techniques for preparation of CdSe thin films were investigated by various research groups [73],[74],[75],[76]. Kainthla et al. [73] prepared thin films of CdSe on Ni, Ti, and stainless steel substrates by solution

growth from an alkaline bath containing $Cd(NH_3)_4^{2+}$ and SeO_3^{2-} and obtained good solar response for CdSe grown on Ti and Ni substrates. A reduced response was obtained for the stainless steel substrate, resulting from a lower V_{oc} and a reduced fill factor. Boudreau and Rauh [75] investigated the same solution growth technique with Ti and stainless steel substrates. Again, the Ti substrate yielded the best solar characteristics; the stainless steel revealed the same I_{sc} but lower V_{oc} due to an increased cathodic dark current. The surface morphology of the thin films was found to be irreproducible due to NH_3 effusion.

Thin film CdSe photoanodes prepared by evaporation or coevaporation technique were investigated by Russak et al. [77], Reichman and Russak [78], and Bonnet [79]. The authors found that coevaporation of Cd and Se onto a Ti substrate [77],[78] or Cr-covered microscope slide [79] yielded highly stoichiometric films, which revealed little or no photoresponse without annealing, and peeled off readily from the substrate. After annealing, the crystallite size increased and a columnar structure extended from the substrate to the surface of the film without grain boundaries. Strong adhesion to the substrates and good solar response were observed [77],[78].

Spray pyrolyzed CdSe photoanodes were investigatede by Liu et al. [80],[81]. The authors found a strong adhesion of the CdSe films onto Ti substrates and observed good solar response after heat treatment of the films.

Hodes et al. [82] and Xiao and Tien [83] prepared CdSe

films by a slurry painting technique. A mixture of CdSe, fluxing material ($ZnCl_2$), and surfactant was painted onto various substrates, such as Mo, Ti, Cr, SnO_2, glassy carbon, and graphite, and then dried and annealed. Titanium, Mo, and graphite substrates were found to yield good power conversion efficiencies and fill factors, while SnO_2 showed a good fill factor but low efficiency due to a low V_{oc} as well as low I_{sc}. Glassy carbon substrates also produced a low overall photoresponse.

Thin film CdSe photoanodes on SnO_2 substrates prepared by electrophoresis [84] revealed good substrate adhesion, but only low solar response. Pressure sintered CdSe photoanodes investigated by Matsumura and Frese [85], Miller et al. [20], and Mackintosh et al. [86] showed a high solar response. Since CdSe pellets do not need a supporting substrate, higher annealing temperatures may be used.

Cadmium selenide films have also been prepared by electrolytical deposition of Cd onto a substrate and then dipping into acidic SeO_2 solution [87] or tarnishing by Se_2 vapour [88]. Both techniques resulted in CdSe films with good photoresponse.

The poor solar performance of unannealed electroplated CdSe was associated with nonstoichiometric films substantially rich in Se [89],[90]. De Silva et al. [90] found that an initial Se/Cd ratio of 3.5 reduced to 1.4 upon annealing at 723 K. They observed from X-ray photoelectron spectroscopy (XPS) and X-ray

and electron diffraction data that unannealed thin films contain quantities of uncombined Cd and Se, and possibly some amorphous CdSe. They reported that Se is liberated from the film surface during annealing which results in higher stoichiometry and Se vacancies. Chemical bonding of uncombined Cd and Se was observed as well as a 7-fold increase in the average CdSe grain size. No noticable change in the resistivity was observed.

3.3 Redox Couple Electrolytes

Cadmium selenide photoanodes employing a polysulfide electrolyte are the most widely analyzed and investigated CdSe electrochemical photovoltaic cells. However, the solar performance of CdSe photoanodes has been reported with various other redox systems, such as polyselenide and polytelluride electrolytes [32], and ferri/ferrocyanide electrolytes [91],[92],[93],[94],[95].

Ellis et al. [32] investigated CdSe photoanodes in X^{2-}/X_n^{2-} electrolytes, where X = S, Se, Te. Polychalcogenide solutions are strongly colored, but for short pathlengths they transmit an appreciable fraction of the entire visible solar spectrum [32]. Flatband potentials of CdSe electrodes in the polychalcogenide solutions, obtained from capacitance measurements, photocurrent onset, and photovoltage measurements, revealed only small differences between the various methods and

electrolytes. These differences are of no significance since CdSe preparation, etching techniques, etc. can result in vastly different photovoltages. Ellis et al. [32] found CdSe to be stable in all three polychalcogenide redox systems and obtained the highest solar response in a polysulfide electrolyte. Power conversion efficiencies on the order of 6 % and 7 % were obtained for polycrystalline and single crystal CdSe in S^{2-}/S_n^{2-} electrolyte, respectively [77],[83],[93].

Hodes, Manassen, and Cahen [65], [96] were the first to report a transformation of the CdSe surface to CdS in polysulfide solutions. The thickness of the CdS layer has a strong influence on the solar performance and stability of the cell. The Se/S exchange at the CdSe surface will be discussed in detail in the following section.

Licht et al. [97] investigated the effect of various alkali cations in a polysulfide electrolyte on the photoresponse and stability of CdSe electrochemical cells. They observed relative efficiencies of 1, 4.06, 5.09, and 5.67 for Li^+, Na^+, K^+, and Cs^+, respectively, and associated this behaviour with decreasing polarization losses according to $Li^+ > Na^+ > K^+ > Cs^+$.

Frese [91], Tenne [92], Noufi et al. [94],[95] and Reichman et al. [93] investigated the solar response of CdSe photoanodes in a ferri/ferrocyanide electrolyte. Power conversion efficiencies on the order of 12 to 14 % were observed for single crystal CdSe, mainly due to large bandbending, i.e.

V_D = 1.22 V, little or no light absorption of the electrolyte, and a good match between the valence bandedge of CdSe and E_{redox}. Reichman et al. [93] and Frese [91] anodized the CdSe electrodes to inhibit extensive corrosion in the electrolyte. Stability tests were not reported, since the electrolyte decomposes under light.

The flatband potentials and power conversion efficiencies of single crystal and polycrystalline CdSe in the various redox couple electrolytes are summarized in Table 3.1.

3.4 The CdSe / Polysulfide Electrolyte System

3.4.1 Stability

The stability of the CdSe photoanode in polysulfide electrolyte is dependent on the competition between the following two reactions:

$$CdSe + 2\ h^+ \longrightarrow Cd^{2+} + Se^0 \qquad (3.1)$$

and

$$S_n^{2-} + 2\ h^+ \longrightarrow S_n \quad . \qquad (3.2)$$

Equation (3.1) represents the corrosion of the electrode and eq. (3.2) represents the oxidation of the polysulfide electrolyte.

To determine whether the CdSe photoanode is thermodynamically stable in a polysulfide electrolyte, the overall reaction given by:

$$CdSe + 2\ S_n^{2-} \xrightarrow{2\ h^+} CdS + S_{(2n-1)}Se^{2-} \qquad (3.3)$$

must be considered. The decomposition potential (E_d) of CdSe in a polysulfide redox electrolyte, calculated from the standard free energy of the reaction in eq. (3.3), is more negative than the electrochemical potential (E_{redox}) of the polysulfide electrolyte, i.e. $E_d = -1.02$ V vs. SCE and $E_{redox} = -0.76$ V vs. SCE [98]. Thus, according to the thermodynamic model represented by Gerischer [27] and Bard and Wrighton [28], the CdSe electrode should corrode readily. However, Hodes et al. [65], Miller and Heller [30], and Ellis et al. [31] independently reported in 1976 the stabilization of CdSe photoanodes in polychalcogenide redox electrolytes. Therefore, one would predict that the overall kinetics of the polysulfide oxidation is faster than the photocorrosion process. However, if photocorrosion is the predominant reaction, a stable photocurrent will be observed if the CdSe surface is converted to CdS such that the S/Se exchange is limited to a few surface layers [98].

Hodes, Manassen, and Cahen [65],[96],[99] were the first to observe the S/Se exchange at the CdSe electrode. After operating the CdSe photoanode in S^{2-}/S_n^{2-} electrolyte, they

analyzed the electrode surface by electron microprobe analysis and found a S/Se ratio of one in the first micrometer from the surface [65].

A CdS layer on the CdSe surface will introduce a hetero-junction, which blocks the flow of holes to the semiconductor/ electrolyte interface if the thickness of the CdS layer exceeds the tunneling distance. Figure 3.3 represents the energy band diagram of the converted CdSe/CdS surface [8].

Gerischer and Gobrecht [100], Heller et al. [101], Noufi et al. [102] and De Silva and Haneman [103] also investigated the extent of the S/Se exchange. Cahen et al. [99] suggested that the $CdSe_{1-x}S_x$ surface may be insulating due to compensation of Cd donors and/or Se vacancies by S atoms. Extensive charging of the aged electrode surface during SEM studies supported their prediction. However, Heller et al. [101] and De Silva and Haneman [103] argued, that from the lattice mismatch between the CdSe and CdS, and defects in the interface region, the CdS layer becomes very conductive. De Silva and Haneman [103] observed by SEM studies that a very uneven surface morphology exists for CdSe after operation in a polysulfide solution.

Noufi et al. [102] studied the surface change of aged CdSe electrodes by X-ray photoelectron and Auger electron spectroscopic analysis (XPS and AES, respectively). Depth profiling for single crystals operated under open circuit conditions for 30 min revealed a small amount of sulfur in the first few atomic layers of the CdSe surface. However, operation

of CdSe single crystals as photoanodes showed a large amount of sulfur with the depth of the $CdSe_{1-x}S_x$ layer dependent on the operation time, due to an increase in x with time.

Gerischer and Gobrecht [100] observed by Mott-Schottky analysis a large charge increase in the surface layer of the illuminated CdSe/polysulfide system and predicted a very disordered form of an amorphous and/or polycrystalline CdSe layer.

Heller et al. [101] observed that dissolving small amounts of Se^o in the polysulfide electrolyte improved the stability of the cell substantially. Auger analysis revealed that for a Se^o concentration of 0.075 M, no S/Se exchange occured at the surface. Noufi et al. [102] observed that the depth of the S/Se exchange was dramatically reduced when the photoanode was operated in a polysulfide redox electrolyte containing 0.05 M Se^o.

If the $CdSe_{1-x}S_x$ layer is thin enough, such that hole tunneling may occur, then the solar performance should not be affected, regardless of whether the layer is insulating or conducting. However, if the layer becomes too thick for tunneling, it will act as a barrier for hole flow to the semiconductor/electrolyte interface.

Heller et al. [101] investigated the stability of both single crystal and hot pressed CdSe in a polysulfide electrolyte. The authors observed that the single crystal (0001) face was less stable than the $(11\bar{2}0)$ face with the

polycrystalline electrode lying in between. This effect was associated with the number of bonds that had to be broken in order to free Cd^{2+} [108]. The $(11\bar{2}0)$ face contains an equal number of Cd and Se atoms, while the $(000\bar{1})$ or (0001) contains either Cd or Se atoms [101]. At a high photocurrent output, the stability of the CdSe/polysulfide cell decreased rapidly, while at lower current values, the stability deteriorated more slowly. This effect suggests a competition between the photocorrosion and the sulfide oxidation reaction. As long as the hole flux to the surface can be accommodated by the S^{2-} ion and the reduced sulfur can be dissolved and transported away from the surface, strong photocurrent deterioration will not occur.

Hodes et al. [104] claim that the degradation of the photocurrent cannot result from a hole barrier at the CdSe/CdS interface, since CdS in polysulfide solution does not give rise to a barrier and is at least as unstable as CdSe in a polysulfide electrolyte. The authors suggested that an electrochemically inactive, porous CdS layer blocks the mass-transport processes in the electrolyte to and from the active semiconductor surface. This is done by impeding the dissolution and the transport of the photoreduced sulfur away from the active surface through the porous CdS layer.

Lando et al. [105] analyzed the transient photocurrents of the CdSe/polysulfide system by measuring the difference in peak current density, i.e. the current density upon onset of

illumination, and the steady state current density. The peak current represents the hole flux to the CdSe/electrolyte interface in the absence of mass transport limitations. The authors observed that the peak current density was independent of experimental parameters, while the steady state value varied with operational temperature, light intensity, electrolyte concentration and applied voltage. They reported that a S^{2-}/S_n^{2-} ratio of 1.4 and an operating temperature of 307 K resulted in the smallest transient current values. An increased stability which was observed with a polysulfide solution containing a small concentration of Se^o was associated with an increase in the sulfur dissolution rate in the polysulfide elctrolyte.

The effect of the operating temperature on the short circuit current was investigated by McCann et al. [106] and Müller et al. [107]. The short circuit current of polycrystalline CdSe/polysulfide cells increased very rapidly at temperatures between 265 and 313 K, while single crystals revealed a constant I_{sc}. This effect was associated with a low diffusion rate for S^{2-} ions which migrated from the bulk of the solution into the pores of polycrystalline CdSe and thus resulted in a depletion of S^{2-} active species in the thin film pores. The increase in I_{sc} with temperature reached a plateau between 307 and 317 K [107].

Cahen et al. [99] observed that electroplated CdSe films were considerably more stable than single crystals and thin

films prepared by other techniques. They attributed this effect to a larger real surface area with respect to the geometric surface area which resulted in reduced real photocurrent densities. Heller et al. [101] and Hodes et al. [108] observed a large increase in stability with reduced current densities. A reduction in I_{sc} from 25 to 15 $mAcm^{-2}$ resulted in a 50-fold increase in stability [108].

Tenne [109] observed an increased output stability for CdSe photoanodes in polysulfide electrolyte under chopped light illumination. He associated this effect with an increase in hole transfer across the interface caused by sulfur dissolution from the electrode surface during the dark cycle.

3.4.2 Surface Etching

Surface states caused by polishing and/or cutting in single crystals, and impurity adsorption on the surface of polycrystalline or single crystal CdSe can be removed by various etching techniques.

Heller et al. [110],[111] observed a large increase in photoresponse of single crystal CdSe after etching and ascribed this effect to the removal of charge trapping surface states. The authors investigated the spectral response of single crystal CdSe by using a two-beam method in which strong continuous laser light populated surface states, while the spectral response was observed with a low intensity measuring beam. They observed a

smaller photocurrent density for short wavelength illumination, which is absorbed close to the crystal surface where a high density of traps exists, than for long wavelength illumination which is adsorbed further away from the surface. Damaged surfaces revealed a sub-bandgap response which was removed by etching.

De Silva and Haneman [112] observed by XPS technique an increase in the Se/Cd ratio after etching CdSe in dilute aqua regia due to Se^{o} on the surface.

Hodes et al. [108] and Tenne et al. [113],[114] investigated the effect of photoetching on the solar performance of CdSe/polysulfide cells. Photoetching results when the CdSe photoanode is operated under illumination in a corrosive electrolyte. Hodes et al. [108] attributed a 50-fold increase in stability after photoetching a smooth, polished single crystal electrode surface, to an increased surface roughness, and thus increased active surface area. Tenne [113] observed after photoetching of single crystal CdSe, an increase in surface area of approximately 50 % due to the formation of pits. This caused the reflectivity of incident light to become negligible which partly explains the effect of photocurrent enhancement ater photoetching. A large increase in the cathodic dark current was observed in single crystals after prolonged photoetching. This effect was much less pronounced in polycrystalline electrodes due to the larger dark current prior to photoetching [113].

Liu et al. [80] investigated the effect of photoetching with neutral or weakly acidic NaCl solutions on spray pyrolyzed CdSe films. Photoetching occured only if the pH of the NaCl solution was lower than 12 due to precipitation of $Cd(OH)_2$ or oxide species on the CdSe surface at higher pH, which blocked further photocorrosion. The authors observed an inreased photocurrent, increased fill factor, and a reduction in surface reflectivity after photoetching.

3.4.3 Specific Ion Adsorption

Various ion treatments of CdSe electrodes have been found to increase the open circuit voltage. Hodes et al. [82] were the first to use a $ZnCl_2$ dip to increase the photovoltage in slurry painted CdSe thin films. Tenne [113] reported an increase in photovoltage due to a decrease in the cathodic dark current by Zn^{2+} ion treatment. The increase in solar performance was found to be larger in polycrystalline CdSe photoanodes than in single crystals. He explained the reduction in cathodic dark current by an analogy to MIS structures, where the metal (M), the insulator (I), and the semiconductor (S) are represented by the electrolyte, the ZnS layer, and CdSe, respectively. Since the transfer of majority carriers across the CdSe/ZnS interface depends on the rate of tunneling through the insulating layer, the thickness of the ZnS layer and the relative positions of the bandedges of CdSe with respect to ZnS

determine the cathodic dark current.

Reichman and Russak [115],[116] investigated CdSe/ZnSe heterostructure, thin film electrodes prepared by elemental vacuum evaporation of a ZnSe film onto evaporated CdSe thin films, followed by annealing in air which changed the surface to ZnO. On operation in polysulfide electrolyte, the ZnO layer was converted to ZnS. The ZnS layer was found to extend to a depth of 80 to 100 Å and was mixed with CdSe after 20 Å. The structure revealed an increased V_{oc} resulting from a reduced dark current. Similar photocurrent-voltage characteristics of etched and non-etched electrodes led to the conclusion that the increased V_{oc} is not a result of a shift in flatband potential. By dipping a coevaporated CdSe electrode into a 1 M $ZnCl_2$ solution, Reichman and Russak [115] observed an increased V_{oc} and an increased solar efficiency. They reported a negative shift in flatband potential resulting in larger bandbending, due to an increased electron affinity of the ZnS surface for $ZnCl_2$ dipped CdSe electrodes.

Tomkievicz et al. [89] observed that dipping an electroplated CdSe photoanode in $GaCl_3$ solution had a similar effect on the photovoltge and cathodic dark current, as was observed for $ZnCl_2$ dipping. However, dipping the electrode in $RuCl_3$ solution resulted in a reduction of the photovoltage. They observed an apparent correlation between cell effects on the performance of the cell and the catalytic effects of the adsorbed metal ion on the H_2 evolution reaction. If the dark

current resulted partly from H_2 evolution at the electrode, then Ga^{3+} ions, a known poison of the H_2 evolution reaction, would result in a decreased dark current [89], and Ru^{3+} ions, a known catalyst for H_2 evolution, would show an increase in dark current, and thus a reduction in V_{oc}. For both Zn and Ga dipping, the magnitude of the observed effects varied between electrodes and was most significant with electrodes which had a poor solar performance [89].

3.4.4 Lifetime

Hodes et al. [104] studied the long term stability of slurry-painted CdSe electrodes with a power conversion efficiency of 3.9 % in a polysulfide electrolyte for eight months and observed a deterioration in efficiency after two months of operation due to a decreased I_{sc}. A battery arrangement of seven 3 cm^2 painted and photoetched CdSe thin film cells with an overall efficiency of 3 % revealed absolute stability for five months. The subsequent decrease in efficiency was associated with electrolyte leakage of the cells. The long stability of the battery may be attributed to the removal of trap centers by photoetching prior to operation, and to a low current density.

Haneman et al. [58] investigated the lifetime dependence of chemically deposited thin film CdSe electrodes with a power conversion efficiency of 5 % [73] on various experimental

parameters, such as polysulfide electrolyte concentration, different substrate materials, $ZnCl_2$ dipping, and various electrode coatings. Decay rates of I_{sc} were reported for up to eighteen months. An initial increase in V_{oc} and fill factor resulted in a constant power conversion efficiency between one and several weeks before η began to decay according to the decrease in I_{sc}.

Haneman et al. [58] observed little or no effect of the OH^- concentration on the lifetime of the CdSe electrode. However, a strong dependence of the S^{2-}/S_n^{2-} ratio on the lifetime was observed, with a ratio of 1.6 resulting in highest stability. Severe photocurrent decay rates observed with low sulfur concentration were attributed to the decomposition of the CdSe surface.

Cadmium selenide deposited on Ni or Ti substates showed similar photocurrent decay rates. The stability of $ZnCl_2$ dipped electrodes was substantially reduced with respect to untreated CdSe [58].

An oxide layer on the CdSe surface, induced by heating the thin films in air at 470 K for 10 to 40 min revealed a reduced photocurrent decay rate. Cadmium selenide coated with a thin layer of Au or Pt by sputtering or evaporation techniques showed a stability similar to uncoated samples. An acrylic layer on CdSe lowered the decay rate substantially, possibly due to a much reduced photocurrent [58].

Most electrodes revealed a photoresponse decrease of larger

than 50 % in five months, but a single "superior" sample showed a solar performance decay of less than 40 % after eight months of continuous operation [58]. Although this result was irreproducible, it indicates that further improvements in lifetime are possible.

Table 3.1 Flatband potentials (E_{fb}) and power conversion efficiencies (η) for CdSe electrochemical photovoltaic cells with various aqueous redox couple electrolytes.

Sample	Electrolyte	Flatband Potential [V]	Efficiency [%]	Ref.
Single Crystal	S^{2-}/S_n^{2-}	−1.63	7.2	93
	S^{2-}/S_n^{2-}	−1.50		100
	S^{2-}/S_n^{2-}	−1.45		32
	Se^{2-}/Se_2^{2-}	−1.40	2.1	32
	Te^{2-}/Te_2^{2-}	−1.45	1.5	32
	$[Fe(CN)_6]^{3-/4-}$	−0.96	14.2	93
Pressed	S^{2-}/S_n^{2-}	−1.34	5.1	20,57
Vac Dep	S^{2-}/S_n^{2-}	−1.30	6.0	57,77

Figure 3.1 The crystal structure of CdSe

(a) Wurzite lattice [40b]

(b) The stacking of tetrahedral layers of Cd and Se in the hexagonal CdSe. [59] The stacking sequence is 01010... .

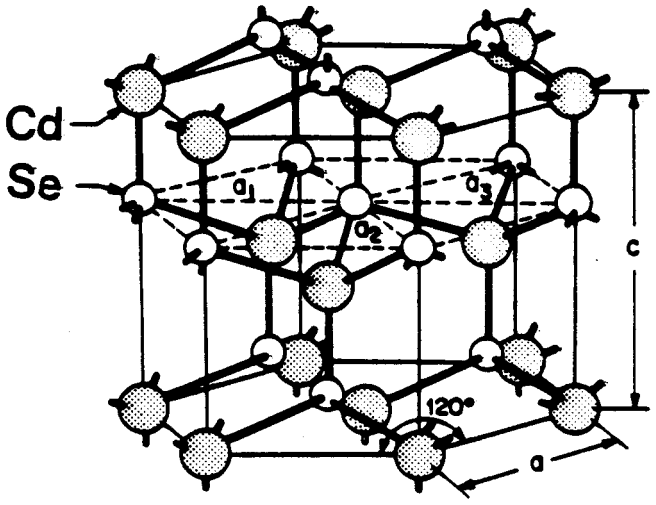

a

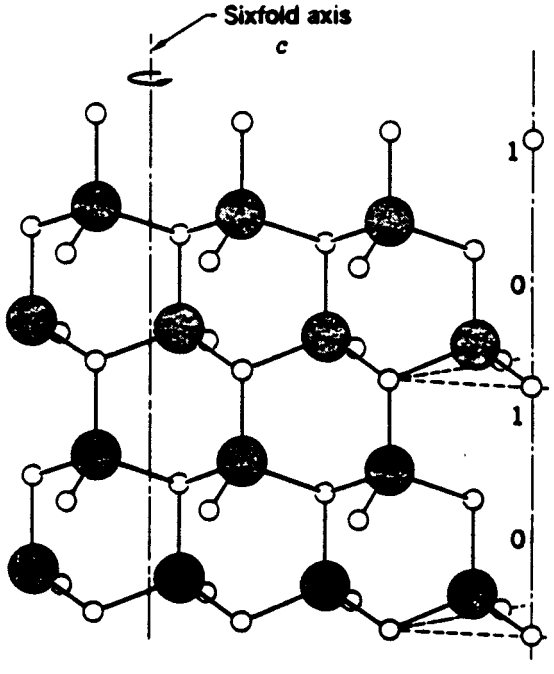

b

Figure 3.2 Band diagram at k = 0 of CdSe at room temperature. The valence band is split into three sub-bands with a separation of 0.026 eV and 0.44 eV between the valence bandedge and the sub-bands.

E_c = conduction bandedge

E_v = valence bandedge

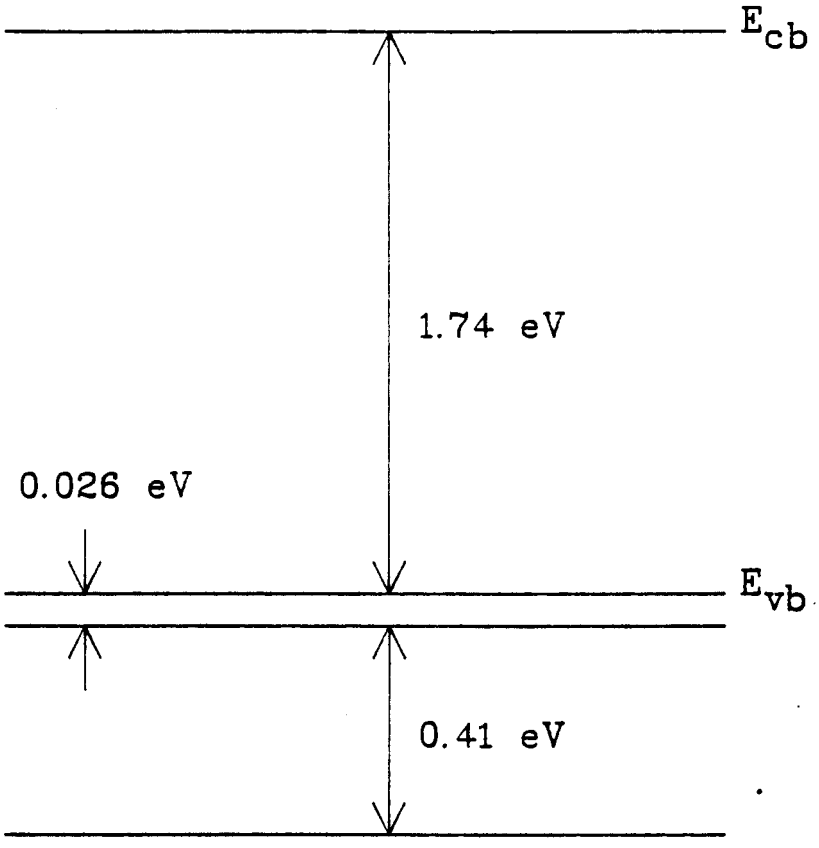
E_{cb}
1.74 eV
0.026 eV
E_{vb}
0.41 eV

Figure 3.3 Energy level diagram for CdSe with a surface layer of CdS

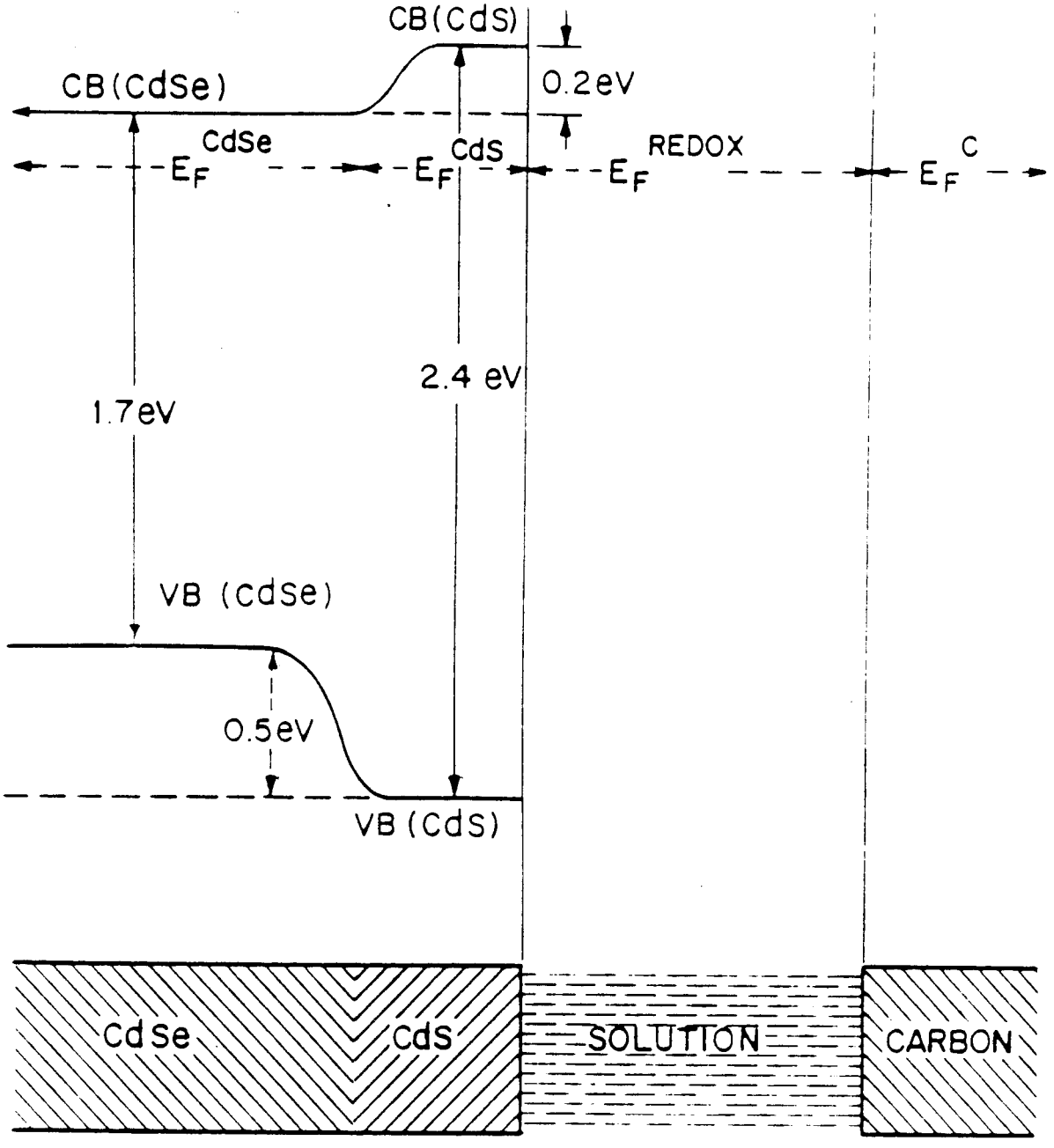
CB(CdS)
CB(CdSe)
0.2eV
CdSe
E_F
CdS
E_F
REDOX
E_F
C
E_F
2.4 eV
1.7eV
VB (CdSe)
0.5eV
VB (CdS)
CdSe
CdS
SOLUTION
CARBON

Chapter 4

Materials And Methods

4.1 Electrodeposited Cadmium Selenide Electrodes

Titanium discs (1 cm diameter, cut from foil of 99.7 % purity and purchased from Alfa Products in Danvers, Massachusetts) were abraded with Scotch Brite (3M Canada Ltd., London, Ontario), rinsed in acetone and distilled water, and then etched in 4 % HF for 30 s. After a Ti wire was spot-welded to each disc, the substrate side with the attached wire was then coated with nail polish to avoid electrodeposition of CdSe on both sides of the Ti substrate.

For the deposition of CdSe, the working electrode (Ti disc) was faced by a large stainless steel counter electrode 5 times the area of the Ti substrate. A saturated calomel electrode (SCE) was placed close to the working electrode. The deposition bath was stirred at a constant rate by a magnetic stirrer. All potentials were measured versus SCE.

Electrodeposition of the CdSe was performed at a constant potential of -0.72 V vs SCE for 15 min using a Wenking

Potentiostat (G. Bank Elektronik, West-Germany). The acidic plating solution, prepared from reagent grade chemicals (BDH Chemicals) consisted of:

1 M H_2SO_4

0.5 M $CdSO_4$

0.01 M SeO_2

The average thickness of the CdSe layer was 10±2 μm as determined with an Etec Autoscan Electron Microscope Model U1 (SEM). Weighing the electrode before and after electrodeposition and using the literature density and the geometric area of the deposit verified the thickness of the deposit.

The deposition bath was examined polarographically using a Princeton Applied Research (PAR) Potentiostat Model 170. The working and counter electrodes were Ti and Pt respectively, and the reference electrode was the SCE. In the voltammogram (Fig. 4.1), the reduction of Cd^{2+} to Cd metal is indicated by the steep current increase with onset at -0.72±0.01 V. The maximum observed at -0.64+0.01 V can be ascribed to Se formation [117],[68]. Deposition potentials close to -0.68±0.01 V and -0.76±0.01 V resulted in deposits rich in Se, indicated by a reddish color, and rich in Cd, with needle like crystals at the electrode's edge, respectively. At -0.72±0.01 V, the deposit appeared uniform and dark grey in color, indicating CdSe formation.

A detailed investigation of the potential range between

-0.70 V and -0.78 V showed that electroplating of CdSe at -0.72 V vs SCE resulted in electrodes with optimum solar cell performance, as can be seen in Table 4.1 [118].

High plating current densities at the desired plating potentials were obtained and resulted in a CdSe layer of 10 μm thickness and a rough surface morphology, which is desirable for good solar performance.

Red Se deposits were observed if the deposition times were too long, even at plating potentials of -0.72 V. The growing CdSe deposit introduced an increasing resistance between the Ti and the deposition bath. The resulting voltage drop across the deposit was reflected by an increasingly more positive potential at the CdSe/deposition bath interface, favoring Se deposition. The deposition process of CdSe is described in detail in Appendix B.

The performance of an electroplated CdSe electrode is highly dependent upon its substrate material. Substrates, such as steel, Ni, Ti, Cu, C and Al were tested. Electroplating CdSe onto Cu, C and Al was not possible. Ti substrates yielded the best CdSe solar cells.

The electroplated samples were heated in a quartz tube furnace at 873 K for 15 min under a vacuum of 10^{-3} torr. This annealing resulted in considerable improvement in the solar performance of the CdSe photoanodes.

The electroplated CdSe samples were mounted in a plexiglass holder with Easypoxy (Conap Inc., Olean, New York), and dried

for 24 h.

4.2 Cold Pressed Cadmium Selenide Electrodes

Cadmium selenide powder (99.9 % purity, 5 μm mesh) was obtained from Cominco Ltd. (Trail, British Columbia). The powder was prepared by reacting a 0.5 M $CdSO_4$ solution with H_2Se gas at 353 K. Samples of 200±2 mg were cold pressed in a carbon steel press at different pressures (11.5, 23, 46 and 69 MPa) and for two different periods of time (5 min and 2 h). Emission spectrographic analysis by Cominco Ltd. of the high purity powder showed the following impurities (in ppm):

Al 30	B 3	Ca 30	Ga 10	In 2
Fe 30	Pb 5	Mg 20	Mn 2	Si 200
Ag <0.1	Sn 4			

The resulting discs, 10 mm diameter and 0.5 - 0.7 mm thick were annealed at 873 K for 6 h under vacuum. Due to material costs, it is desirable to produce the thinnest self-supporting pellets possible. However, discs which were less than 0.25±0.02 mm thick became too fragile to be useful as photoelectrodes. Self-supporting pellets have the advantage that microcracks resulting from differential thermal expansion between the substrate and the CdSe during annealing may be avoided.

The density of the discs was measured before and after annealing using both a micrometer and a Mettler H20 Balance.

Pellets prepared at various pressures were cut in half. One half was used as a photoanode to determine its solar performance, and the other half was used for resistivity measurements.

A study of optimum annealing temperature was performed on electrodes pressed from 150±5 mg CdSe powder at 46 MPa for 5 min. The pellet thickness ranged from 0.20 -0.40 mm.

Ohmic contacts were formed by rubbing a thin layer of In-Ga (25:75 by weight) eutectic onto a slightly abraded sample surface. The pellets were attached with Electrodag 415 (Acheson Colloids Canada Ltd., Brantford, Ontario) to a clean, abraded copper disc, with a copper wire soldered to the other side. The assembly was mounted on a plexiglass holder using Easypoxy .

4.3 Single Crystal Cadmium Selenide Electrodes

Precut single crystal CdSe (C-plate) of 0.25 cm^2 area and 0.1 cm thickness and a raw ingot of single crystal CdSe were obtained from Cleveland Crystals (Cleveland, Ohio). The crystals were grown from a CdSe vapour phase. The resistivities of the crystals were 0.3Ωcm and 2 MΩcm respectively. The ingot was cut into 1 mm thick C-plates of approximately 0.25 cm^2 area.

Emmission spectrographic analysis by Cominco Ltd. of the

two different single crystal CdSe batches showed the following impurities (in ppm):

Precut crystals

Al 0.2	Ca 0.5	Cu 10	Fe 0.1	Pb 0
Mg 0.1	Mn 0	Si 15	Ag 0	Sn 0
Bi 1	Ni 0.5			

Ingot

Al 1	Ca 0.1	Cu 20	Fe 2	Pb 0.5
Mg 0.05	Mn 1	Si 70	Ag 0.5	Sn 0.2
Bi 0.5	Ni 3	Zn 100		

In an attempt to improve the poor solar performance of these crystals, the samples were annealed for 6 h at 873 K under vacuum or in sealed evacuated quartz tubes in the presence of elemental Se or Cd.

Ohmic contacts and the mounting of the crystals were identical to that of the pressed pellets as described on page 87.

Anodization of the single crystal electrodes was achieved in saturated KCl solution by 30 min white light illumination (1000 Wm^{-2}) at short circuit. A Se layer of 0.27±0.03 µm thickness, as calculated from integrated photocurrent i.e. total charge flow measurements [91],[119],[120] was formed on the CdSe surface by photocorrosion.

4.4 Treatment of CdSe Electrodes with Zn^{2+} and Hg^{2+} Solutions

Ions adsorbed by the surface and grain boundaries of the photoanodes will cause considerable changes in the solar performance.

Pressed CdSe electrodes (0.35±0.02 mm thick, pressed from 150+5 mg powder at 46 MPa for 5 min, annealed for 6 h at 873 K) and electroplated samples were dipped or boiled for various lengths of time in a 1 M $ZnCl_2$ or 1 M $HgCl_2$ solution.

Prior to testing, all CdSe electrodes were etched for 1 min in a 50 % H_2O_2 and glacial acetic acid solution in the ratio of 1 : 3, unless indicated otherwise.

4.5 The Test Cell

The test cell (Fig. 4.2) consisted of a quartz tube, 6 cm in diameter, with an optical flat bottom window. The electrode was fitted through a tight teflon lid, which allowed the system to be fully sealed from the atmosphere, and also enabled flushing of the system with N_2 prior to and after introducing the redox couple electrolyte into the cell.

The electrolyte was prepared and stored under N_2

atmosphere. It consisted of the following reagent grade chemicals (BDH Chemicals):

1 M NaOH

2 M Na_2S

1 M S^o

0.01 M Se^o

The absorption spectrum of the electrolyte (Fig. 4.3) was measured with a Pye Unicam Spectrometer Model 8000.

The light entered the test cell through the bottom window, passing through 3 mm of electrolyte between the window and the CdSe electrode. The photoanode was faced by a large Pt counter electrode ring of 5 cm^2 area.

The reference electrode (SCE) was made by amalgamating approximately 1 g Hg with a few mg Hg_2Cl_2 and immersing it in saturated KCl solution in a glass tube. A Pt wire pierced through the bottom of the tube, connecting the amalgam to the outside circuit. A salt bridge (KCl in agar) connected the SCE to the solar cell. The reference electrode was calibrated against a Fisher Scientific Calomel Reference Electrode Model 13-639-52.

4.6 Current-Voltage (I-V) Characteristics

Fig. 4.4 illustrates the experimental arrangement for measurement of the I-V characteristics of the CdSe electrodes under white light illumination from a tungsten halogen lamp (Canadian General Electric, ELH 120 V, 300 W). The CdSe electrode was biased by means of a PAR Potentiostat Model 173 in combination with a Universal Programmer Model 175. The spectra were recorded at a rate of 20 mVs^{-1}.

The irradiance on the test cell was measured by means of a Tektronic J16 Digital Photometer.

4.7 Quantum Efficiency-Voltage (η_q-V) Characteristics

The change in quantum efficiency with forward bias voltage was measured using the experimental arrangement shown in Fig. 4.5. Helium-Neon laser light (Spectra Physics Model 125), chopped at 20 Hz, was incident on the solar cell with an intensity of 140 Wm^{-2}. The forward bias was controlled with the PAR Potentiostat and scanned at a rate of 2 mVs^{-1}. The current response was fed into a Lock-In amplifier (PAR Model HR-8) and then recorded on an X-Y recorder (Hewlett-Packard Model 700AR).

4.8 Spectral Response (η_{sc}-λ)

The wavelength response of the electrodes was obtained under short circuit conditions using a 100 W tungsten halogen lamp (Philips, 12 V). Figure 4.6 illustrates the measurement apparatus. White light, chopped at 20 Hz, was passed through a grating monochromator (Jarell-Ash, 8 nm resolution) onto the solar cell. The current response, as measured by the potentiostat was fed into the Lock-In Amplifier and then recorded on the X-Y recorder.

Since the illumination intensities at the crystal surface were very low (0.2 - 0.4 Wm^{-2}), some cells were illuminated with continous laser light (He- Ne Laser, Spectra Physics Model 133) of 10 Wm^{-2} intensity at the electrode surface in addition to the weak monochromatic measuring beam.

All light intensities measured with the Tektronic Photometer were corrected for electrolyte absorption.

Since the potentiostat in Figures 4.4 - 4.6 was not available for the earlier experiments, the circuit shown in Fig. 4.7 functioned as such. The semiconductor electrode was biased manually using a rheostat connected to a 6 V battery, and the current response of the solar cell was determined across a 10 Ω load resistor.

Some experiments were repeated with the potentiostat arrangements and revealed identical results.

4.9 Resistivity

The resistance of the pressed electrodes was measured with the experimental arrangement shown in Fig. 4.8. The Interstate Electronics Corporation Function Generator (Model F34) supplied a triangular voltage ramp across the sample. The current, determined by the voltage drop across a 1 kΩ load resistor was recorded as a function of applied voltage on the X-Y recorder.

The back contact (In/Ga) of the single crystal and pressed CdSe electrodes was found to be ohmic within the applied voltage range of 1 V.

4.10 Scanning Electron Micrographs

Images of the CdSe samples were obtained using the Autoscan Electron Microscope. The images were recorded on Ilford FP4 film.

Table 4.1 Solar performance at 1000 Wm^{-2} white light illumination of CdSe electrodes, electroplated onto Ti substrate at various constant negative plating potentials, ϕ.

(V_{oc} = open circuit voltage,

I_{sc} = short circuit current)

ϕ [mV]	V_{oc} [mV]	I_{sc} [$mAcm^{-2}$]	Fill Factor
700	680	8.2	0.42
710	643	9.0	0.41
720	632	10.0	0.44
730	662	7.6	0.39
740	647	9.9	0.43
750	567	7.2	0.39
760	505	5.3	0.50
770	575	4.0	0.56
780	545	7.1	0.53

Figure 4.1 Voltammogram of the deposition bath:

1 M H_2SO_4

0.5 M $CdSO_4$

0.01 M SeO_2

The working and the counter electrode were Ti and Pt, respectively.

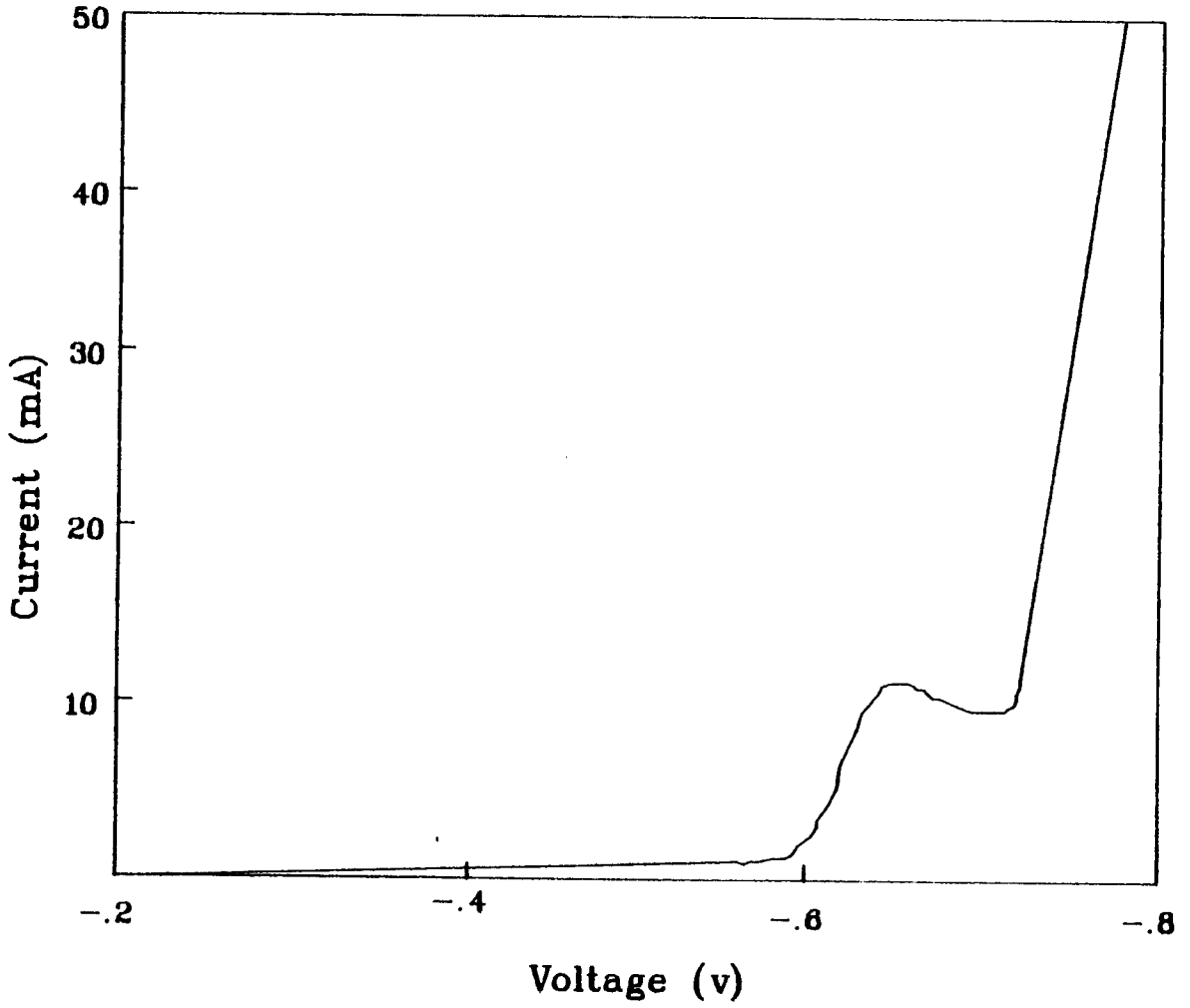
50
40
30
20
10
Current (mA)
-.2
-.4
-.6
-.8
Voltage (v)

Figure 4.2 The test cell containing a CdSe electrode, Pt counter electrode, and SCE reference electrode in polysulfide electrolyte.

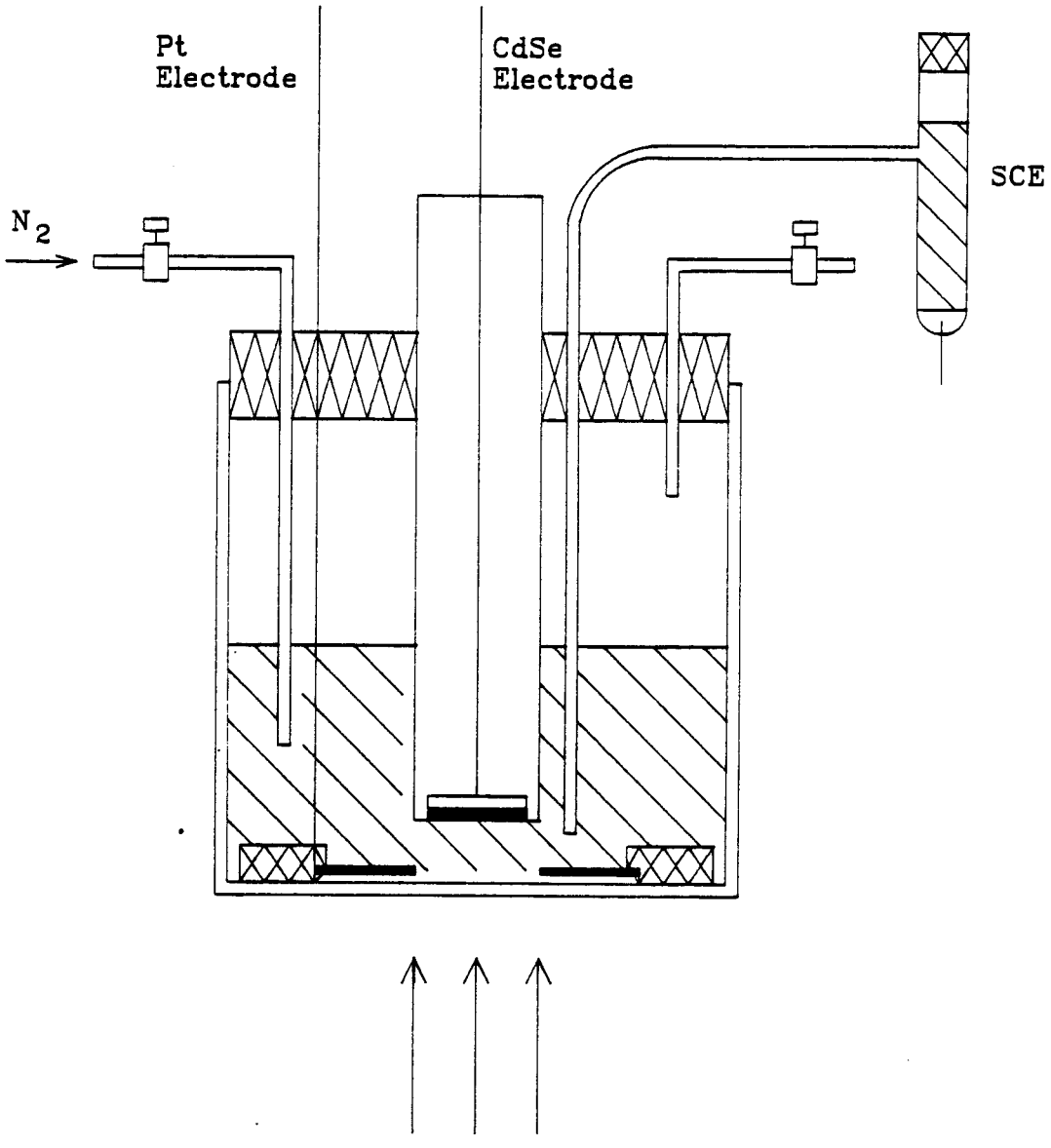
Pt
Electrode
CdSe
Electrode
SCE
N_2
Light

Figure 4.3 Absorption spectrum for 10 mm pathlength of the sulfide/polysulfide redox electrolyte, containing:

1 M NaOH

2 M Na_2S

1 M S^o

0.01 M Se^o.

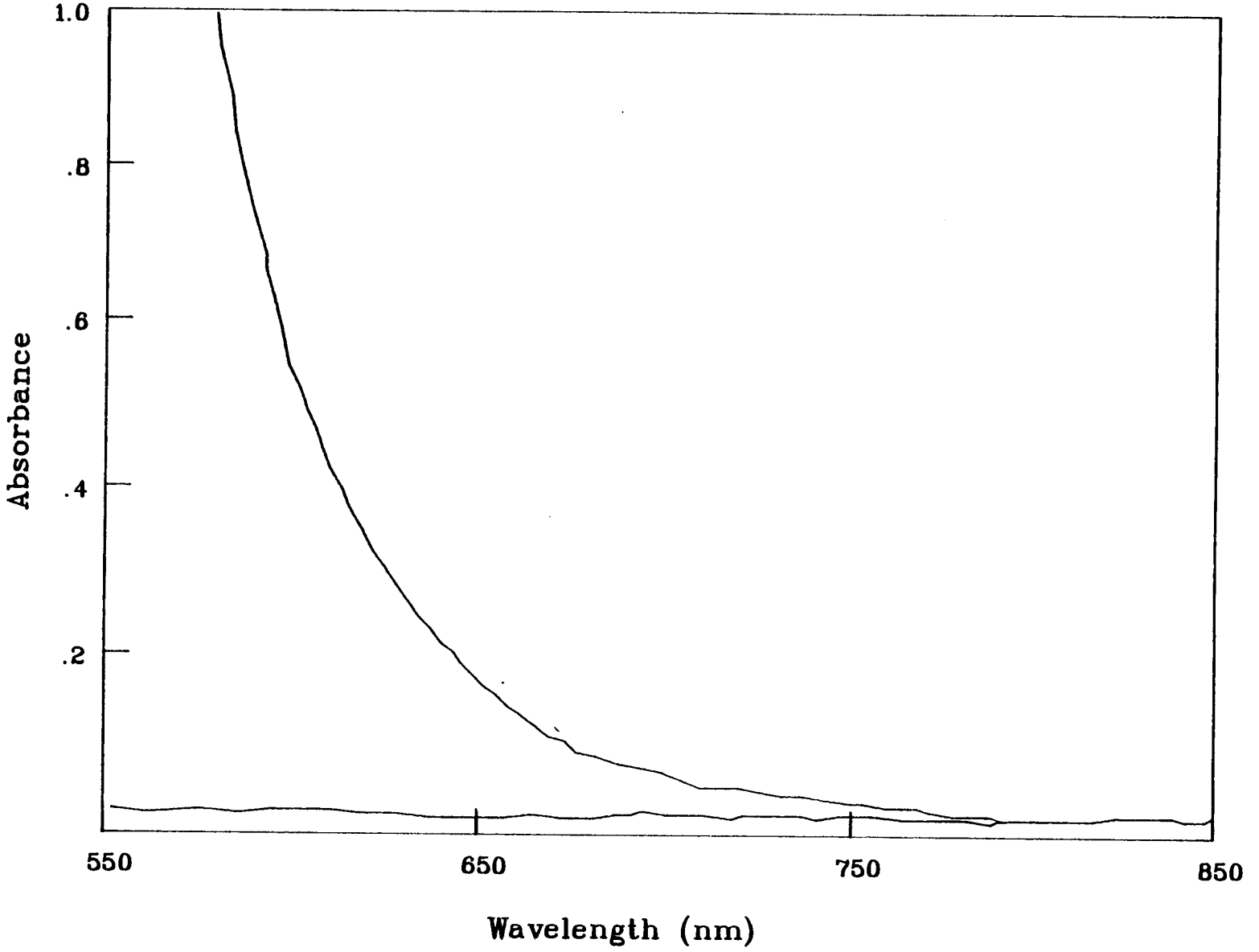
1.0
.8
.6
.4
.2
Absorbance
550
650
750
850
Wavelength (nm)

Figure 4.4 The measuring apparatus with white light illumination to determine current-voltage characteristics.

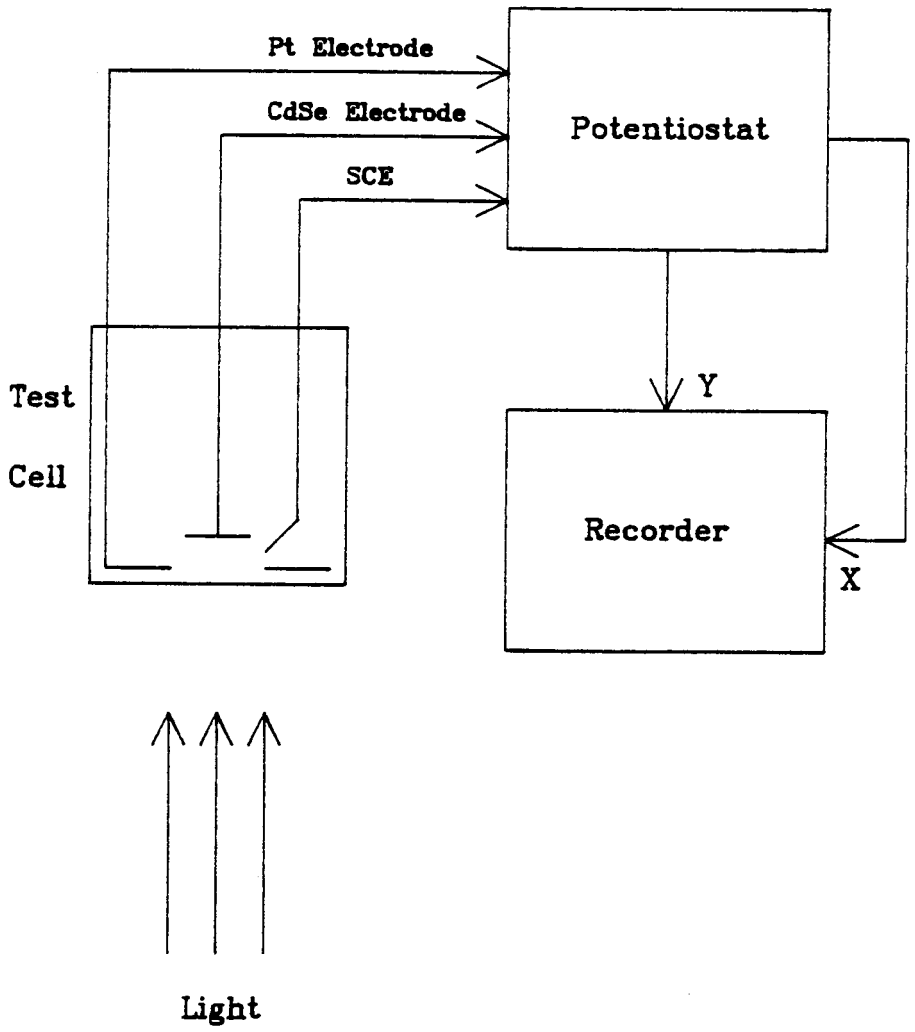
Pt Electrode
CdSe Electrode
SCE
Potentiostat
Test
Cell
Y
Recorder
X
Light

Figure 4.5 The measuring apparatus to determine quantum efficiency-voltage characteristics.

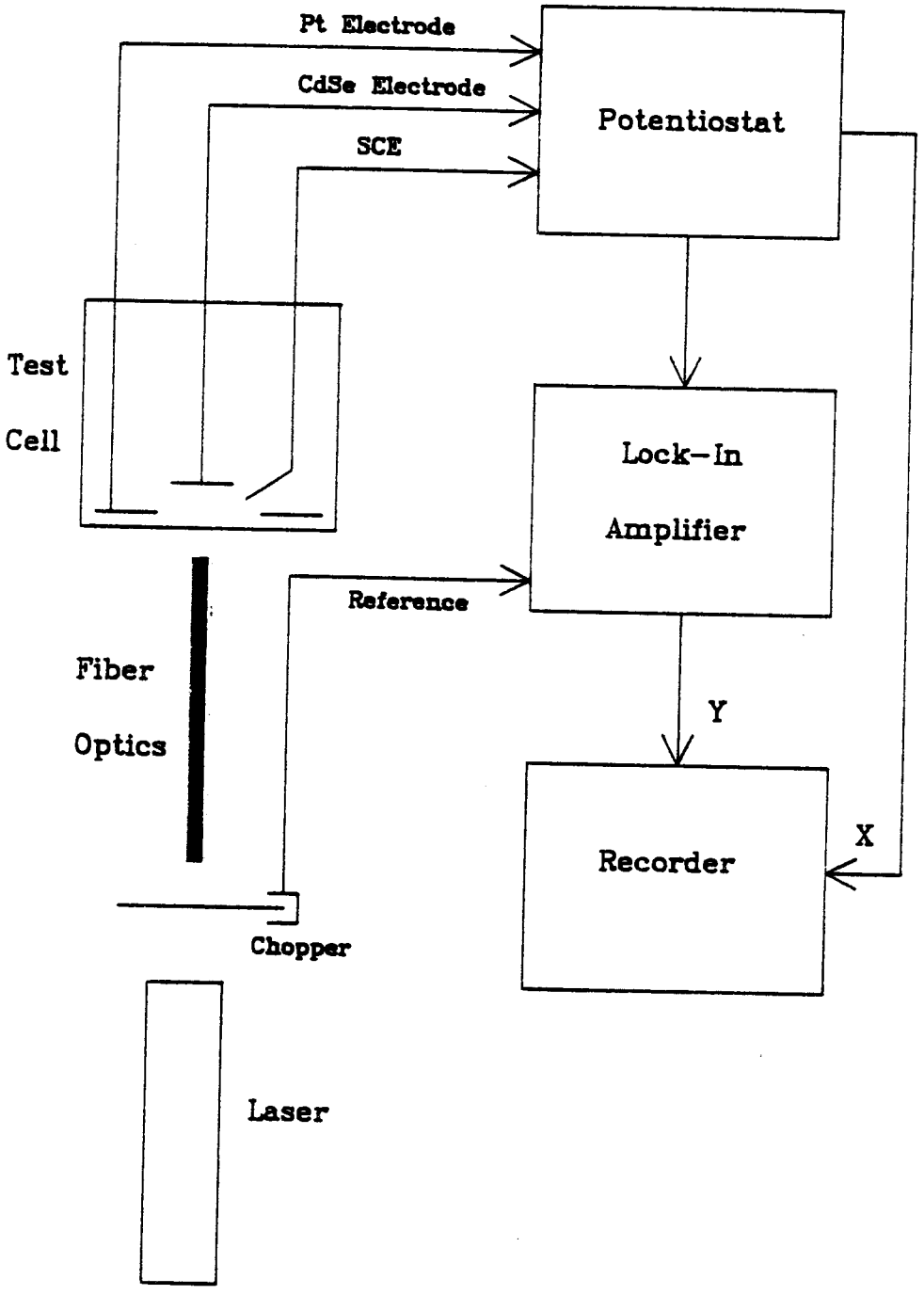
Pt Electrode
CdSe Electrode
SCE
Potentiostat
Test
Cell
Lock-In
Amplifier
Reference
Fiber
Optics
Y
X
Recorder
Chopper
Laser

Figure 4.6 The measuring apparatus to determine spectral response.

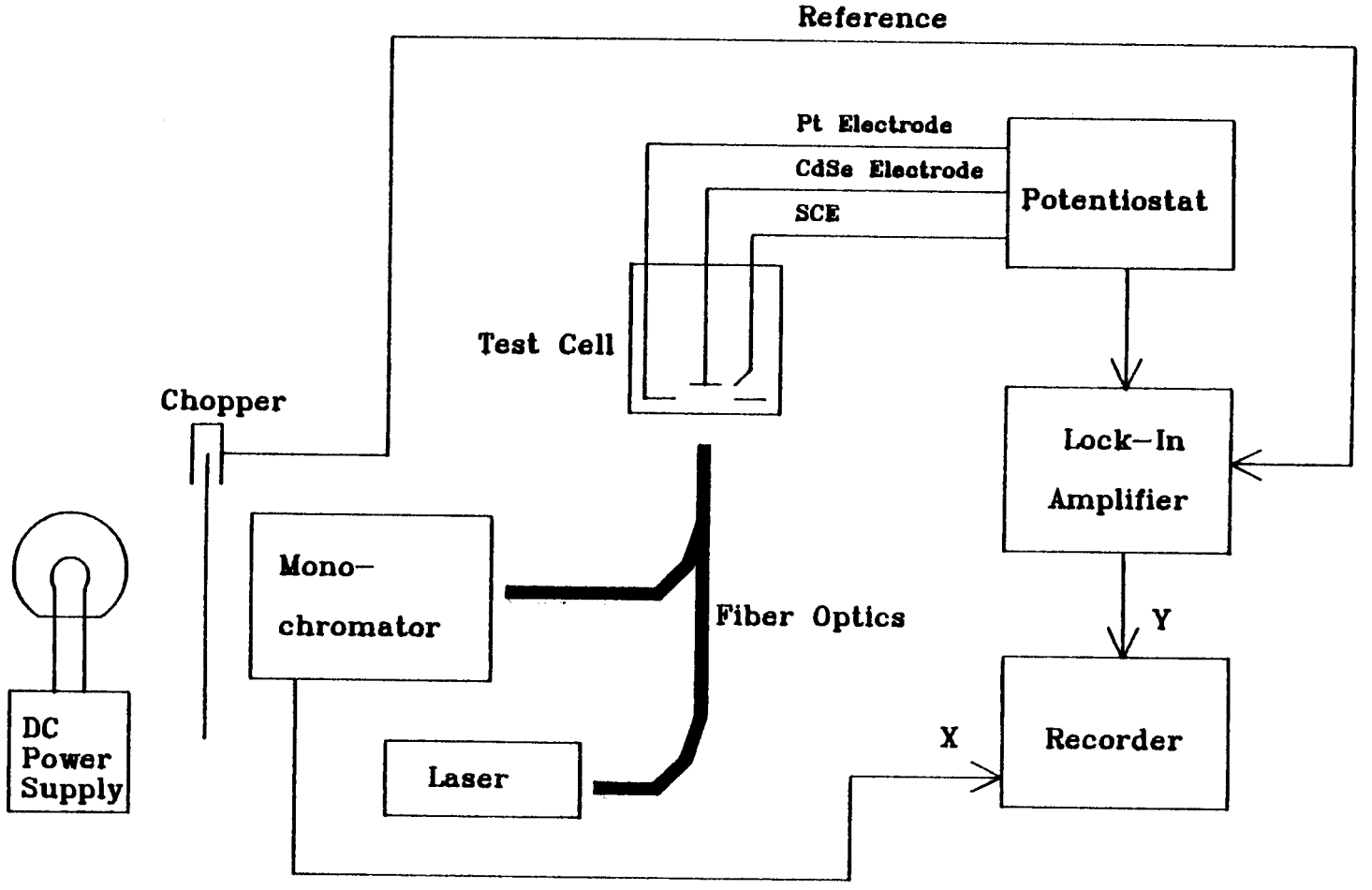
Reference
Pt Electrode
CdSe Electrode
SCE
Potentiostat
Test Cell
Chopper
Lock-In
Amplifier
Mono-
chromator
Fiber Optics
Y
DC
Power
Supply
Laser
X
Recorder

Figure 4.7 Circuit used instead of the potentiostat in Fig. 2.4 - 2.6 for the earlier experiments.

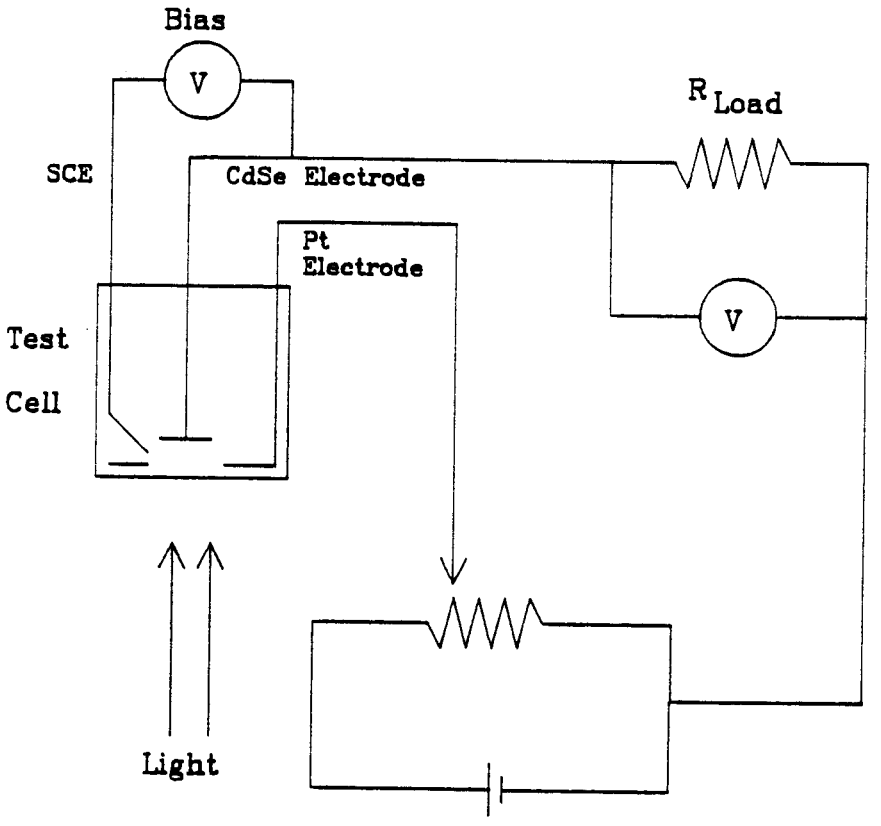
Bias
V
R Load
SCE
CdSe Electrode
Pt
Electrode
Test
Cell
V
Light

Figure 4.8 Circuit to determine resistivity.

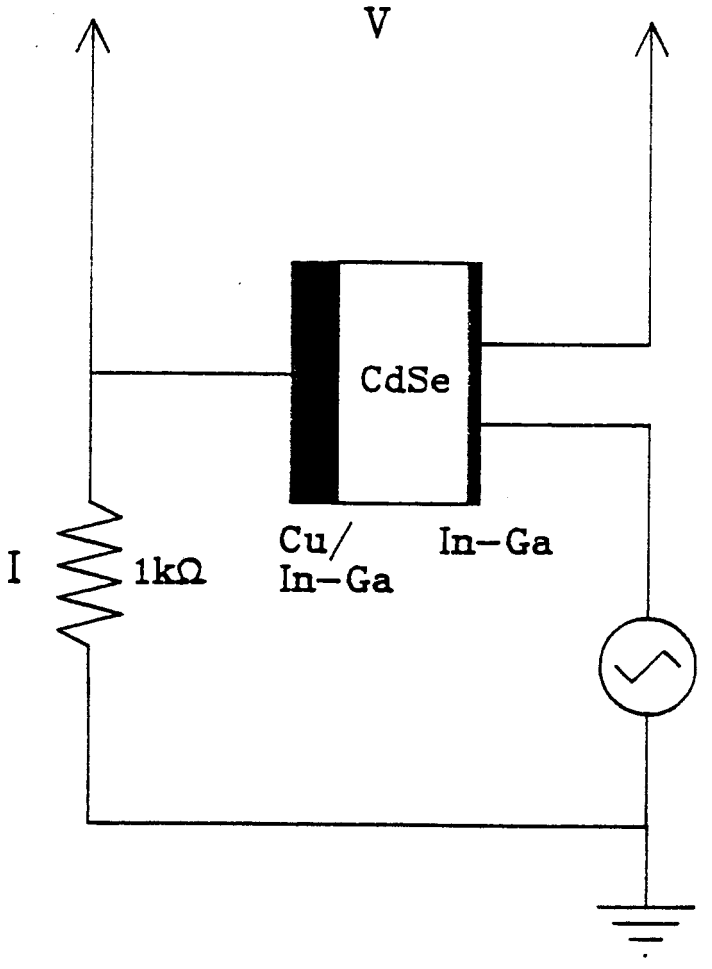
V
CdSe
I
1kΩ
Cu/
In-Ga
In-Ga

Chapter 5

Results and Discussion

5.1 Electrodeposited CdSe Electrodes

The surface morphology of electrodeposited CdSe films reveals a cauliflower structure as shown in Fig. 5.1. The micrographs in Fig. 5.1a and 5.1b depict the same area of a CdSe film before and after annealing, respectively, as indicated by the raster which was drawn onto the Ti substrate prior to the electrodeposition. The annealed film shows several microcracks and bare spots which are most likely caused by the difference in the thermal expansion coefficients of the Ti substrate and the CdSe film.

The I-V characteristics shown in Fig. 5.2 reveal a very low overall solar response for unannealed electrodes. The approximately linear decrease in current with forward bias can be associated with a high non-stoichiometry of the films observed by De Silva et al. [90] and Tomkievicz et al. [89], and a poor adhesion of the thin film to the Ti substrate. The unannealed films often peeled off the substrate if they were

left for several days, exposed to air at room temperature. After annealing, the electrode showed a 9-fold increase in the short circuit current density and an increase in the open circuit voltage from 270 to 530 mV. The "squareness" of the I-V characteristics (fill factor) also improved substantially after annealing as shown in Fig. 5.2.

The contact between the CdSe and the Ti substrate was found to be slightly non-ohmic at an applied voltage of 800 mV as shown in Fig. 5.3. For an ohmic contact between a metal and a semiconductor, it is necessary for the workfunction of the metal (ϕ_m) to be smaller than the workfunction of the semiconductor (ϕ_{sc}) [121]. Since ϕ_m(Ti) = 4.30 V [122] and ϕ_{sc}(n-CdSe) = 5.00 V [123], an ohmic contact should result. Thus, the non-ohmic behaviour must arise from a thin oxide layer on the Ti substrate.

The substantially improved solar characteristics of electrodeposited CdSe after annealing may be due to various effects, such as crystallite growth, which reduces the density of grain boundary states, increased stoichiometry and better homogeneity of the films, which reduces the number of trapping sites and recombination centers [89],[90]. The observed microcracks and bare spots in annealed films will not substantially lower the solar performance of the electrodes since the TiO_2 layer covering the substrate acts as an insulator.

The effects of etching the annealed electrodeposited CdSe

electrodes in dilute aqua regia on the surface morphology of CdSe are shown in Fig. 5.4. Etching removed loose grains and exposed larger areas of the substrate, as can be seen by comparison of the CdSe micrographs with the micrograph of the Ti substrate (Fig. 5.4e).

Comparison of the photoresponse of etched and non-etched electrodes presented in Fig. 5.5 shows both an increased photocurrent and fill factor and a slightly reduced V_{oc} due to an increased dark current for the etched electrode. The increase in current density and "squareness" of the I-V curve may be associated with the increase in active surface area of the etched electrode [108] and the removal of charge trapping sites [110],[111].

The change in quantum efficiency with forward bias, represented in Fig. 5.6, reveals the "S-shape" behaviour, which indicates a loss mechanism of charge carriers [51],[52],[55],[56]. Since the onset of the photocurrent is the same for the etched and non-etched electrodes, the reduction in V_{oc} of the etched electrodes does not arise from a shift in the flatband potential. Etching most likely reduces the shunt resistance, as indicated by an increased exposure of the substrate. A simultanous reduction in current density after etching which one may expect from removal of CdSe will be minimal if etching removes preferentially material which was poorly attached to the substrate.

The effect of light intensity on the short circuit current

in electroplated CdSe thin film electrodes (Fig. 5.7) shows a linear behaviour, as expected from eq. 2.22 in Chapter 2. The open circuit voltage reveals a logarithmic behaviour with respect to light intensity (Fig. 5.8) as predicted from the model represented in Chapter 2 by eq. (2.21), eq. (2.22), and eq. (2.23). A nonlinear behaviour would indicate a limiting hole transfer mechanism at the semiconductor/electrolyte interface.

5.2 Cold Pressed CdSe Electrodes

The surface structure of pressed CdSe powder reveals a shiny, streaked morphology which becomes flaked after annealing as shown in Fig. 5.9. The unannealed pellets had no solar response. The effect of the annealing temperature and duration on the solar parameters is summarized in Table 5.1. Annealing at 673 K in vacuum for a duration of 0.25 to 6 h showed a low overall solar response. An increase in temperature to 773 K increased the open circuit voltage considerably, although it was still low. Annealing at 973 K revealed the best solar response, but the pellets had lost a substantial amount of material and became very fragile. Annealing at 873 K for 6 h resulted in a high V_{oc}, high I_{sc}, and good fill factor.

The effect of pressure and its duration on the density of the CdSe discs is illustrated in Fig. 5.10. The duration of the

pressure had only a small effect on the density of the pressed samples. Larger pressures led to densities closer to the single crystal density of 5.74 gcm^{-3}. However, for pressures larger than 69 MPa, fractures occured either on release of the pressure or during the following heat treatment. Annealing the pellets under vacuum at 873 K for 6 h increased the density by 13 to 22 %, with the largest increase occuring for the samples pressed at a lower pressure.

The surface morphology of the annealed pressed pellets is represented in Fig. 5.11. Figure 5.11a shows the crystalline nature of the sample pressed at 11.5 MPa and the presence of large crystallites which disappear after etching the sample prior to testing its solar cell characteristics. For a sample pressed at 23 MPa (Fig. 5.11b), the surface shows an increase in flakes size and fewer crystallites are present on the surface. The crystallites disappear completely for samples pressed at 46 MPa (Fig.5.11c), and the surface has a more polycrystalline structure as evident in Fig.5.11d (five times expanded scale). Figure 5.11e shows a sample pressed at 69 MPa, which is similar in appearance to the 46 MPa sample.

The effects of pressure and its duration on the resistivity, V_{oc}, and I_{sc} are illustrated in Table 5.2. For an increased duration in pressure, the resistivity decreases, while the V_{oc} and I_{sc} fluctuate within 15 % . An increase in pressure resulted in a decreased resistivity and an increased V_{oc}, while the short circuit current was slightly reduced. The increase in

open circuit voltage and decrease in short circuit current may be associated with the increased flake size of the pellets with increased pressure. The smaller flakes yield a large surface area and a large number of surface states which may pin the Fermi level and reduce the V_{oc}.

Typical I-V characteristics under white light illumination are illustrated in Fig. 5.12(I) for samples pressed for 5 min and in Fig. 5.12(II) for samples pressed for 2 h at different pressures. Both figures show that lower pressures give rise to a higher short circuit current while the open circuit potential is lower compared to samples pressed at higher pressure. For comparison, the dark currents are shown in Fig. 5.13. Comparison with Fig. 5.12 shows that the "superposition principle" [56] is reasonably well-obeyed in these samples, i.e. the photoresponse of the cell deteriorates when the opposing dark current becomes large.

Figure 5.14 relates the I_{sc} and the V_{oc} to the density of the annealed pellets. The observed dependence of V_{oc}, I_{sc}, and the I-V characteristics on the pellet density could be ascribed to several factors which include series and shunt resistances of the cell, crystallinity of the samples, and variations in the intrinsic quantum efficiency with voltage and wavelength of the incident light.

Figure 5.15 illustrates the effect of pressure and its duration on the η_q-V curves. A general trend is a deteriorating quantum efficiency around 300 to 350 mV; as well, lower pressure

generally leads to a lower quantum efficiency. The highest density pellet (69 MPa with 2 h pressure time) shows the best efficiency at low forward bias, but shows a faster decrease with increasing forward bias, most likely due to a decrease in shunt resistance rsulting from microcracks. All curves in Fig. 5.15 exhibit the familiar "S-shape", indicating a loss mechanism related to recombination of carriers in the neutral region, the depletion region, or at the surface of the semiconductor [51],[52,[55],[56].

The spectral response of the photoanodes in Fig. 5.16 shows a well defined absorption edge of CdSe at 1.71 eV for the two samples pressed at higher pressures which indicates increased crystallinity of the pellets. The two samples that were pressed at lower pressure show a more gradual transition of the absorption edge due to a smaller grain size. This results in an increased density of defect states in the bandgap.

Comparing the general features of the voltage dependence reveals that the features of the "S-shaped" curves in the quantum efficiency dependence on forward bias (Fig.5.15) are not present in the I-V characteristics (Fig. 5.12 and Fig. 5.13). This indicates that the dominant mechanism affecting the shape of the I-V curves is the large dark current which flows opposite to the photocurrent.

5.3 Single Crystal CdSe Electrodes

Precut single crystals (batch A) and single crystals cut from an ingot (batch B) were annealed under vacuum, and in Cd and Se atmosphere. Their solar response was analyzed and compared by I-V and η_a-V characteristics, and by single and double beam photocurrent spectroscopy, using a He-Ne laser as a pumping source. The spectral response was obtained with a weak, modulated measuring beam.

Annealing of CdSe under vacuum liberates Se from the surface, leaving behind a Cd rich sample [89],[90],[124]. In polycrystalline samples, Se would escape via grain boundaries, and it is conceivable that in single crystals, the Se diffuses through the crystal surface resulting in a Se-rich surface layer over a non-stoichiometric CdSe crystal, as indicated by a red colour. This will give rise to bulk defects and a surface barrier associated with a high density of surface states. The polysulfide redox electrolyte will readily dissolve the Se layer; however the rate of dissolution is strongly reduced by the addition of 10^{-2} M Se to the electrolyte.

The presence of excess Se in the surface layer of vacuum annealed single crystals was confirmed by the SAM technique. The ratio of the Cd(376 eV) signal to the Se(1315 eV) signal was observed to be 15 % lower in the vacuum annealed samples than in

the unannealed single crystals. Unfortunately, the unannealed crystals had to be sputtered by Ar^+ ions to free the surface of excess carbon. Since Ar^+ bombardment was found to induce lattice defects in single crystal CdSe, which were attributed to excess Se [125],[126], the actual Cd/Se ratio in the unannealed crystals would be higher than observed.

The current-voltage characteristics of Cd and vacuum annealed single crystal CdSe is represented in (Fig. 5.17). While the current densities of the two different samples are similar, the dark currents (Fig. 5.17b) show very different behaviour. The dark current increases rapidly at approximately 1500 mV forward bias for vacuum annealed crystals, and between 500 and 600 mV for Cd annealed samples. The strongly reduced dark current in the vacuum annealed crystal may be accounted for by the presence of a surface barrier to electron flow arising from the Se-rich surface which breaks down a high forward bias, in agreement with a model proposed by Frese for anodized single crystal surfaces [91],[119],[120].

The decrease in current density of the Cd annealed crystals in Fig. 5.17a is primarily determined by the dark current, while the current density of the vacuum annealed samples seems to be independent of the dark current. For both samples, the decrease in current density for low forward bias indicates a blocking barrier for holes at the surface [56]. El Guibaly and Colbow [56] associated this behaviour with surface states acting as hole trapping sites which become ionized with illumination, thus

reducing the amount of bandbending. As seen in Fig. 5.17, the Cd annealed sample shows a high cathodic current which essentially equals the hole flow to the electrode surface at ~0.5 V. In contrast, the vacuum annealed electrode does not reveal this large cathodic current, presumably due to the Se layer at the surface.

The behaviour of the quantum efficiency at 6328 Å with forward applied voltage is illustrated in Fig. 5.18. The current direction of the vacuum annealed single crystal (Fig. 5.18b) reverses for voltages larger than the open circuit voltage. A possible explanation is that under strong light illumination the Se layer becomes photoconductive and allows a cathodic current to flow between the CdSe and the electrolyte solution.

The Cd annealed sample in Fig. 5.19 shows the same "normal" spectral response as an untreated single crystal [127] (not shown), but with a six-fold increase in quantum efficiency (see Table 5.3), with and without laser pumping. Vacuum annealing of CdSe crystals did not improve the overall solar response. In fact, it showed a rather unusual behaviour, which became more pronounced with laser pumping. A double peak feature in the photocurrent spectrum at 1.66 eV and 1.71 eV near the bandedge of CdSe, and a lower, nearly constant response for photon energies larger than 1.8 eV, was observed. With laser pumping, the efficiencies near the bandgap increase substantially, while the efficiencies decrease and reach a low value for high energy photons.

Haak et al. [125],[126] observed the presence of intrinsic inter-bandgap states approximately 0.2 eV below the conduction bandedge in CdSe, with a higher density of states in polycrystalline CdSe than in single crystal CdSe. However, polishing and Ar^+ ion bombardment of single crystals, which causes defect states, enhanced the density of these states. The authors attributed the origin of these states to excess Se.

Heller et al. [110] observed a similar, but much less pronounced behaviour of the spectral response of single crystal CdSe with peaks at 1.64 and 1.69 eV as shown in Fig. 5.19. They ascribed these peaks to states within the bandgap arising from imperfections near the semiconductor surface and acting as traps and recombination centers. This would lead to changes in the photoresponse, particularly for light absorbed near the semiconductor surface. The observed peaks possibly arise from photon absorption and electron-hole generation involving inter-bandgap states. Photons of energy greater than 1.8 eV are strongly absorbed near the surface, resulting in a reduced quantum efficiency due to recombination via the large density of surface states. Laser pumping would result in the filling of the traps near the CdSe/Se interface and thus yield an increased quantum efficiency.

Amorphous Se has a bandgap of 2.05 eV [128], just above the laser energy of 1.96 eV. Amorphous Se at the surface, with a large concentration of Cd, will likely show strong absorption at the laser energy. If electrons are trapped in the Se surface

layer while the light generated holes are captured by the reduced species of the redox electrolyte, a larger bandbending will be produced in the CdSe, and thus a larger depletion width will result. The increased number of electrons near the CdSe/Se interface will decrease the quantum efficiency for electron-hole pairs generated by high energy photons by filling traps and recombination centers. The increased depletion width will result in an increased quantum efficiency for holes generated by near bandgap photons since they create electron-hole pairs deeper in the crystal. This would also explain the increased efficiency of the 1.66 eV transition with increasing light intensity, as shown in Fig. 5.20. At a laser intensity of 7 Wm^{-2}, the photocurrent is saturated, which indicates a slow transfer velocity of holes to the electrolyte [53],[56], resulting in photocorrosion.

Figure 5.21 shows the spectral response of anodized CdSe after Cd and after vacuum annealing. The grown Se layer was found to be ~0.27 μm thick for both samples, as calculated from integrated photocurrent measurements [91],[119],[120]. While the Cd annealed sample reveals the same behaviour with and without laser pumping (Fig. 5.21a), the vacuum annealed, anodized crystal (Fig. 5.21b,c) shows a response similar to the untreated, vacuum annealed sample. The overall increase in quantum efficiency of anodized samples is most likely caused by an improved surface condition due to photoetching. Similar results were obtained by Frese [121], showing an increased

quantum efficiency near the bandedge for anodized CdSe electrodes. For Se layer thicknesses of 0.24 and 0.36 μm, the photoresponse substantially decreased for wavelengths less than 1.96 eV, and was associated with photon absorption in the Se layer. The spectral response in Fig.5.21 shows a smaller decrease in quantum efficiency for the high energy photons, indicating that the Se layer may in fact be thinner than calculated, or possibly porous [129].

Leaving the anodized samples for 24 h in redox electrolyte under short circuit conditions improved the quantum efficiency, which indicates that the Se layer dissolves, leaving behind a photoetched CdSe surface. The double peak feature of the vacuum annealed sample (Fig. 5.21b) disappears upon anodizing and only the 1.71 eV peak remains. Upon laser pumping (Fig. 5.21c), the quantum efficiency peak again shifts to 1.66 eV. This indicates that the 1.66 eV transition is due to a deep interband state which is essentially not affected by photoetching.

Figure 5.22 represents various heat treatments for batch B single crystal CdSe. The spectral response of the quantum efficiency is considerably improved for the Cd annealed sample compared to the untreated single crystal (Fig. 5.22a). Both show a "normal" spectral response and reveal identical results with and without laser pumping. The untreated crystal shows some band tailing which seems to disappear upon Cd annealing. The vacuum annealed single crystal (Fig. 5.22b) shows only one peak at 1.71 eV with very low quantum efficiency. Photons with

energy greater than 1.8 eV do not show any measurable photoresponse, indicating a strong absorption in the Se surface layer of the crystal and/or a large density of hole trapping sites near and at the surface. Upon laser pumping, only one peak is observed which shows strong band-tailing and a large 50-fold increased quantum efficiency at 1.66 eV.

Figure 5.22c represents the spectral response of Se annealed CdSe crystals. While the quantum efficiency is extremely small, the crystals show a "normal" behaviour with a bandgap of 1.74 eV. With laser pumping, the bandedge shifts towards lower energies, giving rise to a small peak at 1.74 eV. Annealing in Se atmosphere may compensate the semiconductor since Se would act as an electron acceptor, resulting in a low effective donor density and a large number of carrier traps.

Table 5.3 summarizes and compares the quantum efficiencies for highly energetic photons (2.0 eV) and the observed peak efficiency at 1.71 eV (without laser pumping) and 1.66 eV (with laser pumping) for the untreated and annealed CdSe single crystals.

5.4 Comparison of Electrodeposited, Cold Pressed and Single Crystal CdSe Electrodes

The I-V characteristics of electroplated, pressed, and single crystal CdSe photoanodes is compared in Fig.5.23. While

the highest power conversion efficiency of 4.2±0.2 % is obtained for the pressed pellet electrode, the electroplated electrode has a performance similar to that of the single crystals, with an efficiency of 2.4±0.2 %.

The surface morphologies of the electroplated and pressed CdSe after heat treatment are compared in Fig. 5.24. The pressed pellet surface shows a uniform polycrystalline appearance, and the electroplated sample reveals a cauliflower-like structure with microcracks, some of which extend to the Ti substrate. Thus, the high short circuit current of the pressed pellet in Fig. 5.23 may result from the large active surface area, and the reduced short circuit current in electroplated CdSe may be due to its inhomogeneous morphology. The microcracks give rise to a low shunt resistance and thus a reduced V_{oc}.

Electroplated thin films are generally less pure than pressed electrodes, resulting in a narrower depletion width, so that more carriers are generated in the bulk where recombination is more probable. The emission spectrographic analysis of both the single crystals and the powder on pages 88 and 86, respectively, reveals that the poor performance of the single crystals cannot be associated with a high impurity concentration. However, the reduced I_{sc} and fill factor of the single crystals may be explained by the presence of a large number of defect states causing recombination and trapping of charge carriers.

The quantum efficiency at 6328 Å as a function of forward

bias for the polycrystalline samples and the Cd annealed single crystal is represented in Fig. 5.25. The "S-shape" in the quantum efficiency is apparent for all three electrodes. Although the single crystal shows a lower quantum efficiency than the pressed pellet, the shape of the single crystal curve indicates a lower series resistance. Due to series resistance of the photocell, in forward bias not all of the applied voltage will be across the space charge region. This affects the observed voltage dependance of the quantum efficiency and causes saturation of the dark current. Thus, the gradual tailing in η_q of the pressed pellet could be ascribed to a higher series resistance. The relatively flat response in η_q with small forward bias for both the single crystal and the electroplated CdSe is not observed in the I-V characteristics. This indicates that the dark current determines the shape of the I-V curves.

The quantum efficiency at low forward bias in Fig. 5.25 was fitted to the Gärtner/Butler model [22],[23], represented on page 24. The best fit was obtained with $\alpha L_p << 1$. The donor densities calculated from the fitted W_o with $\alpha = 0.68 \times 10^5$ cm^{-1} for a photon energy of 6328 Å [61] are:

single crystal electrode 1.3×10^{17} cm^{-3}

pressed pellet electrode 3.1×10^{16} cm^{-3}

electroplated electrode 1.6×10^{18} cm^{-3}.

These values were then used to regenerate the quantum efficiencies via eq. 2.19 in Chapter 2 and the results are

indicated in Fig. 5.25 by the circles. The calculated and experimental efficiencies are in agreement only for low forward bias. The Gärtner/Butler model only assumes recombination of carriers in the bulk of the semiconductor. For a larger forward cell bias, the charge recombination in the depletion region and at the surface becomes more probable; in this case the model no longer holds.

Figure 5.26 represents the spectral response of the quantum efficiency for the Cd annealed single crystal, pressed pellet, and electroplated CdSe photoanodes at short circuit. While the photoresponse of single crystal CdSe is relatively small for sub-bandgap photon energies, the electroplated and pressed pellet electrodes show appreciable band-tailing. This indicates defect states within the semiconductor bandgap, which most likely result from grain boundaries and/or lattice defects. The low performance of the electroplated electrode is determined largely by its morphology and by a low shunt resistance. Assuming the validity of the Gärtner/Butler model at short circuit, Fig. 5.26 suggests that the wavelength response of the absorption coefficient is different for the three different electrodes.

The plot of $(\eta_q h\nu)^2$ in Fig. 5.27 shows a bandgap of 1.73±0.01 eV for the single crystal CdSe, while the polycrystalline samples extrapolate to an absorption edge of 1.71±0.01 eV. The knee in the curves of the polycrystalline samples may result from defect states within the bandgap.

5.5 Ion Surface Treatments

Dipping CdSe electrodes into $ZnCl_2$ or $HgCl_2$ solution can cause considerable changes in the solar performance. Zinc or Hg^{2+} ions chemisorbed at grain boundaries and surface states will result in a Zn-Se or Hg-Se bond, respectively. This will relocate surface states and may split them into bonding and anti-bonding states. Zinc selenide is a wide bandgap semiconductor (E_g=2.6 eV) which will reduce hole trapping and/or recombination at grain boundaries, while HgSe with a bandgap of 0.26 eV will enhance minority carrier loss.

The various Zn^{2+} ion treatments of pressure sintered CdSe electrodes are summarized in Table 5.4. While dipping the electrodes in cold, as well as boiling $ZnCl_2$ solution shows a pronounced increase in V_{oc}, the short circuit current density of electrodes dipped in boiling $ZnCl_2$ solution shows a dramatic decrease, even though it is not affected in cold-dipped electrodes. This decrease in J_{sc} could be caused by fracturing the pellets, and in fact, some electrodes split into half after 20 min immersion into the boiling solution. The effect of Zn^{2+} ion treatment is most significant for electrodes with a low solar performance, which was also reported by Tomkievicz et al. [89]. Therefore a true comparison between different electrodes is not possible.

The I-V characteristics of the cold dipped, pressure sintered elctrode, represented in Fig. 5.28, show a pronounced increase in V_{oc}, resulting largely from the decrease in the dark current. The treated and untreated electrodes do not obey the "superposition principle", i.e. the superposition of photocurrent and dark current, which would indicate the presence of a large density of surface states [56]. The increase in V_{oc} with dipped electrodes may arise from a shift in the surface states close to the conduction bandedge, which prevents shunting of the depletion region.

The effect of $ZnCl_2$ dipping on the quantum efficiency-voltage characteristics is represented in Fig. 5.29. The dipped electrode shows a shift in the onset of the photocurrent to a higher voltage, which may be associated with a shift in the flatband potential. This would also explain the reduction in dark current density and thus, the increase in open circuit voltage. The shifted "S-shape" in the η_q-V curves predicts an increased charge transfer across the interface [52],[56], possibly due to the increased bandbending.

A comparison of the I-V characteristics of pressed pellet electrodes dipped in $HgCl_2$ solution with $ZnCl_2$ dipped and untreated electrodes is represented in Fig. 5.30. Mercuric ion treatment results in a reduced open circuit voltage as well as a reduced fill factor and power conversion efficiency, due to an increased dark current. The weakly adsorbed Hg^{2+} ions at the electrode surface slightly shift the surface states such that an

increased shunting causes majority carriers to fill the surface states as indicated by the increased dark current. However, strongly adsorbed Zn^{2+} ions result in a large shift of surface states, such that the tunneling of majority carriers is blocked.

Scanning Auger electron microscopy provided evidence that Zn^{2+} and Hg^{2+} ions are chemisorbed at the surface and at grain boundaries of polycrystalline CdSe. The spectra showed no evidence of the ion adsorption of dipped and subsequently etched single crystal CdSe; dipping with subsequent etching revealed the presence of Zn and Hg atoms in the CdSe pressed pellets.

The effect of Zn^{2+} treatment on electroplated electrodes is more pronounced than in pressure sintered electrodes, as shown in Fig. 5.31. In addition to an increased V_{oc} caused by a decreased dark current, the current density shows a substantial increase. Since the surface of the electroplated thin films is porous with microcracks and bare spots and thus less homogeneous than the pressed pellets, the ion solution will passivate grain boundaries very effectively, more so than in pressed electrodes. The resulting reduction in the density of recombination centers would account for the substantial increase in the photocurrent.

Table 5.1 The effect of annealing temperature and its duration on the solar performance of CdSe pressed pellet elctrodes

The pellets were pressed at 46 MPa.

(Illumination intensity 630 Wm^{-2})

V_{oc} = open circuit voltage in mV

J_{sc} = short circuit current density in $mAcm^{-2}$

ff = fill factor

Temp [°C] \ Time [h]	1/4			1/2			1			2			6		
	V_{oc}	J_{sc}	ff	V_{oc}	J_{sc}	ff	V_{oc}	J_{sc}	ff	V_{oc}	J_{sc}	ff	V_{oc}	J_{sc}	ff
400				160	0.01	0.39	150	0.03	0.25	105	0.04	0.26	105	0.14	0.27
500	460	0.02	0.25	360	0.10	0.36	370	0.08	0.31	470	2.2	0.32	460	0.70	0.31
600	540	3.3	0.30	515	4.7	0.31				550	3.3	0.50	540	3.8	0.56
650	520	0.9	0.45				545	3.0	0.46						
700				610	4.0	0.57									

Table 5.2 The effect of pressure and its duration on the solar parameters of pressure sintered electrodes

(Illumination intensity 1000 Wm^{-2})

V_{oc} = open circuit voltage

J_{sc} = short circuit current

Pressure [MPa]	Time [min]	Resistivity [Ω cm]	V_{oc} [mV]	J_{sc} [$mAcm^{-2}$]
11.5	5	13.9 k	367	5.50
11.5	30	8.3 k	362	5.10
11.5	60	1.6 k	378	6.12
11.5	120	3.4 k	353	5.30
11.5	180	1.5 k	373	5.46
23	5	456	409	4.85
23	30	125	575	4.47
23	120	751	412	3.76
23	180	750	573	5.37
46	5	71	597	4.15
46	30	175	624	4.00
46	60	194	549	3.43
46	120	740	590	4.00
69	5	348	561	4.21
69	120	569	516	3.84

Table 5.3 The quantum efficiencies at 2.00 eV and the peak response (~1.7 eV) with and without laser pumping for CdSe single crystals with various treatments

CRYSTAL BATCH	TREATMENT	LASER OFF		LASER ON	
		QUANTUM EFFICIENCY (%) 2.00eV	1.71eV	QUANTUM EFFICIENCY (%) 2.00eV	1.66eV
A	etched	4		4	
	Cd-annealed				
	etched	24		24	
	anodized	30		30	
	24 h later	37		37	
	Vac-annealed				
	etched	3	3	0.1	17
	anodized	5	6	0.1	21
	24 h later	12	11	0.1	94
B	etched	16		16	
	Cd-annealed	50		50	
	Vac-annealed	0	1	0	47
	Se-annealed	0.1		0.1	

Table 5.4 The effect of Zn^{2+} ion surface treatments on the solar performance of CdSe pressed pellet electrodes

ΔV_{oc} = change in open circuit voltage

ΔJ_{sc} = change in short circuit current

Δ ff = change in fill factor

$\Delta \eta$ = change in power conversion efficiency

Zn^{2+} ion Treatment	ΔV_{oc} [%]	ΔJ_{sc} [%]	Δ ff [%]	$\Delta \eta$ [%]
5 min 373 K	3	2	−6	0
10 min 373 K	3	−14	0	−8
20 min 373 K	6	−41	29	17
5 min 295 K	10	0	4	4
30 min 295 K	16	0	7	20

Figure 5.1 The surface morphology of electrodeposited CdSe thin films

(a) as deposited

(b) annealed in vacuum at 873 K for 20 min

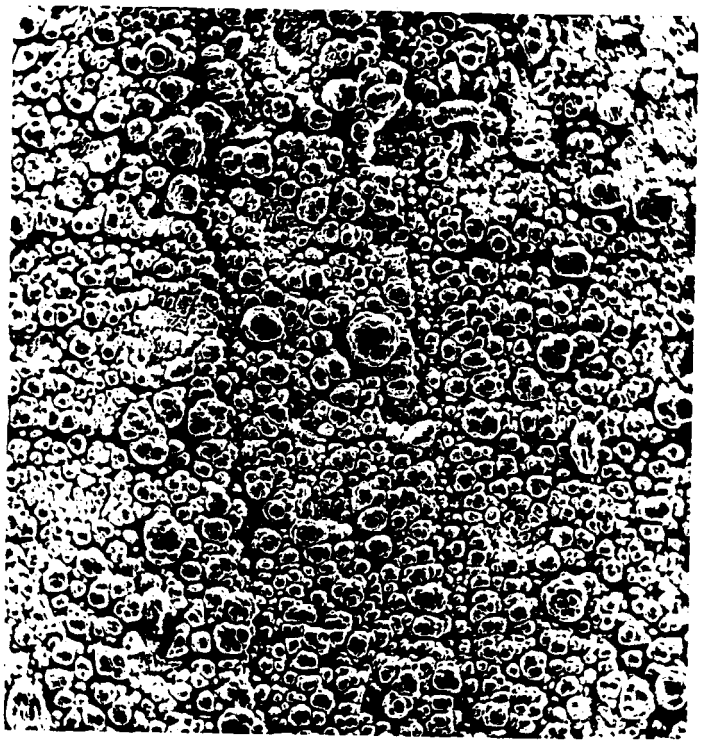

a

5μm

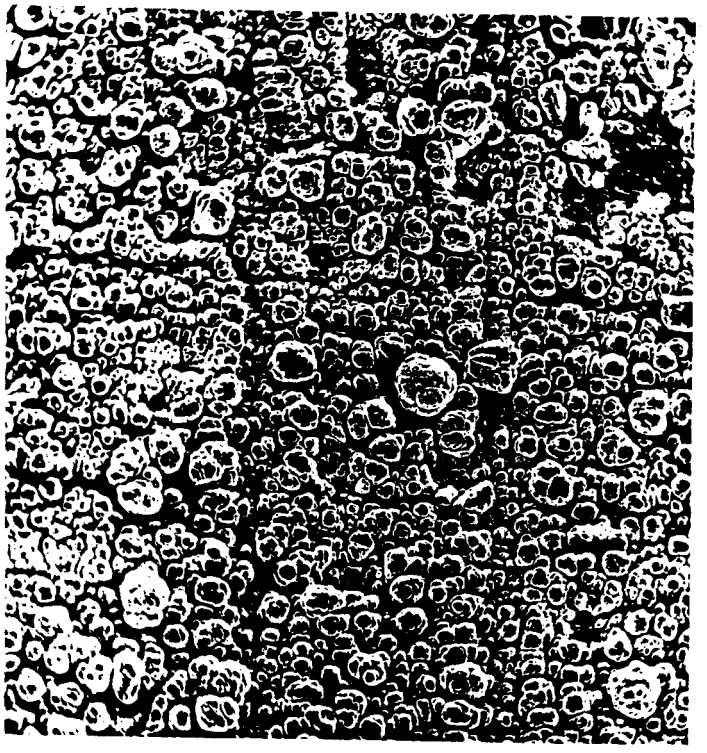

b

5μm

(200 x)

Figure 5.2 Current-voltage characteristics of annealed (——) and untreated (- - -) electroplated CdSe photo-anodes

(a) in the dark

(b) with white light illumination of 1000 Wm^{-2}) intensity

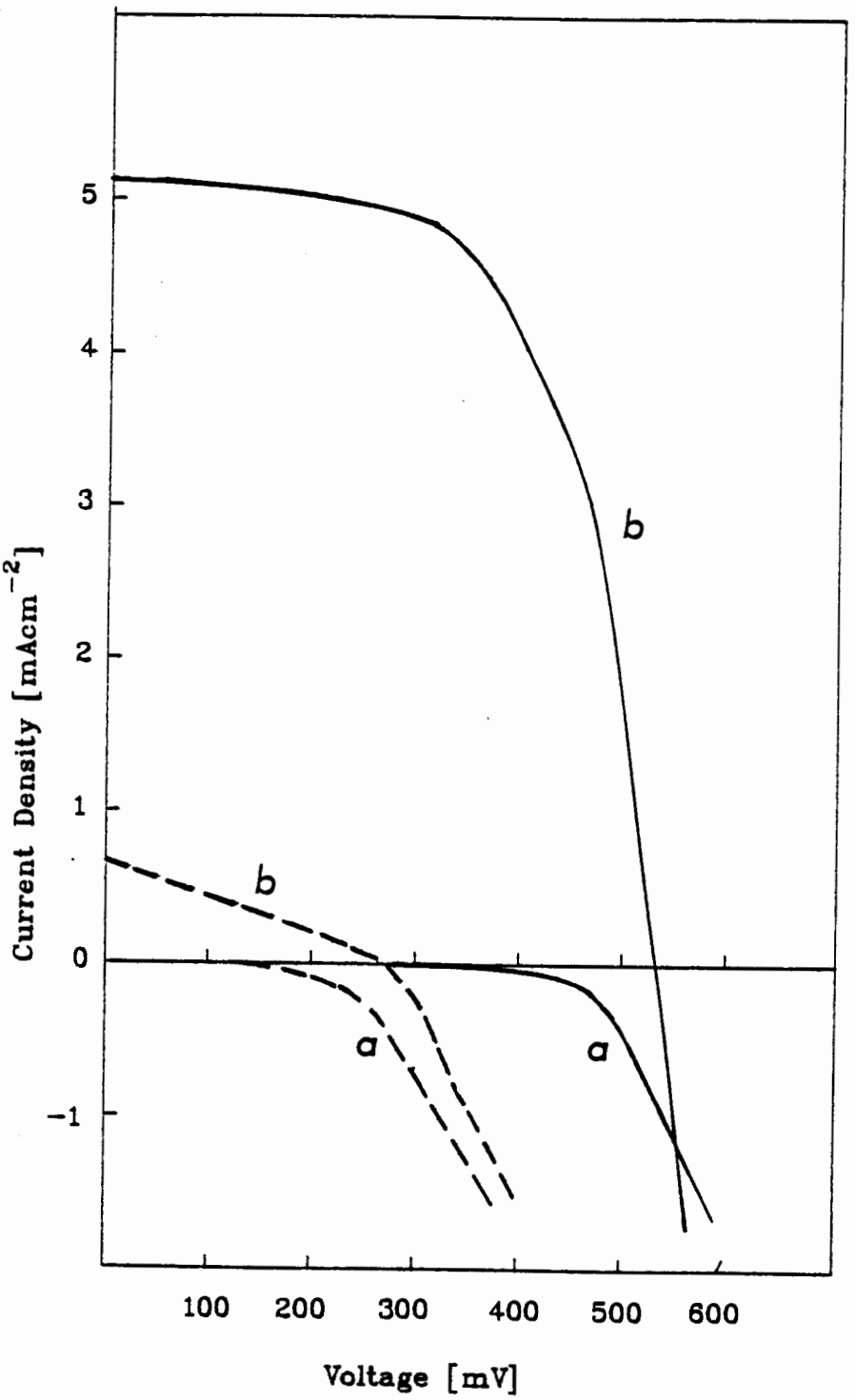
Current Density [mAcm^{-2}]
5
4
3
2
1
0
−1
b
b
a
a
100
200
300
400
500
600
Voltage [mV]

Figure 5.3 Current-voltage characteristics of the electroplated CdSe/Ti substrate and CdSe/In-Ga solid state contacts

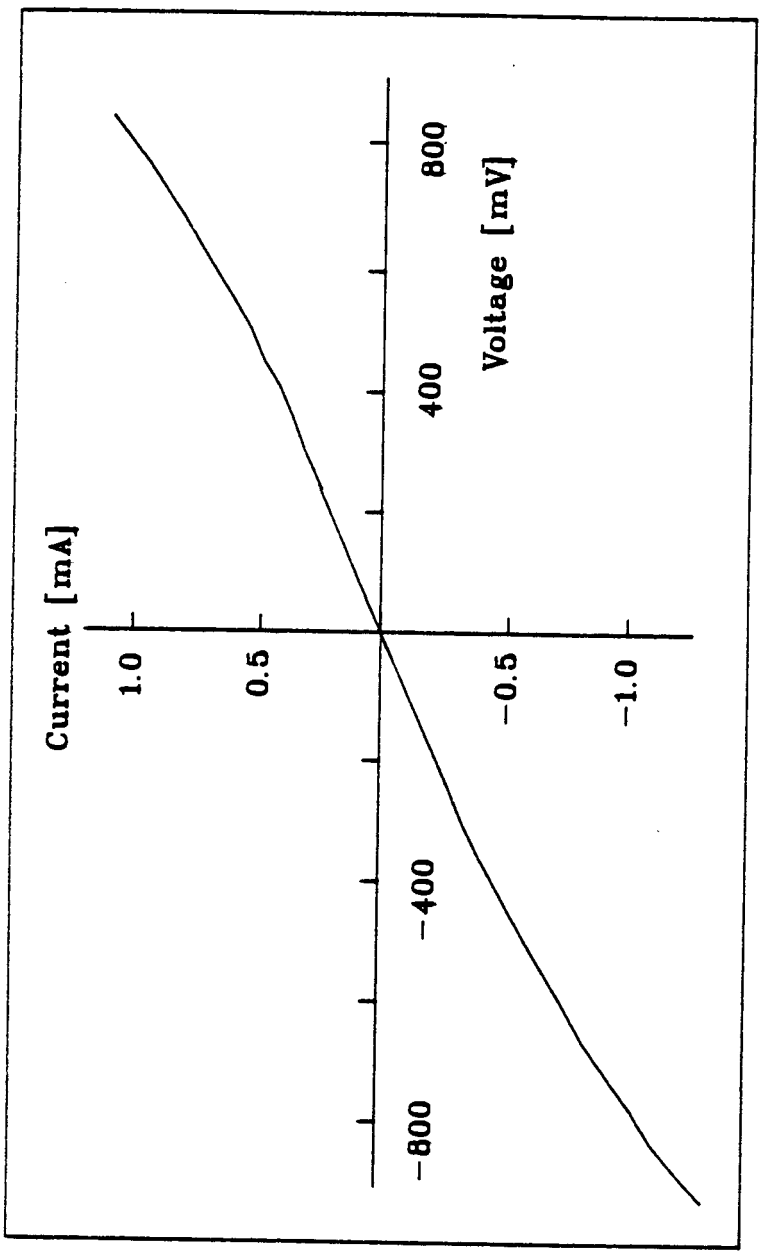
Current [mA]
1.0
0.5
-0.5
-1.0
800
400
-400
-800
Voltage [mV]

Figure 5.4 Surface morphology of electroplated CdSe thin films

(a), (b) before etching

(c), (d) etched for 1 min in dilute aqua regia

(e) Ti substrate

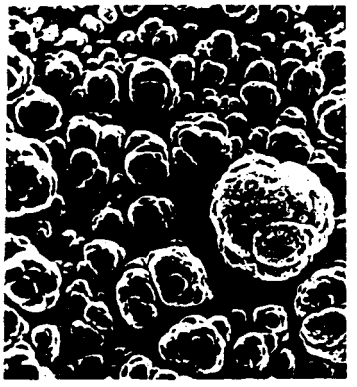

a

b

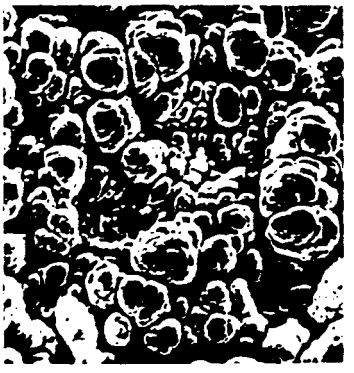

c

d

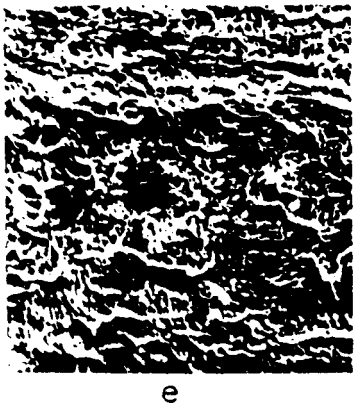

e

10 µm

(1000x)

Figure 5.5 Current-voltage characteristics of etched (——) and unetched (- - -) electroplated CdSe electrodes
(a) in the dark
(b) with white light illumination of 1000 Wm^{-2}) intensity.

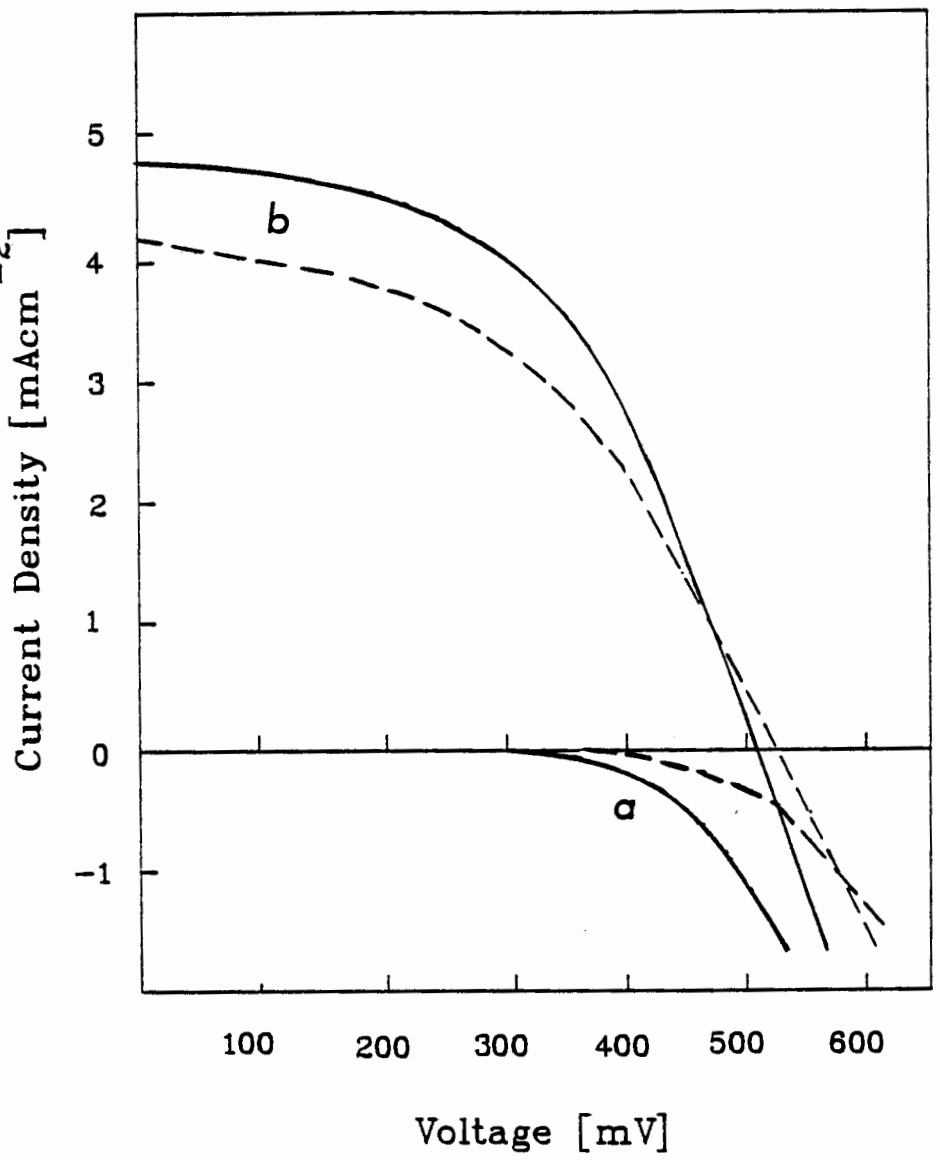
Current Density [mAcm^{-2}]
5
4
3
2
1
0
−1
b
a
100
200
300
400
500
600
Voltage [mV]

Figure 5.6 Quantum efficiency-voltage characteristics of the electrodes shown in Fig. 5.5

(a) after etching

(b) before etching

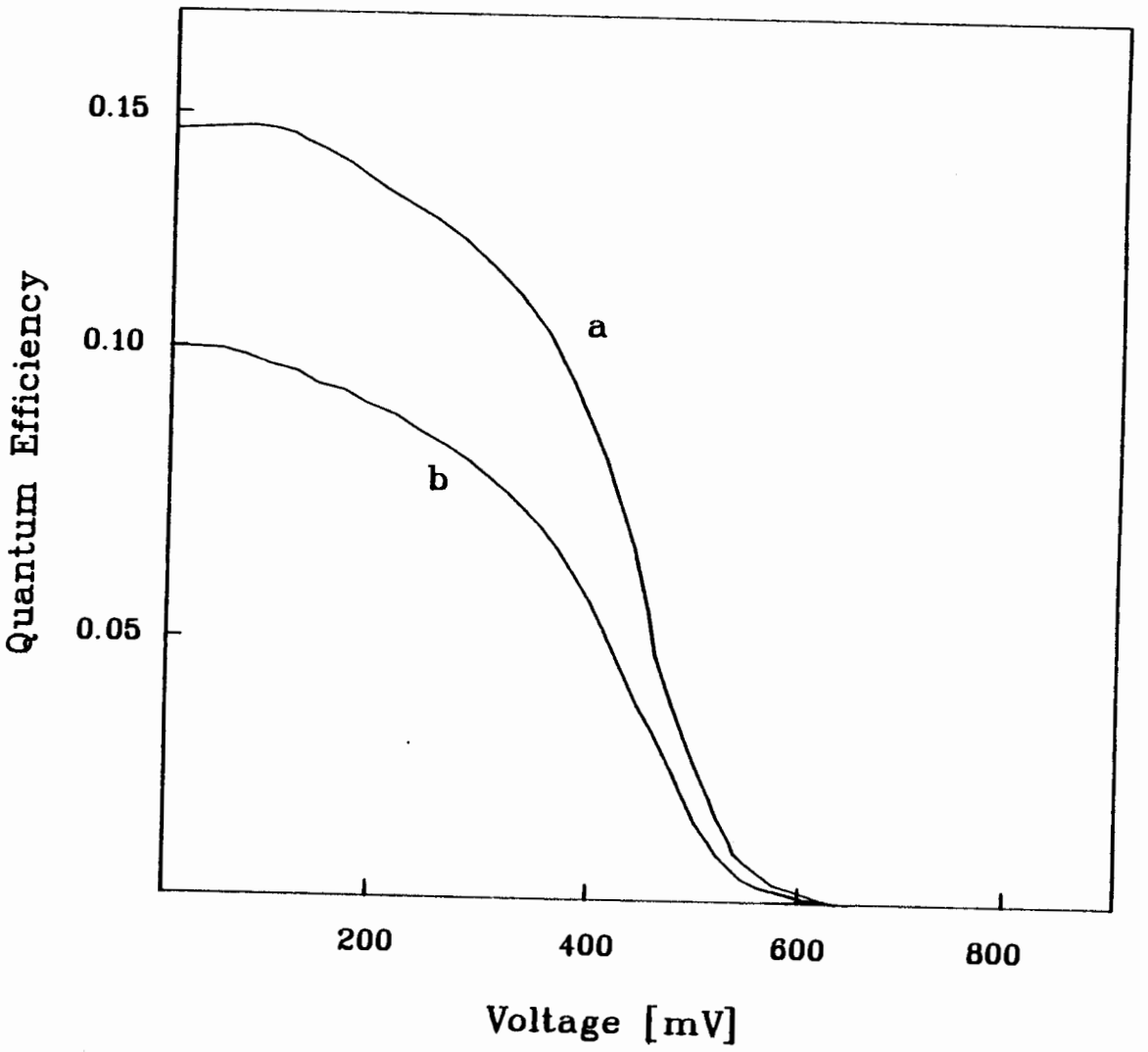
Quantum Efficiency
0.15
0.10
0.05
a
b
200
400
600
800
Voltage [mV]

Figure 5.7 The effect of light intensity on the short circuit current of electroplated CdSe elctrodes

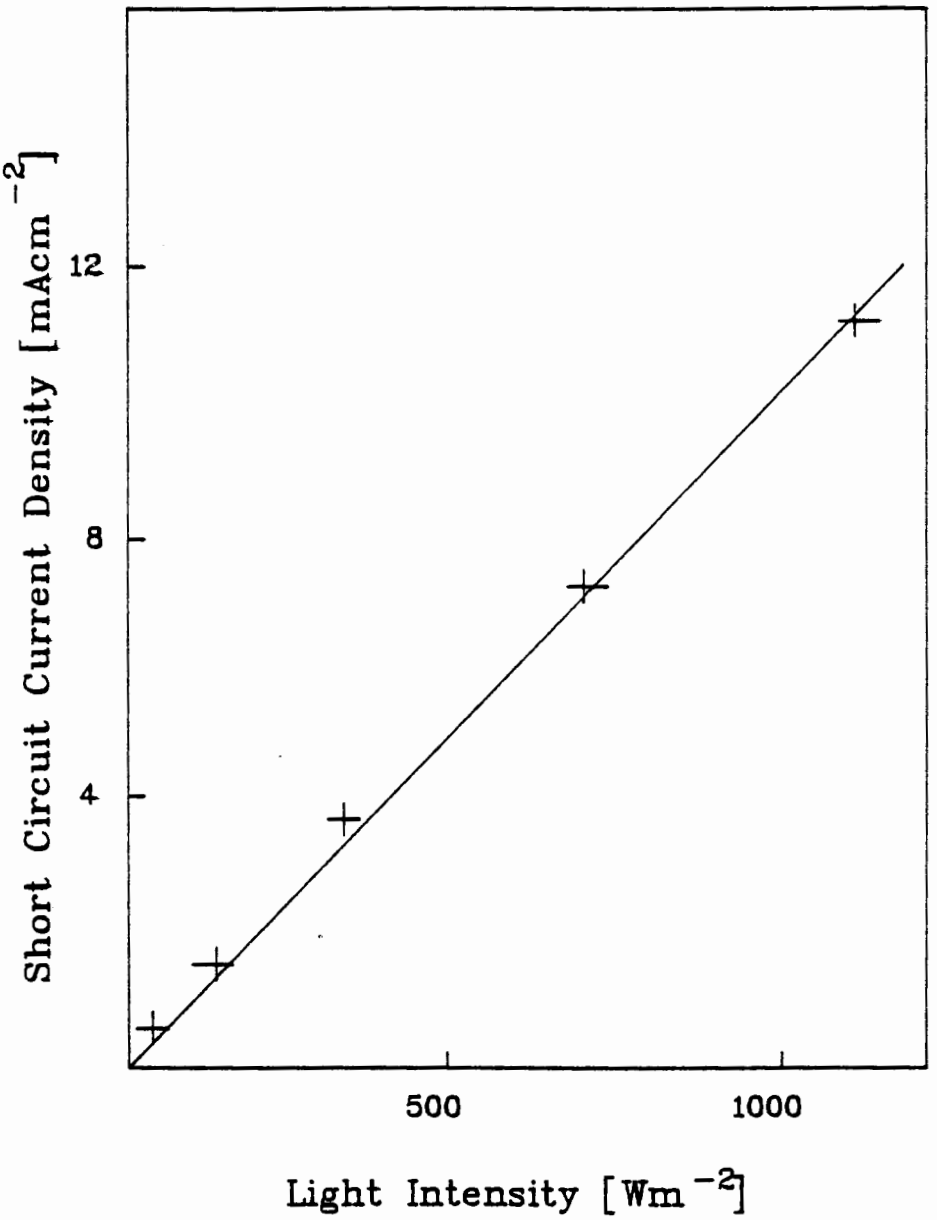
Short Circuit Current Density [mAcm^{-2}]
12
8
4
500
1000
Light Intensity [Wm^{-2}]

Figure 5.8 The effect of light intensity on the open circuit voltage of electroplated CdSe electrodes

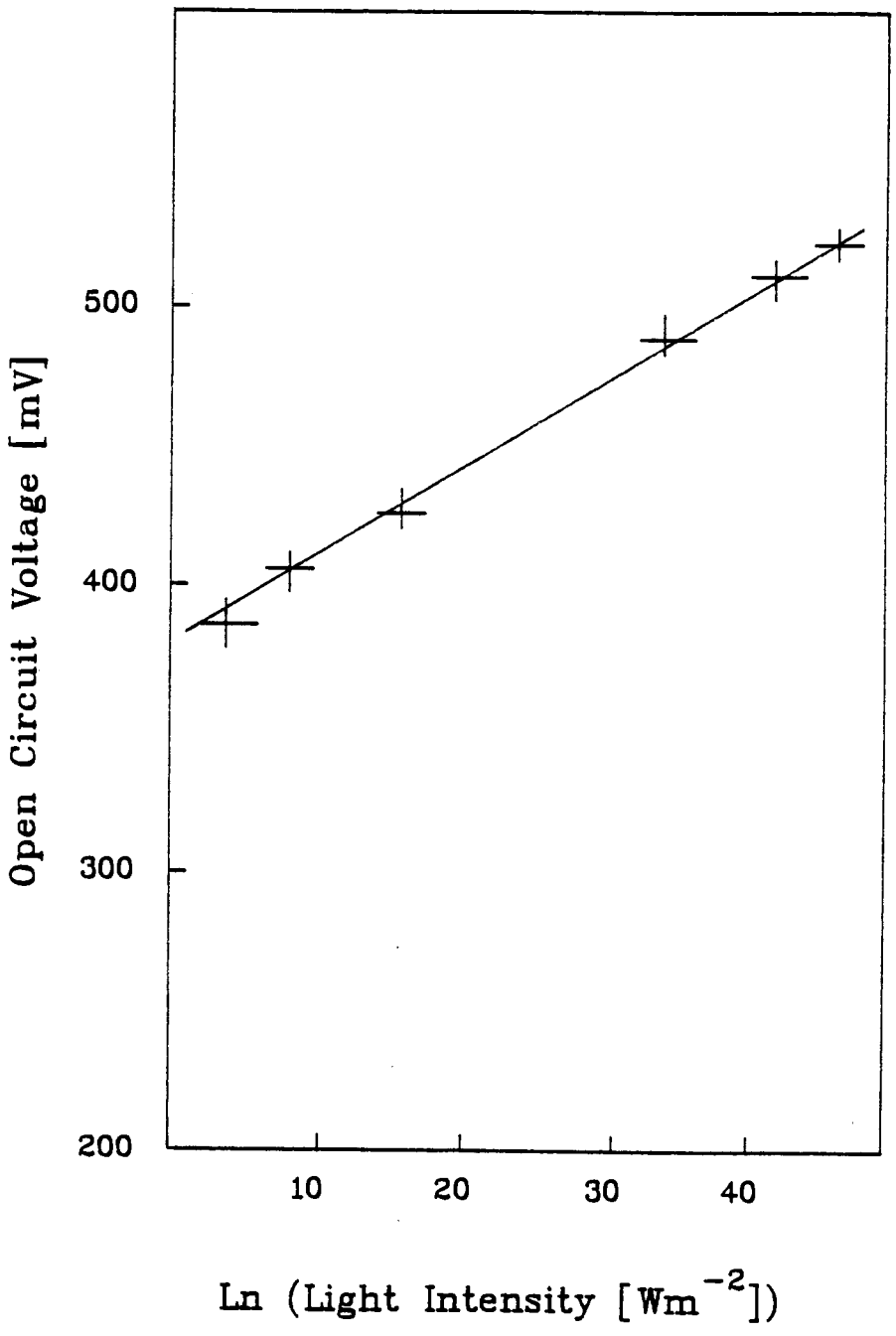
Open Circuit Voltage [mV]
500
400
300
200
10
20
30
40
Ln (Light Intensity [Wm^{-2}])

Figure 5.9 Surface morphology of unannealed (a) and annealed (b) pressure sintered CdSe electrodes

a

b

5μm
(3000 x)

Figure 5.10 Effects of pressure and its duration on the density of pressed CdSe.

(———) Density before annealing

(- - -) Density after annealing at 873 K for 6 h

The samples were pressed at pressures of:

(a) 11.5 Mpa

(b) 23 Mpa

(c) 46 Mpa

(d) 69 Mpa

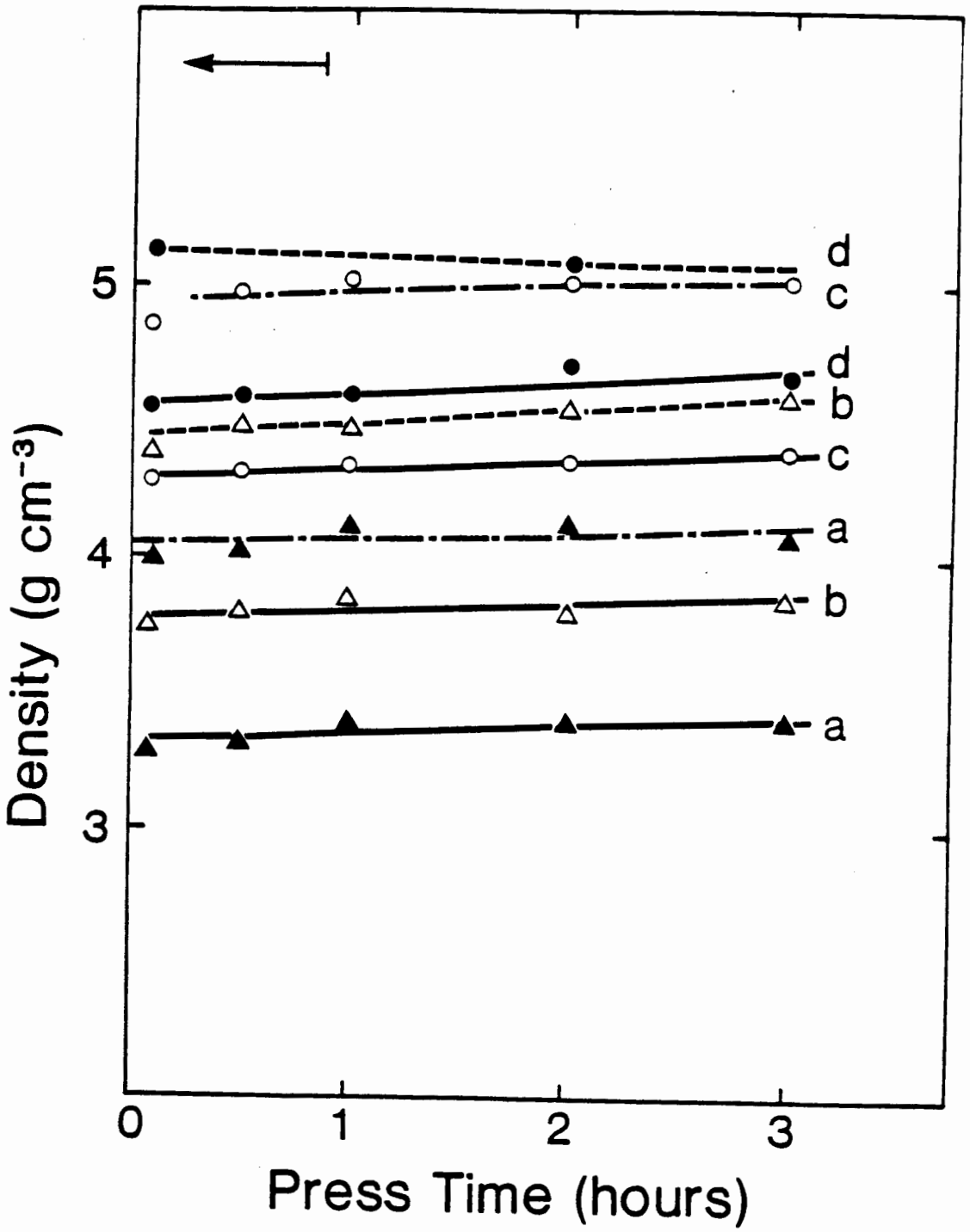
Density (g cm^{-3})
5
4
3
0
1
2
3
Press Time (hours)
d
c
d
b
c
a
b
a

Figure 5.11 Electron micrographs showing the surface morphology of annealed CdSe samples magnified 1000 times, except for (d) (5000 times)

The pressures applied and the duration were:

(a) 11.5 MPa for 2 h

(b) 23 MPa for 2 h

(c) 46 MPa for 2 h

(d) 46 MPa for 2 h

(e) 69 MPa for 5 min

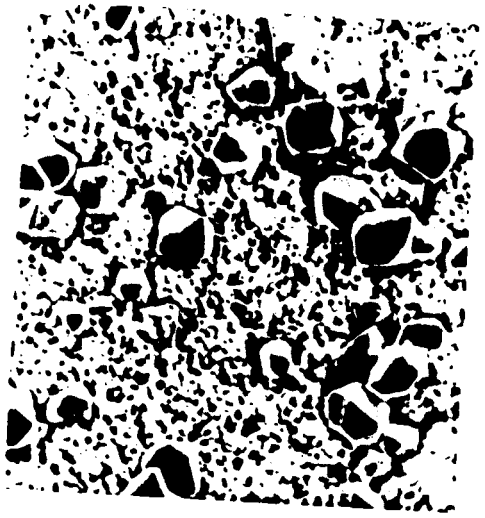

a

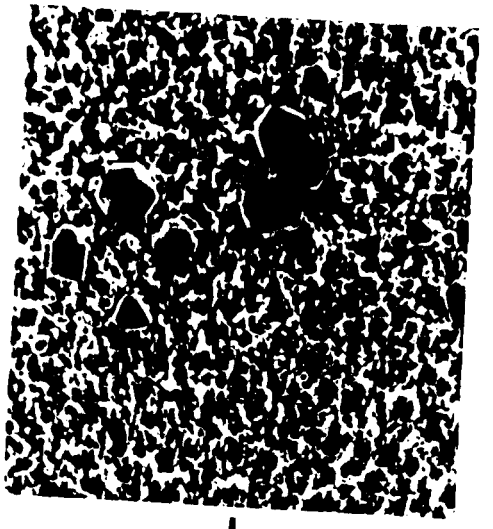

b

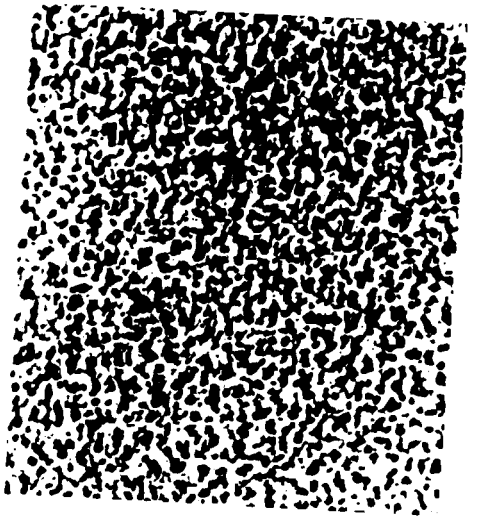

c

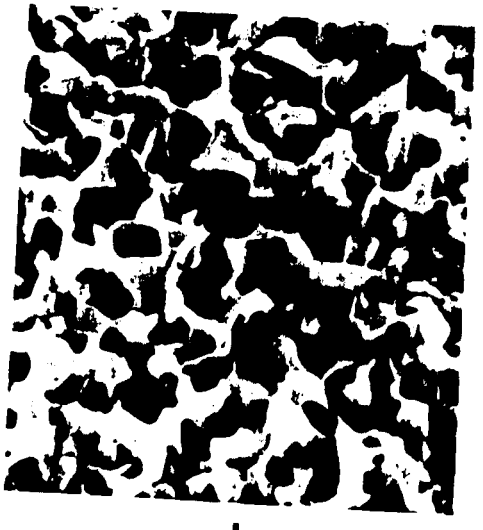

d

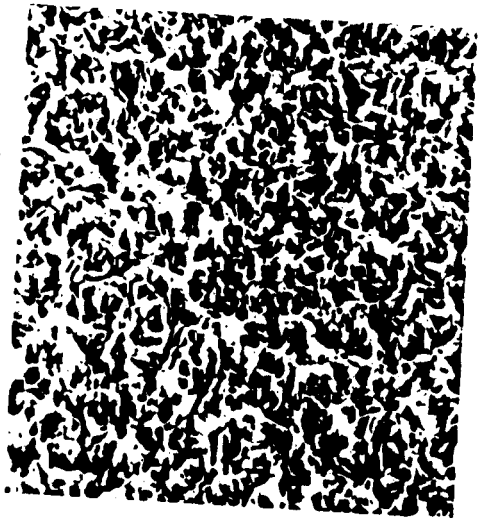

e

10 μm

(1000X)

Figure 5.12 Current-voltage characteristics at 1000 Wm^{-2} white light

The samples were pressed for 5 min (I) and 2 h (II) at pressures of

(a) 11.5 MPa

(b) 23 MPa

(c) 46 MPa

(d) 69 MPa

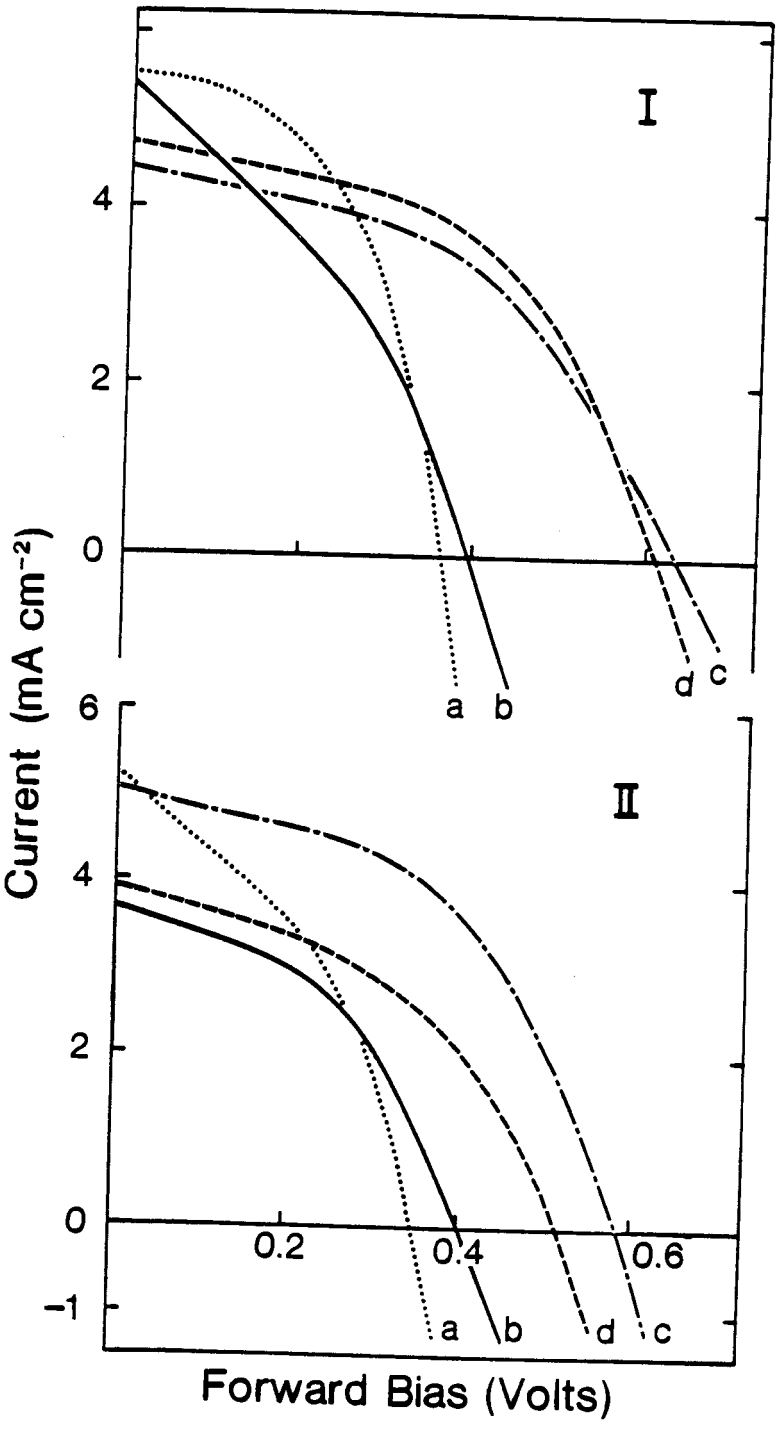
I
II
4
2
0
6
4
2
0
-1
0.2
0.4
0.6
a
b
c
d
Current (mA cm⁻²)
Forward Bias (Volts)

Figure 5.13 Dark current-voltage characteristics of the electrodes of Fig. 5.12

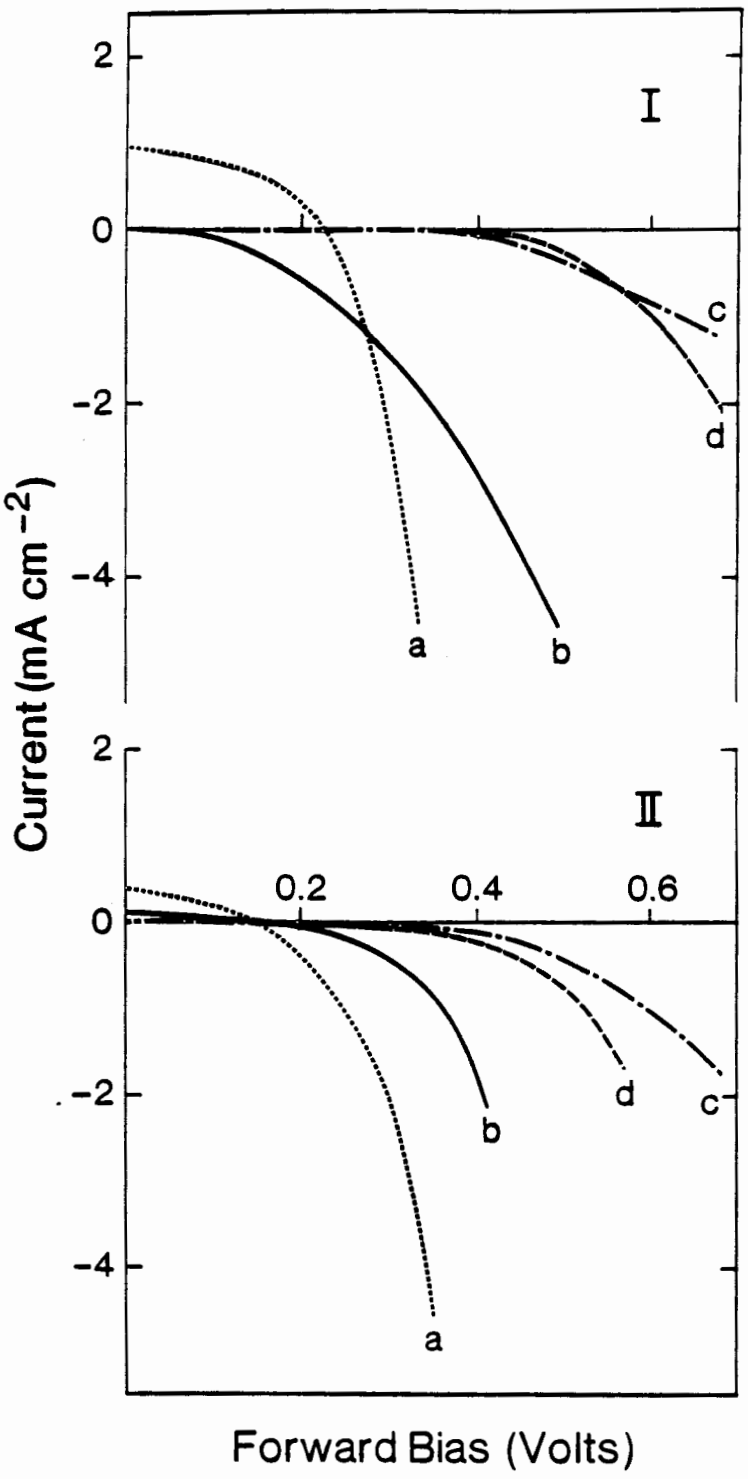
2
0
-2
-4
I
a
b
c
d
2
0
-2
-4
II
0.2
0.4
0.6
a
b
d
c
Current (mA cm^{-2})
Forward Bias (Volts)

Figure 5.14 Dependence of the short circuit current density and the open circuit voltage on the densities of pressed pellets after annealing

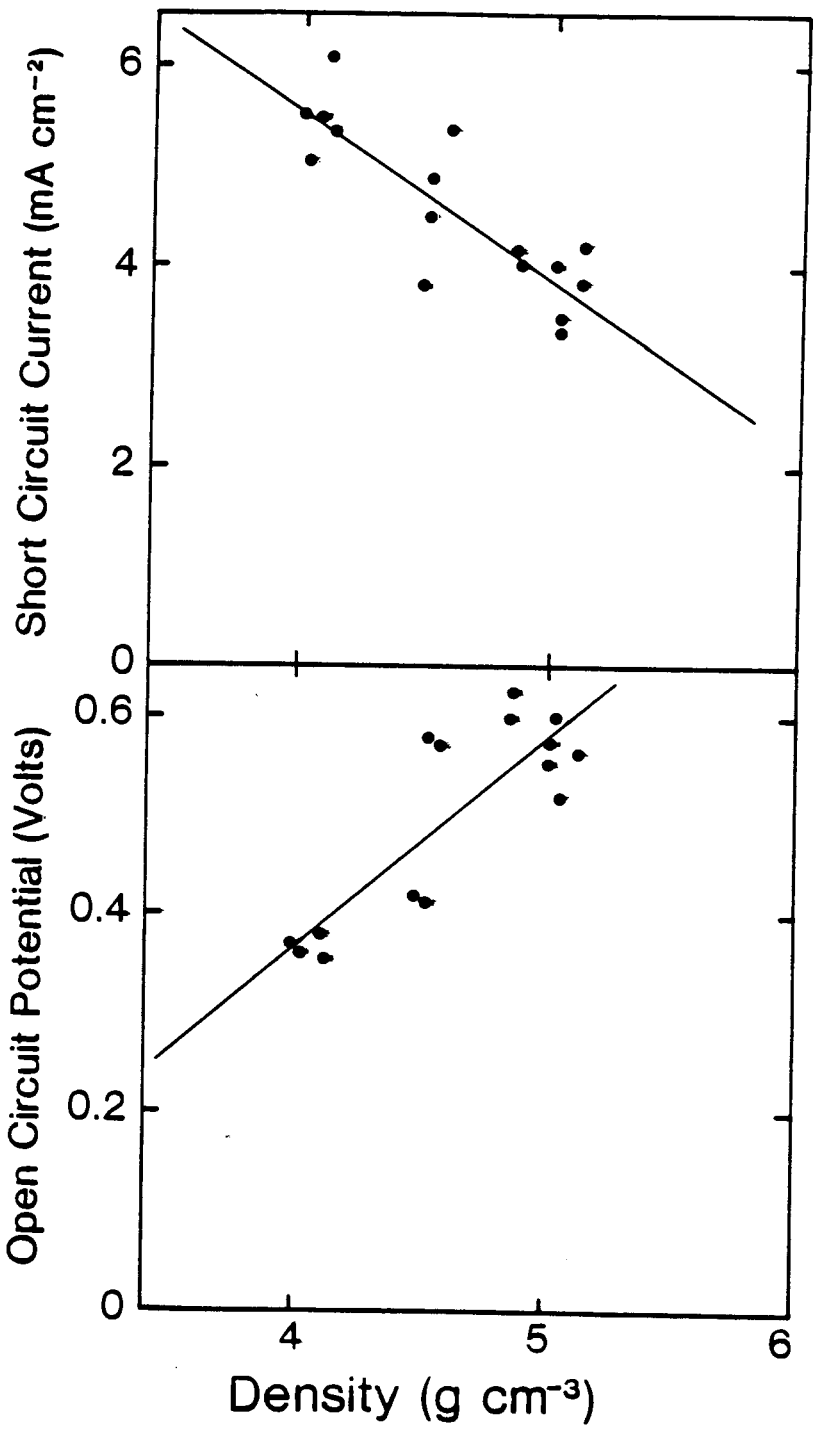
Short Circuit Current (mA cm⁻²)
6
4
2
0
Open Circuit Potential (Volts)
0.6
0.4
0.2
0
4
5
6
Density (g cm⁻³)

Figure 5.15 Voltage dependence of the quantum efficiency at 6328 Å for samples pressed for 5 min (I) and 2 h (II) at pressures of:

(a) 11.5 MPa

(b) 23 MPa

(c) 46 MPa

(d) 69 MPa

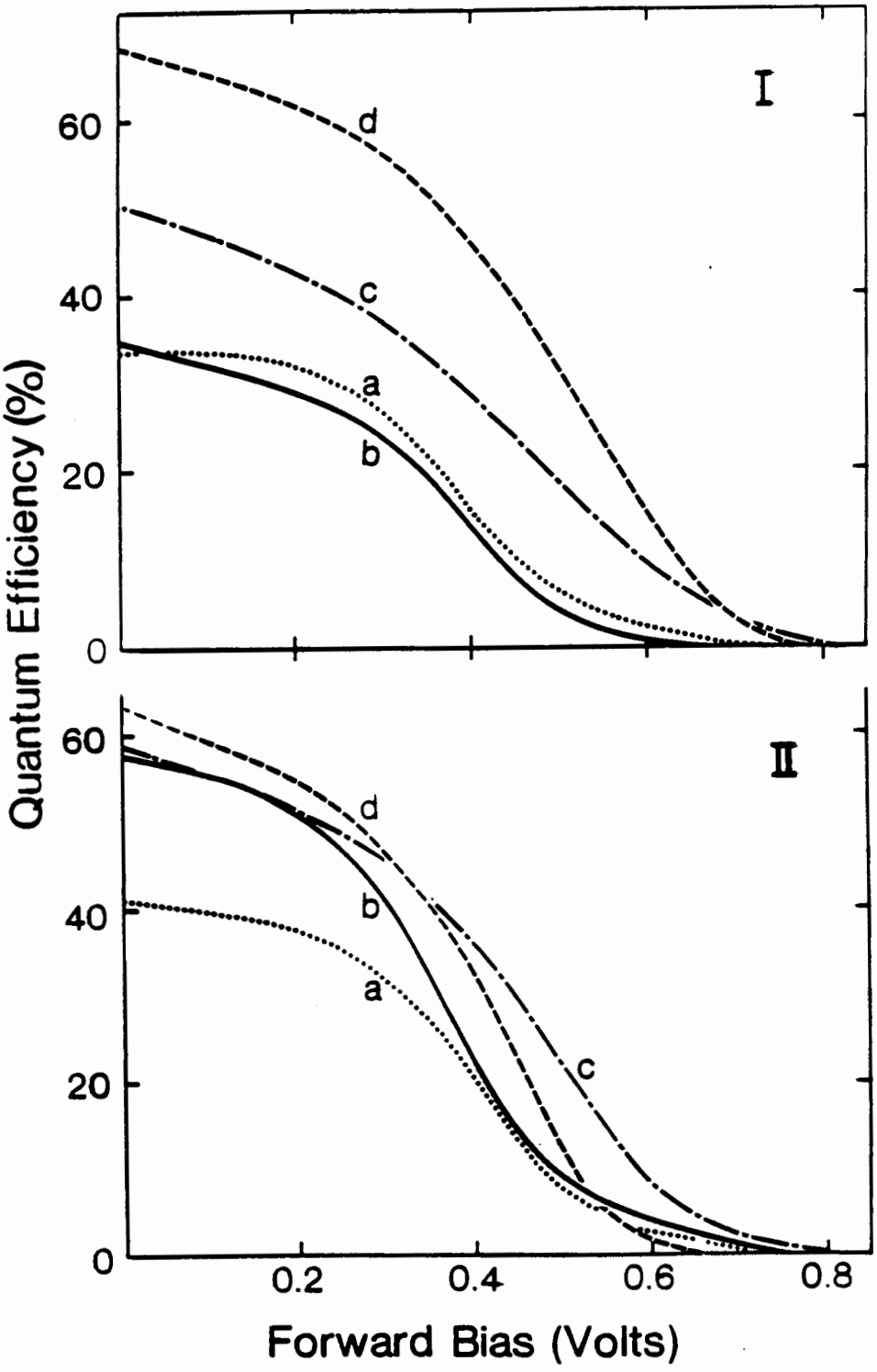
I
II
d
c
a
b
60
40
20
0
0.2
0.4
0.6
0.8
Quantum Efficiency (%)
Forward Bias (Volts)

Figure 5.16 Spectral response of annealed CdSe photoanodes pressed for 2 h at pressures of:

(a) 11.5 MPa

(b) 23 MPa

(c) 46 MPa

(d) 69 MPa

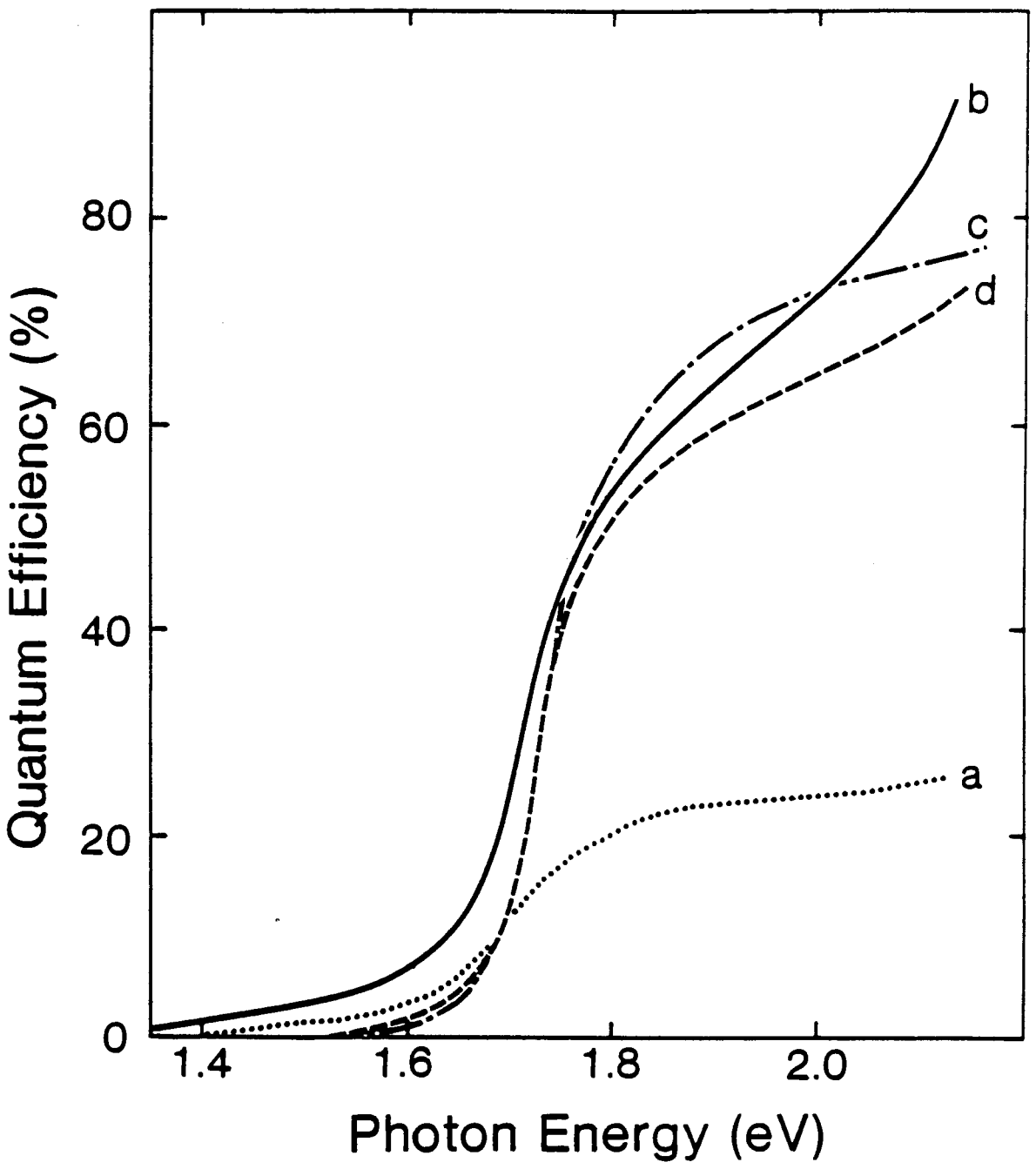
Quantum Efficiency (%)
80
60
40
20
0
1.4
1.6
1.8
2.0
Photon Energy (eV)
b
c
d
a

Figure 5.17 Current-voltage characteristics at 1000 Wm^{-2} white light illumination (a) and in the dark (b) for annealed single crystal CdSe in Cd atmosphere (——) and under vacuum (- - -)

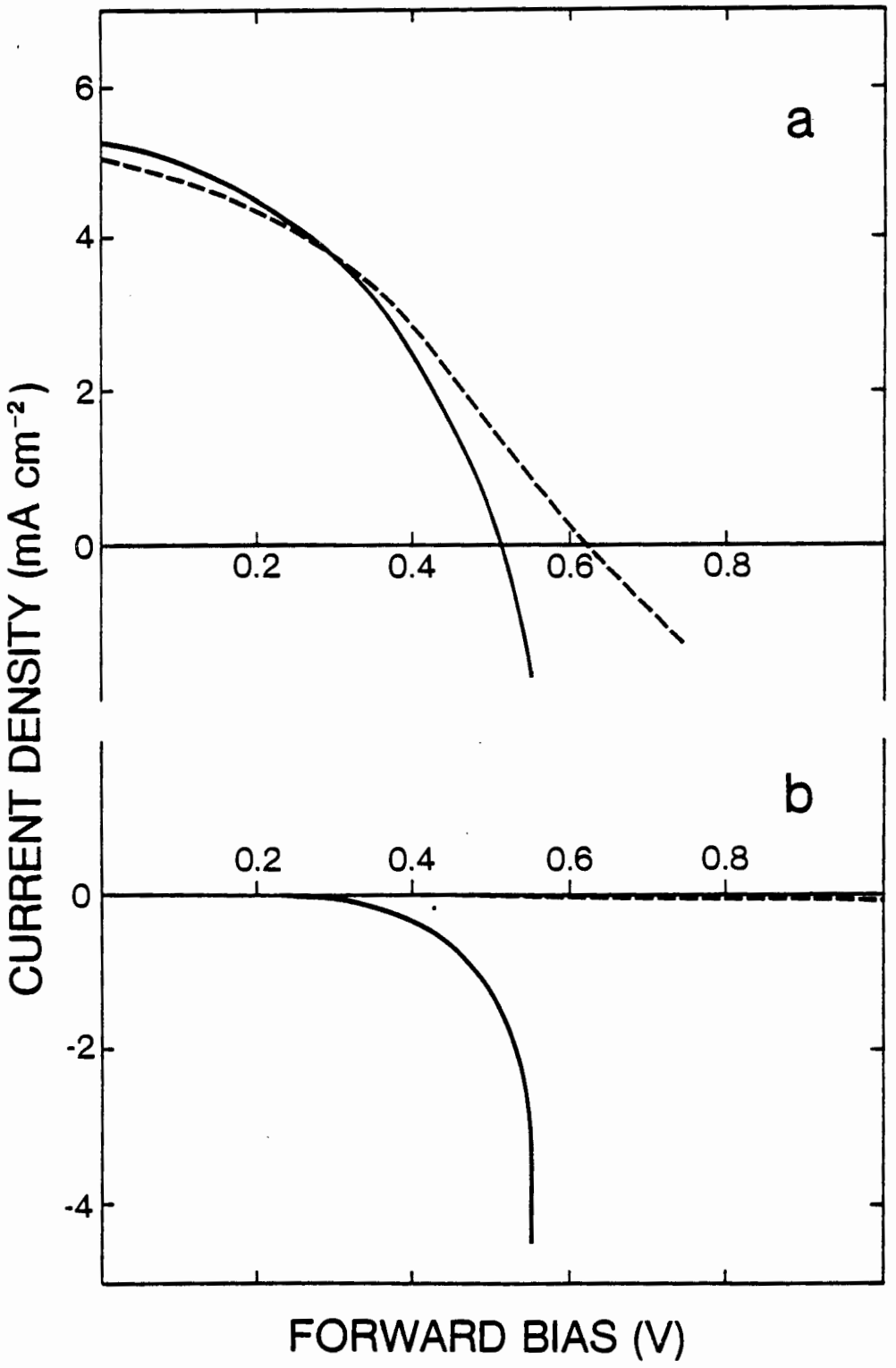
a
b
6
4
2
0
-2
-4
0.2
0.4
0.6
0.8
CURRENT DENSITY (mA cm⁻²)
FORWARD BIAS (V)

Figure 5.18 Voltage dependence of the quantum efficiency at 6328 Å for single crystal CdSe annealed in:

(a) Cd atmosphere

(b) vacuum

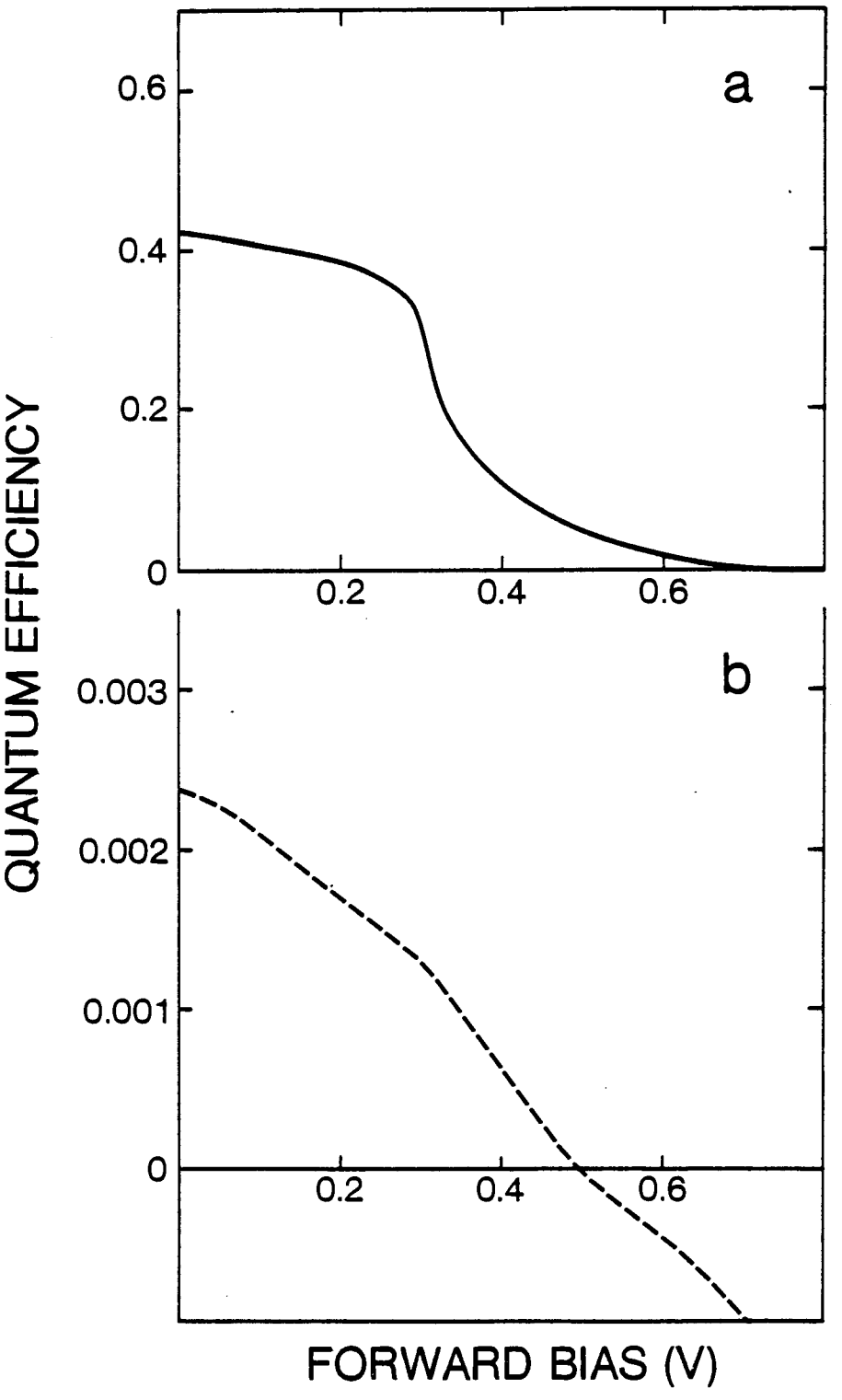
a
b
0.6
0.4
0.2
0
0.2
0.4
0.6
0.003
0.002
0.001
0
0.2
0.4
0.6
QUANTUM EFFICIENCY
FORWARD BIAS (V)

Figure 5.19 Spectral response of single crystal CdSe (batch A) for Cd annealed (———) and vacuum annealed (- - -) electrodes without laser pumping, and the vacuum annealed electrode under laser pumping (·····) Actual efficiencies of the dashed and dotted curve are half as shown.

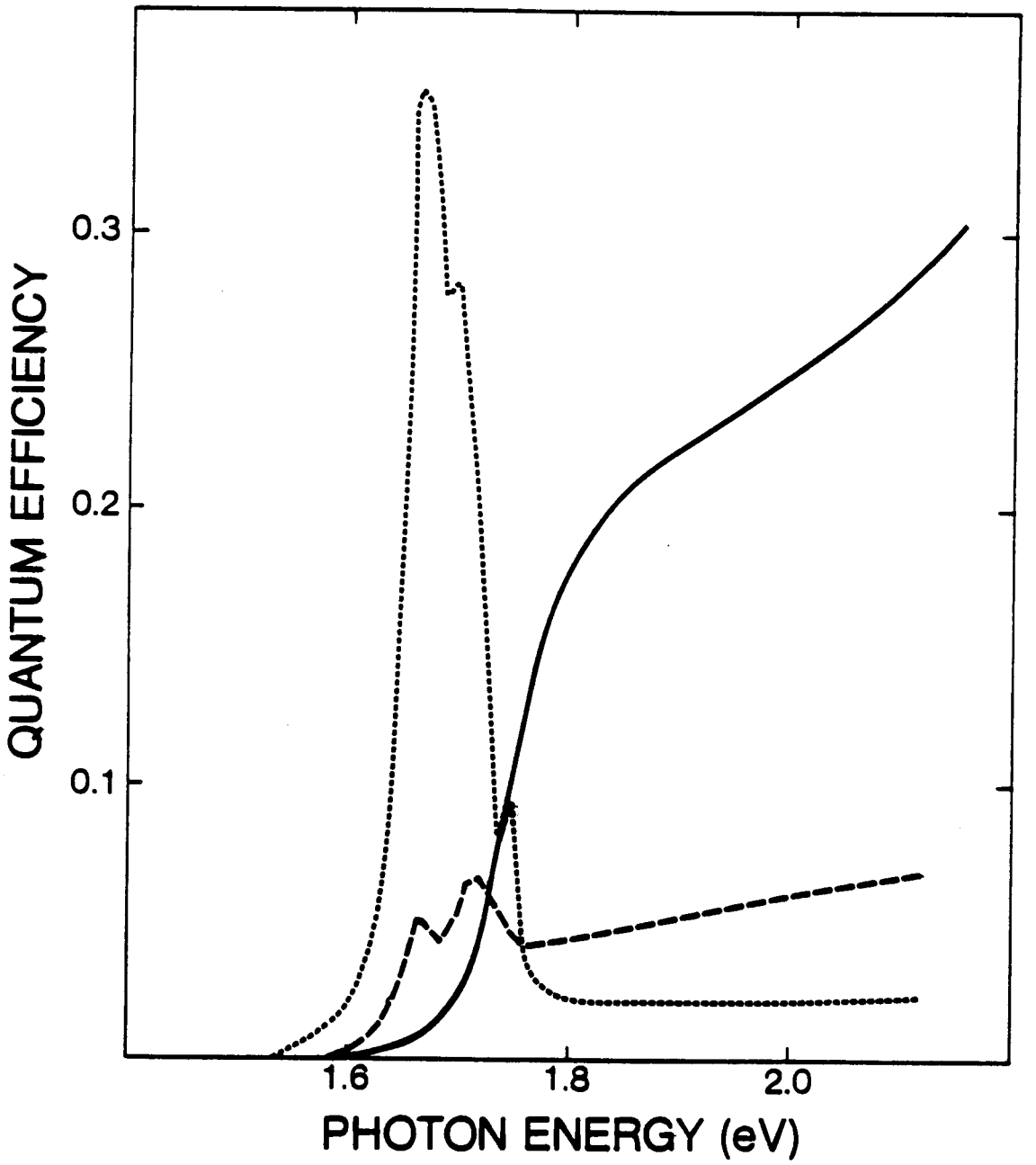
QUANTUM EFFICIENCY
0.3
0.2
0.1
1.6
1.8
2.0
PHOTON ENERGY (eV)

Figure 5.20 Short circuit current wavelength response of vacuum annealed CdSe (batch A) with simultaneous laser pumping for different, relative laser intensities
(Initial laser intensity 10 Wm^{-2})

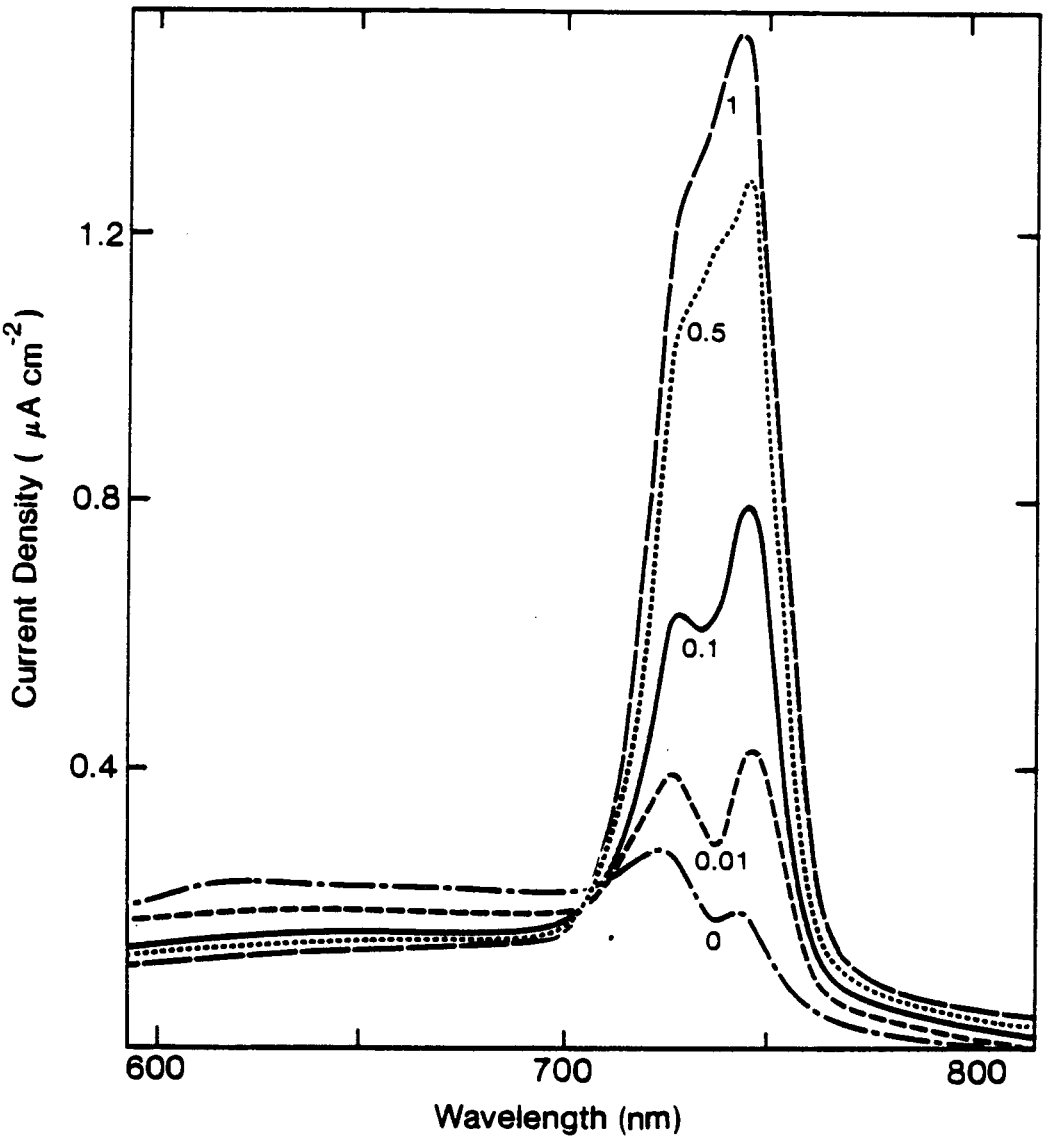
1
0.5
0.1
0.01
0
1.2
0.8
0.4
600
700
800
Current Density (μA cm-2)
Wavelength (nm)

Figure 5.21 Spectral response of single crystal CdSe (batch A) for etched electrodes (———) and anodized electrodes after 30 min (- - -) and 24 h (·····) in redox electrolyte for:

(a) Cd annealed

(b) vacuum annealed

(c) vacuum annealed CdSe with laser pumping

All curves in (b) show twice and the dotted line in (c) one third of the actual efficiencies.

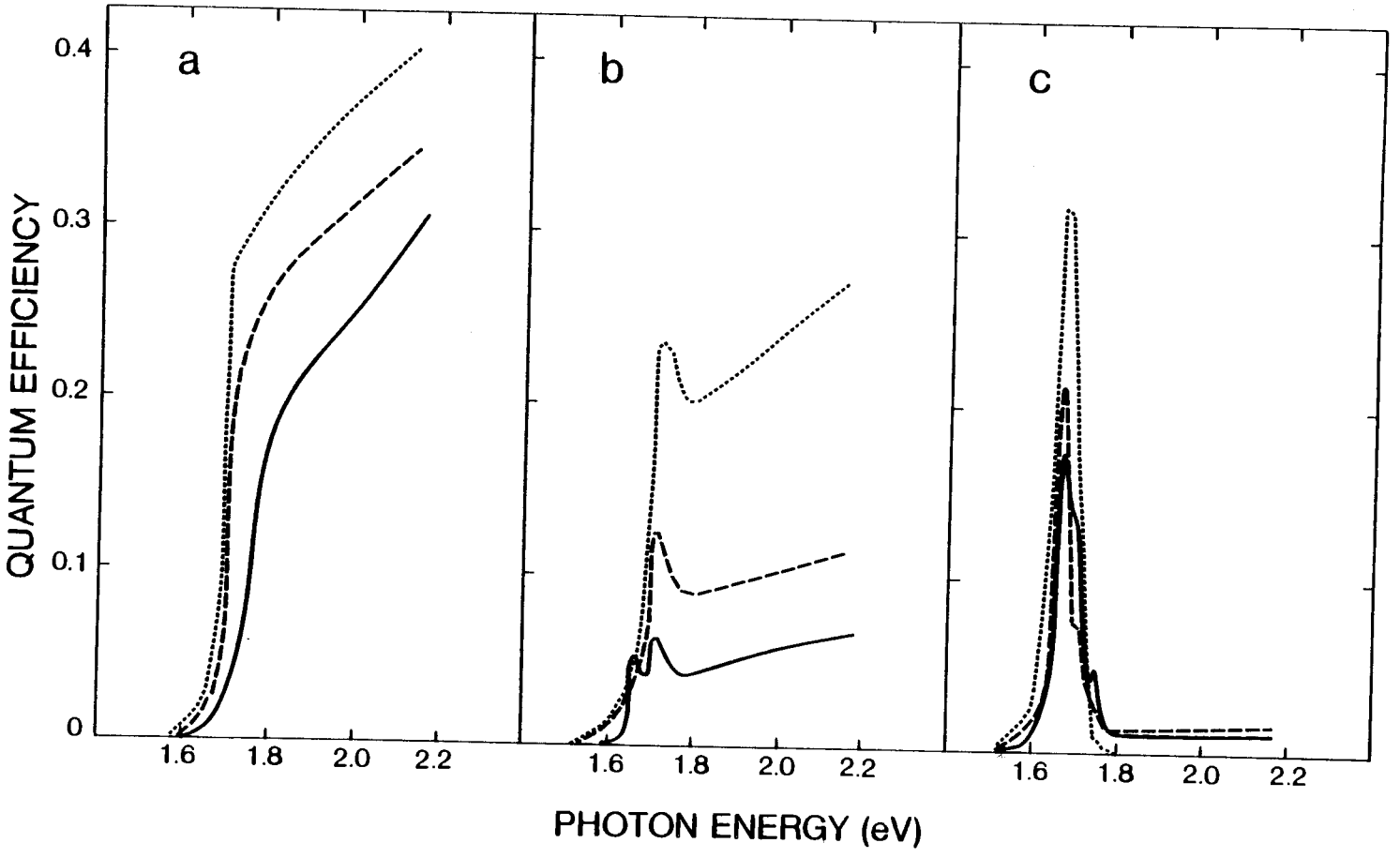
a
b
c
QUANTUM EFFICIENCY
0.4
0.3
0.2
0.1
0
1.6
1.8
2.0
2.2
PHOTON ENERGY (eV)

Figure 5.22 Spectral response of single crystal CdSe (batch B). (a) shows the behaviour of untreated (———) and Cd annealed (- - -) electrodes; (b) and (c) vacuum and Se annealed CdSe, respectively, with (- - -) and without (———) laser pumping.

The solid line in (b) shows 10 times and both curves in (c) 500 times the actual efficiencies.

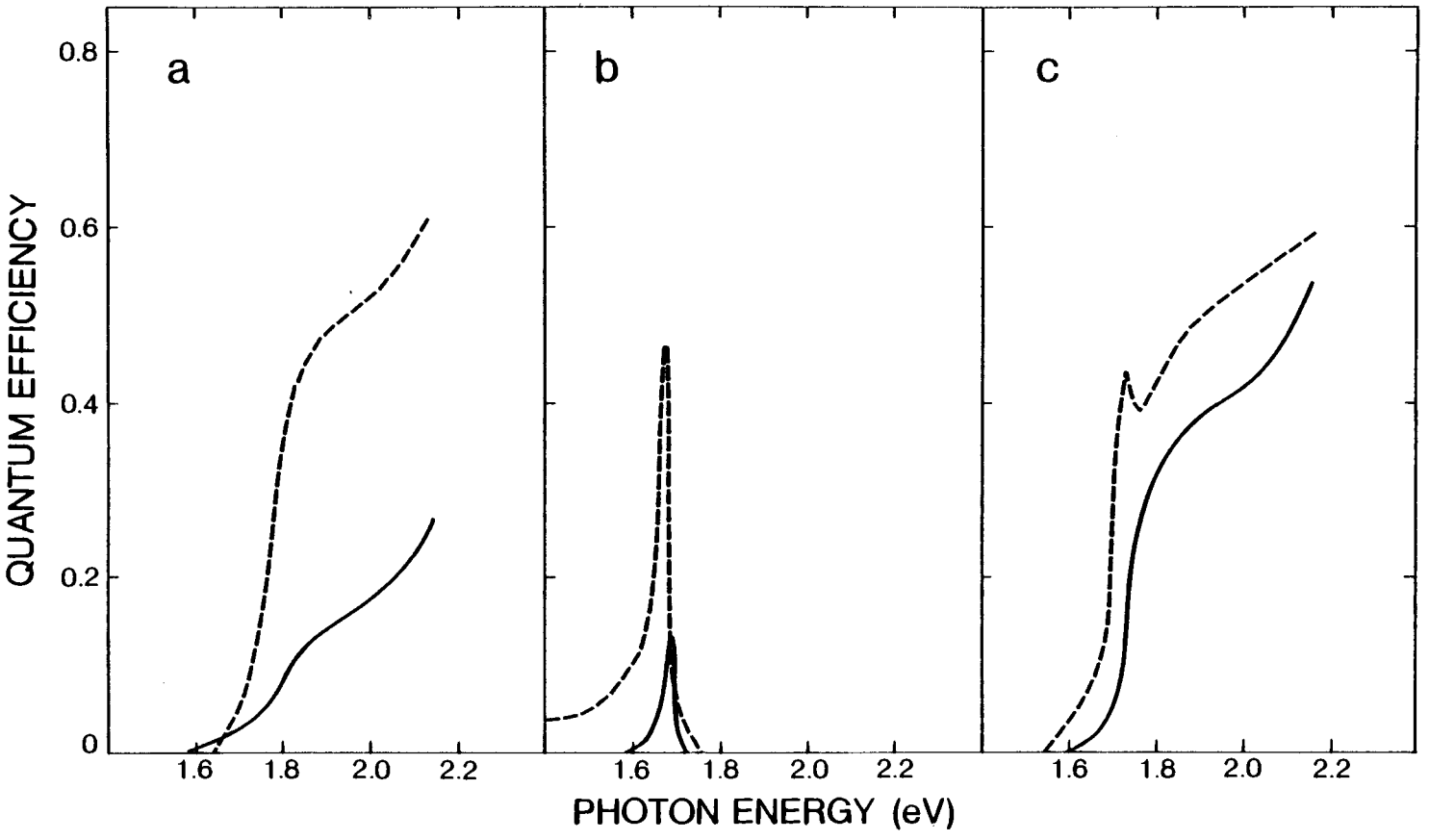
a
b
c
QUANTUM EFFICIENCY
0.8
0.6
0.4
0.2
0
1.6
1.8
2.0
2.2
PHOTON ENERGY (eV)

Figure 5.23 Current-voltage characteristics at 1000 Wm^{-2} white light illumination for Cd annealed single crystal (———), pressed pellet (- - -) and electroplated (·····) CdSe

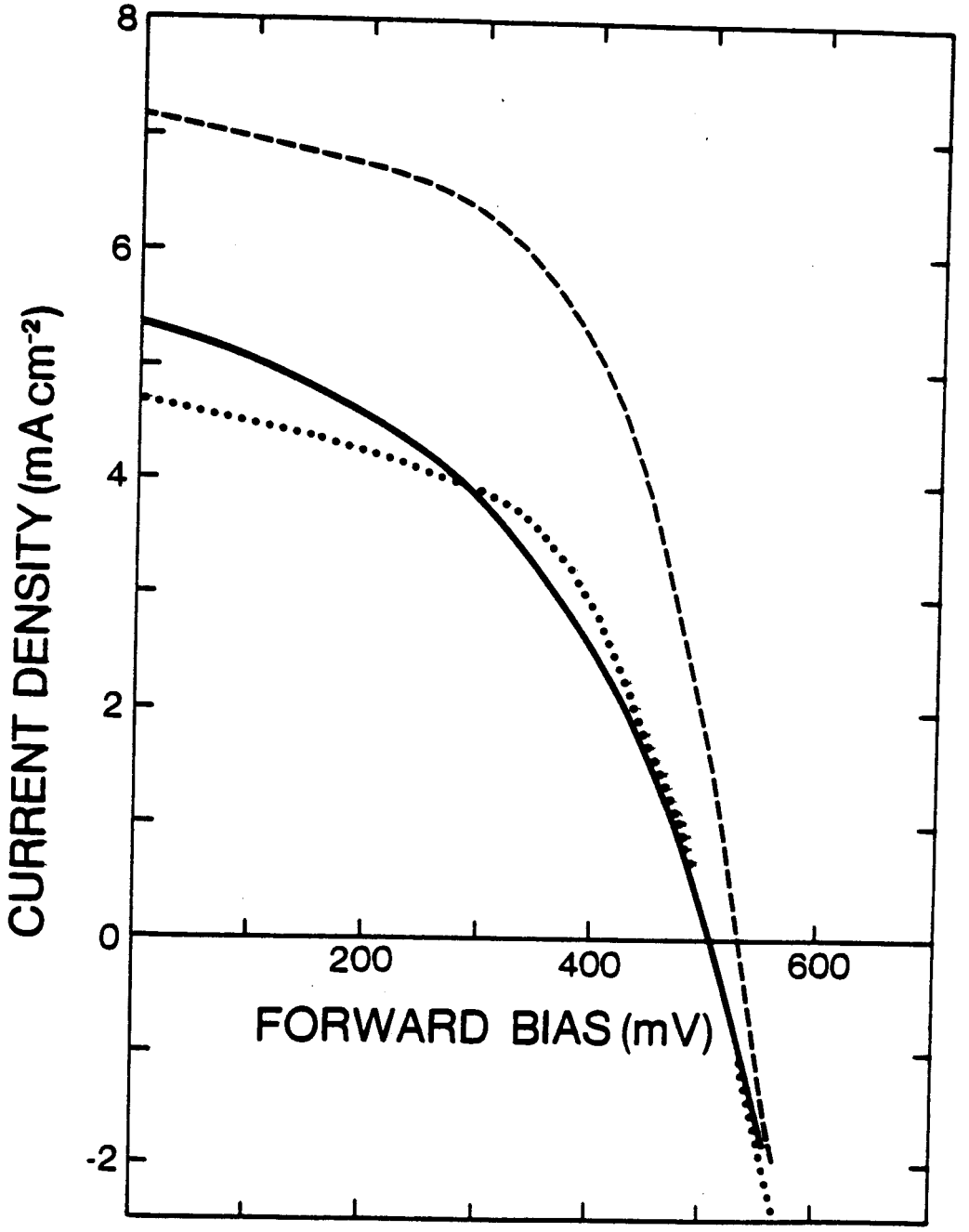
8
6
4
2
0
-2
200
400
600
CURRENT DENSITY (mA cm⁻²)
FORWARD BIAS (mV)

Figure 5.24 Electron micrographs of annealed CdSe at 1000X magnification for an electroplated sample (a) and a pressed pellet (b)

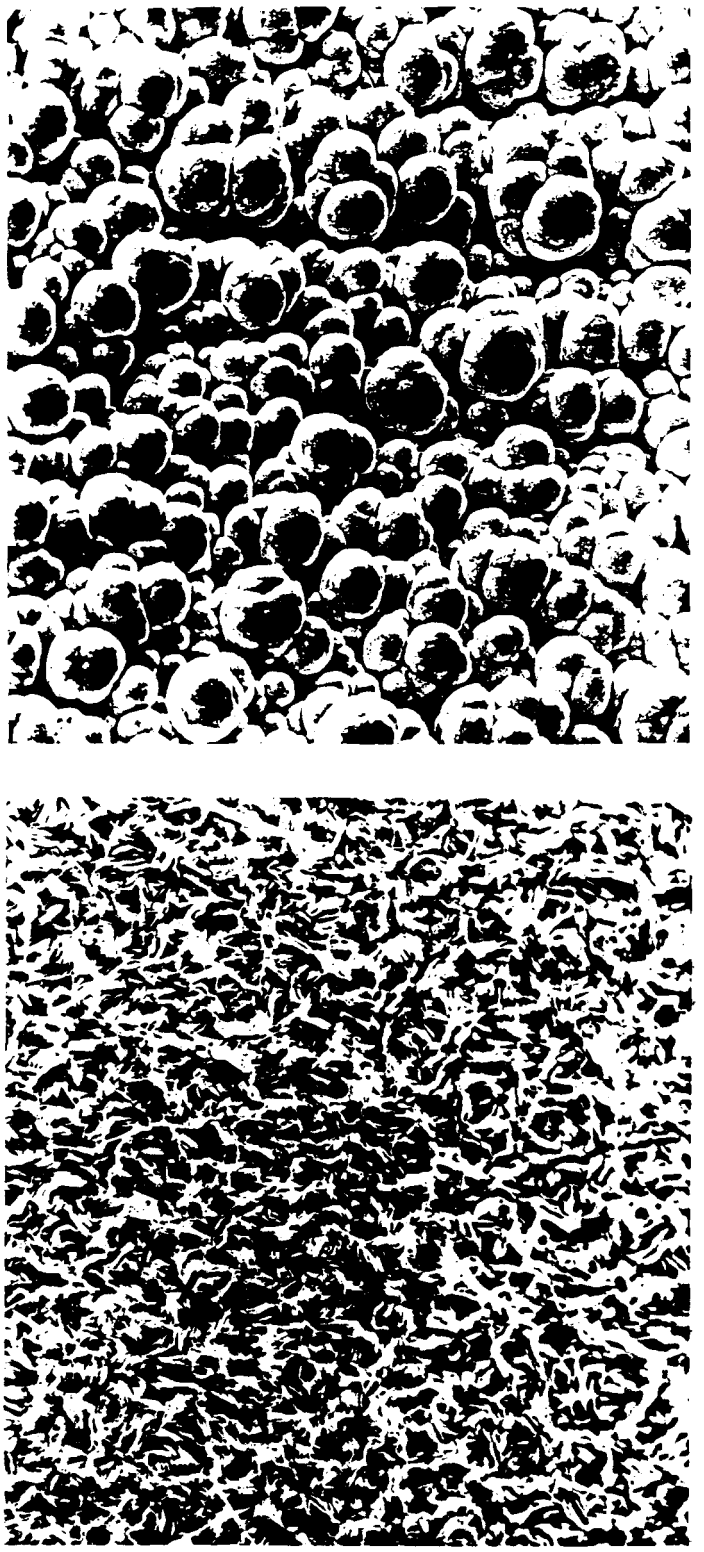

a

b

10 µm

(1000 x)

Figure 5.25 Voltage dependence of the quantum efficiency at 6328 Å for single crystal (Cd annealed) (———), pressed pellet (- - -), and electroplated (·····) CdSe

The circles represent calculated values.

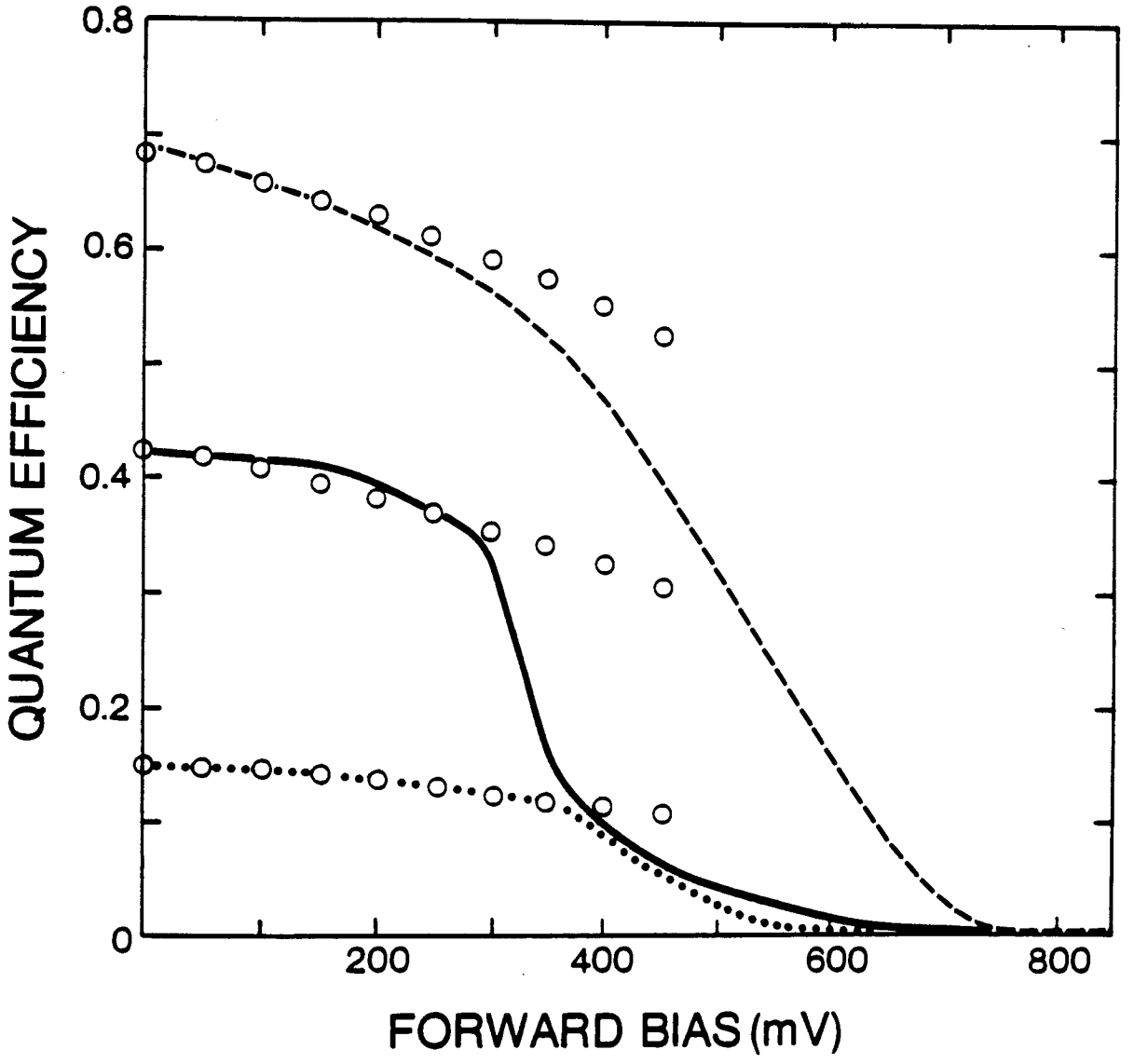
0.8
0.6
0.4
0.2
0
QUANTUM EFFICIENCY
200
400
600
800
FORWARD BIAS (mV)

Figure 5.26 Spectral response of Cd annealed single crystal (———), pressed pellet (- - -), and electro-plated (·····) CdSe

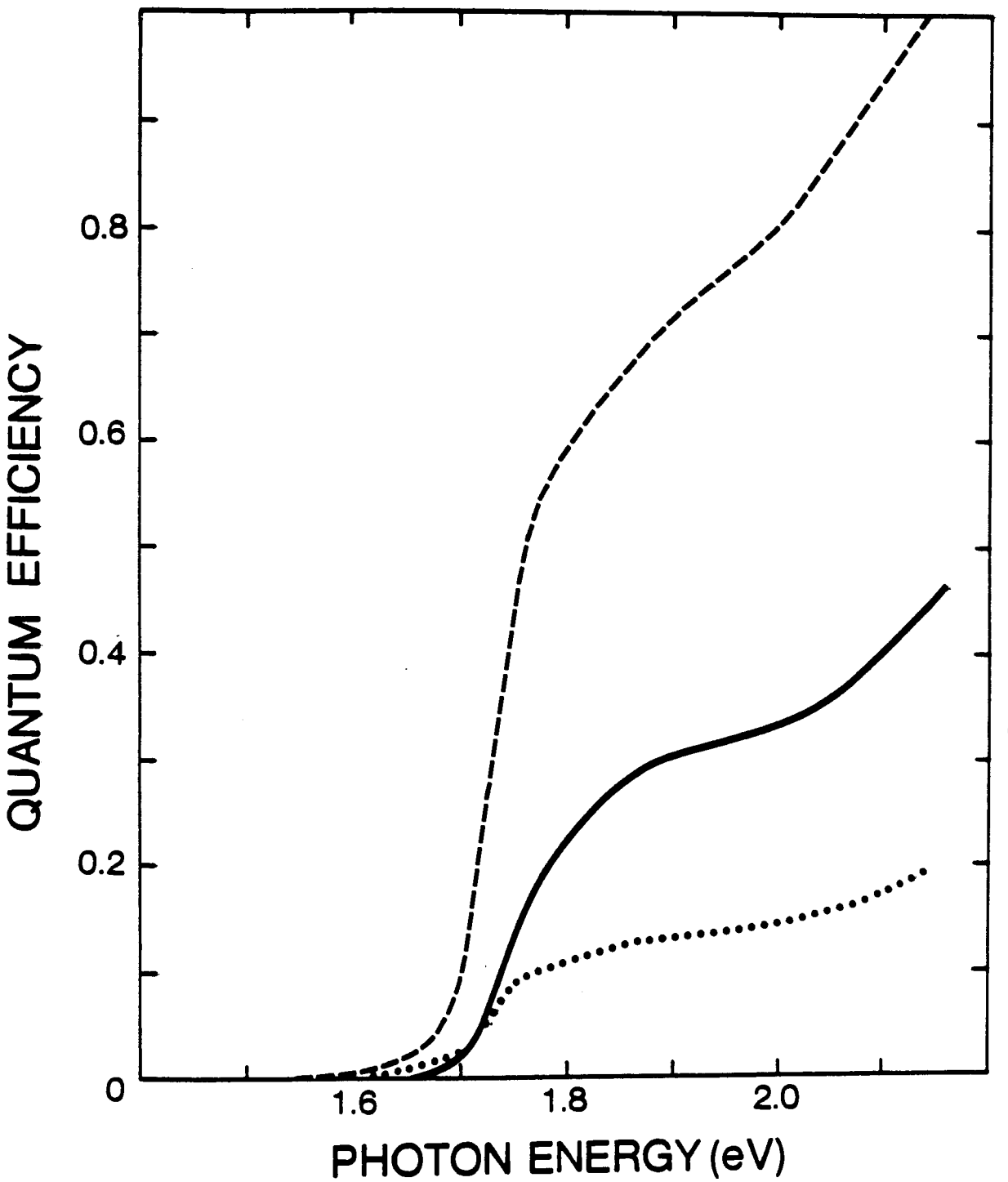
QUANTUM EFFICIENCY
0.8
0.6
0.4
0.2
0
1.6
1.8
2.0
PHOTON ENERGY (eV)

Figure 5.27 Bandgap determination plot of $(\eta h\nu)^2$ vs. photon energy $h\nu$ for single crystal (———), pressed pellet (- - -), and electroplated (·····) CdSe

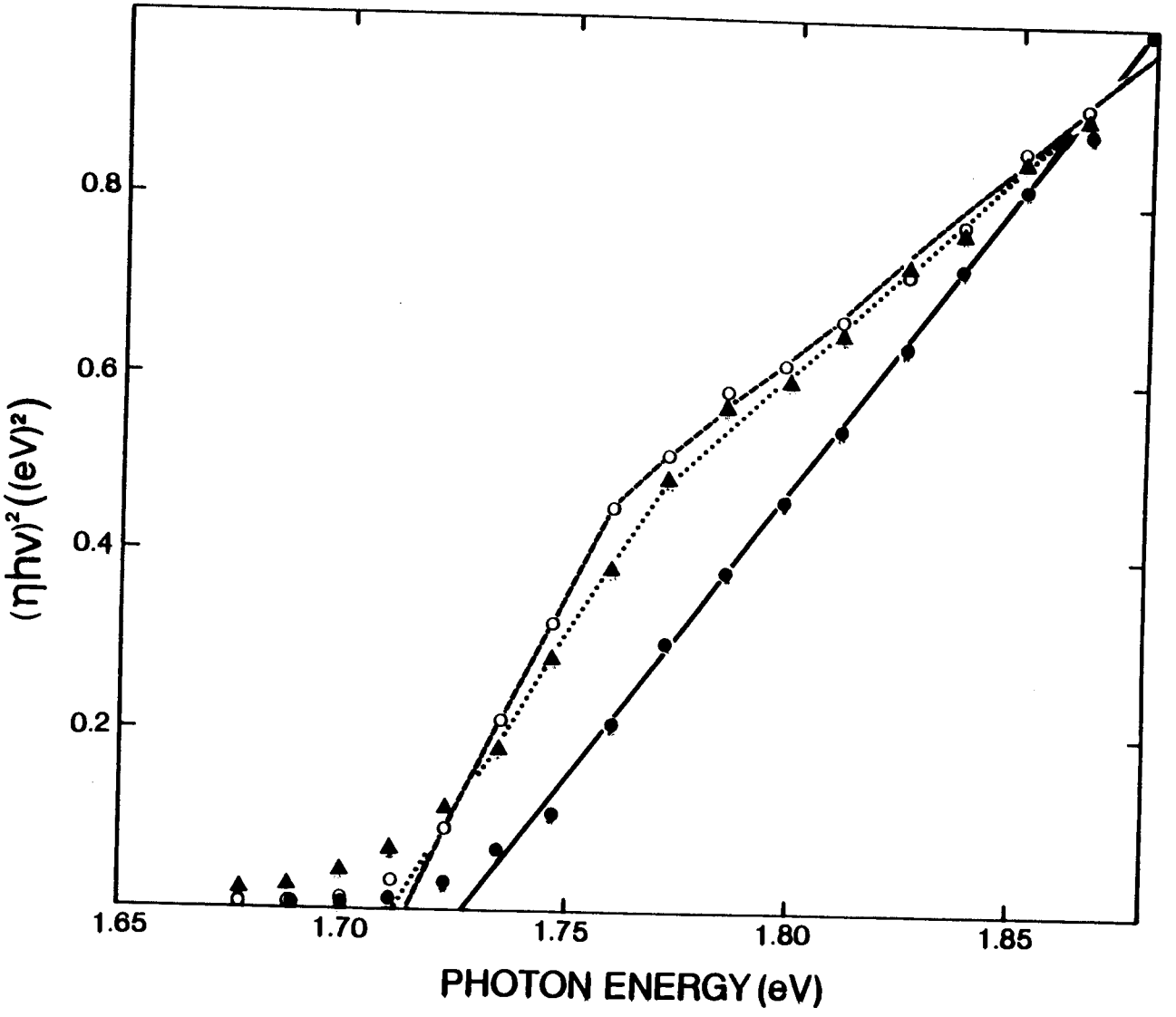
0.8
0.6
0.4
0.2
$(\eta h\nu)^2((eV)^2)$
1.65
1.70
1.75
1.80
1.85
PHOTON ENERGY (eV)

Figure 5.28 Effect of $ZnCl_2$ dipping on the I-V characteristics of pressed pellet electrodes

(———) dipped for 30 min in 1 M $ZnCl_2$ at room temperature

(- - -) untreated

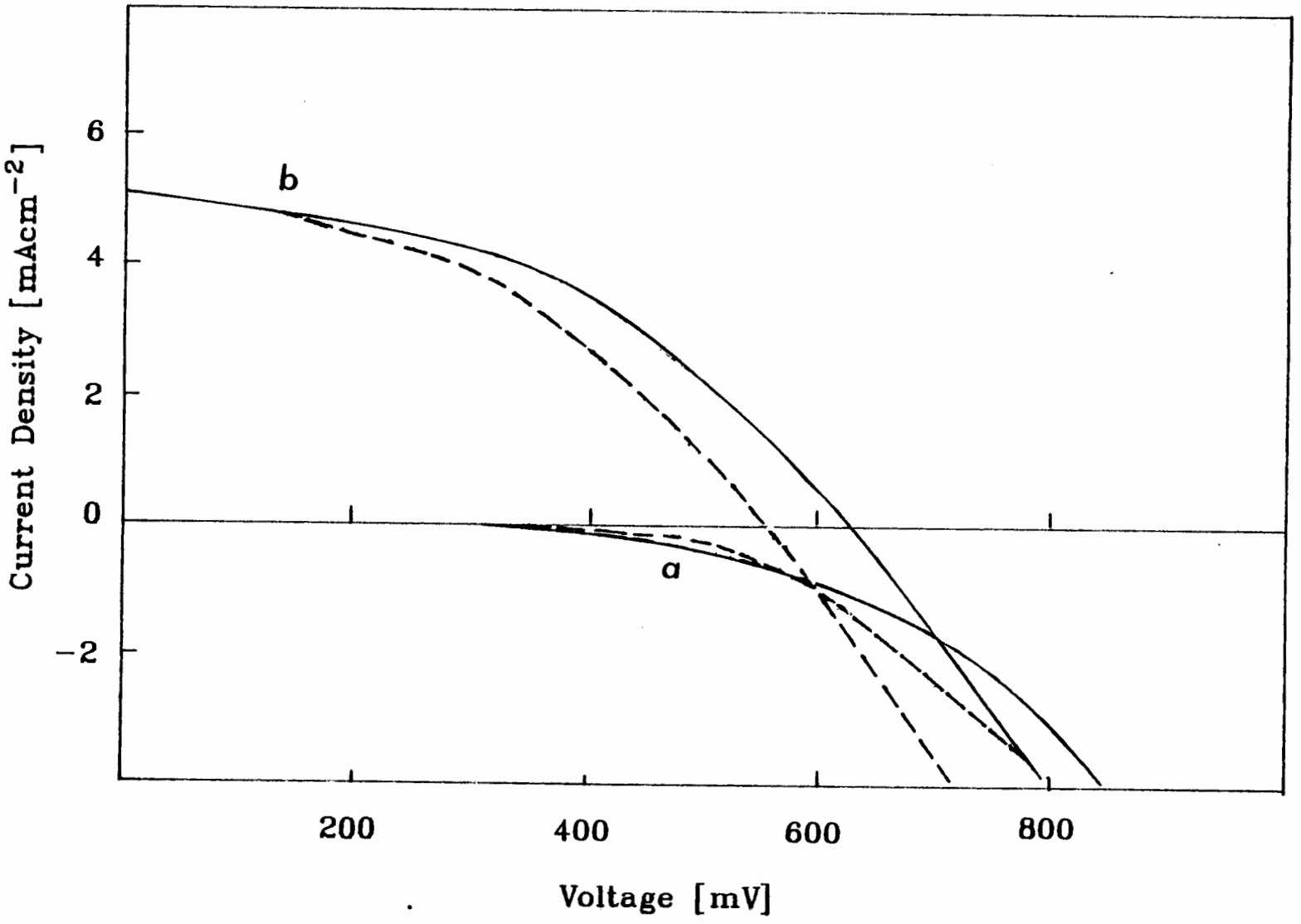
Current Density [mAcm^{-2}]
6
4
2
0
-2
b
a
200
400
600
800
Voltage [mV]

Figure 5.29 The quantum efficiency-voltage characteristics of the electrodes shown in Fig. 5.28

(a) dipped electrode

(b) untreated electrode

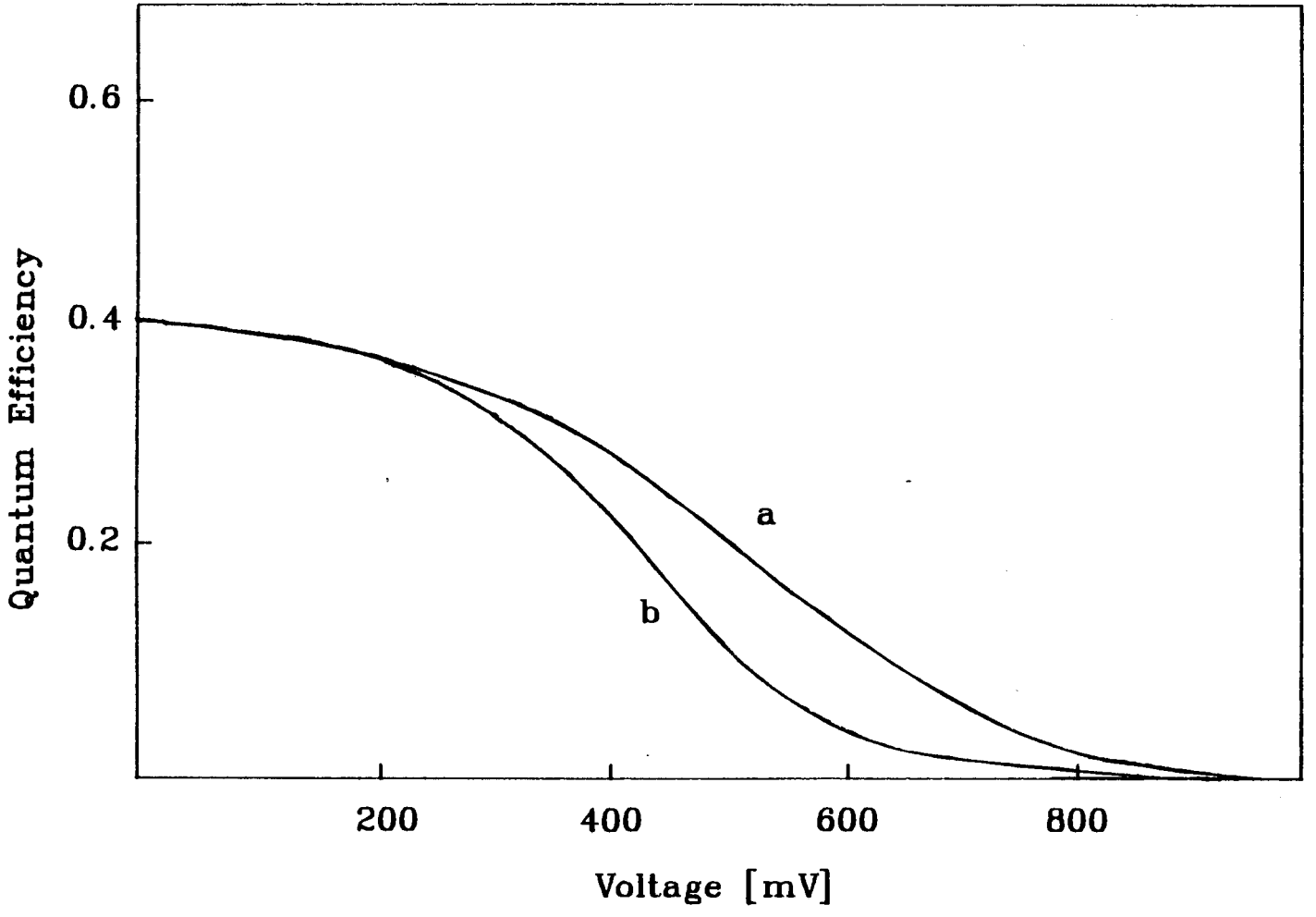
Quantum Efficiency
0.6
0.4
0.2
200
400
600
800
Voltage [mV]
a
b

Figure 5.30 Comparison of the I-V characteristics of a $ZnCl_2$ dipped (———) and a $HgCl_2$ dipped (- - -) pressed pellet with the untreated photoanode (·····)
The dipped electrodes were immersed for 30 min in 1M ion solution at room temperature.
(a) in the dark
(b) illuminated with white light of 1000 Wm^{-2} intensity

Current Density [mAcm^{-2}]
9
3
0
200
400
600
Voltage [mV]
a
b

Figure 5.31 Effect of $ZnCl_2$ dipping on the I-V characteristics of an electroplated CdSe electrode

(———) dipped for 30 min in 1 M solution at room temperature

(- - -) untreated

(a) in the dark

(b) illuminated with white light of 1000 Wm^{-2} intensity

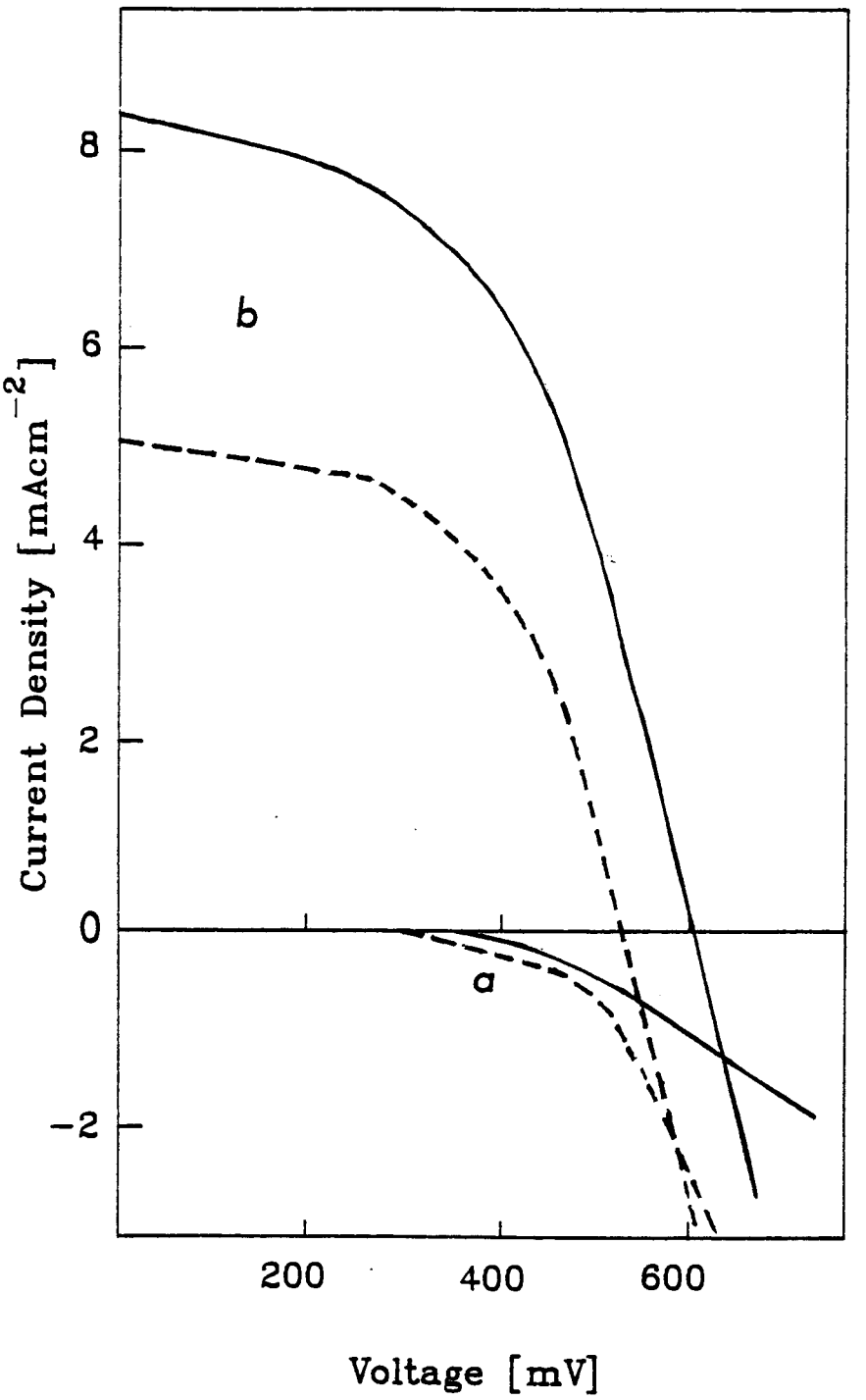
8
6
4
2
0
−2
b
a
200
400
600
Current Density [mAcm^{-2}]
Voltage [mV]

Chapter 6

Summary and Conclusions

Electroplated, cold pressed, and single crystal CdSe photoanodes in polysulfide electrolyte were investigated and compared.

Annealing of both electroplated and pressed electrodes greatly increased the solar performance, possibly due to crystallite growth, increased homogeneity, and improved stoichiometry. Annealed, electroplated CdSe films showed microcracks and bare spots which most likely arose from the differential thermal expansion coefficient between the substrate and the CdSe thin film. Etching of annealed, electroplated CdSe electrodes resulted in an increased photocurrent density possibly due to an increase in active surface area.

Cold pressed CdSe electrodes were prepared at various pressures of 11.5, 23, 46, or 69 MPa. Annealing increased the density of the pressed samples 13 to 22 %, with the highest increase occuring for samples pressed at the lowest pressure. Cadmium selenide pellets prepared at low pressures revealed higher short circuit currents but lower open circuit voltages than pellets pressed at high pressures; this was attributed to a

smaller grain size.

Annealing of single crystal CdSe under vacuum produced a Se surface layer and probably a large density of bulk defect states, possibly due to Se interstitials. This resulted in an unusual spectral response with two strong, distinct bands below the CdSe absorption edge of 1.73 eV, and a decreased efficiency for highly absorbed light due to large recombination near the semiconductor surface. Simultaneous pumping with a He-Ne laser enhanced the unusual spectral characteristics. This may be accounted for by assuming that the laser light is strongly absorbed in the larger bandgap Se surface layer, where electron trapping leads to larger bandbending and thus an increased depletion layer width in the CdSe. This would lead to an improved quantum efficiency for photon energies smaller than the bandgap energy.

The quantum efficiency enhancement by the laser could possibly be attributed to a photoconductivity effect, i.e. a lowering of the series resistance by penetrating light, which was observed for the high resistance vacuum annealed samples. However, the photoconductivity reduced the series resistance by only 40 % which is not sufficient to account for the observed data.

Annealing of single crystal CdSe in Cd atmosphere improved the solar performance considerably compared to the untreated crystals. This effect could be associated with better stoichiometry and a reduction in defect states.

Comparison of the current-voltage characteristics, voltage dependence of the quantum efficiency, and the spectral response of the electroplated, pressed, and single crystal CdSe photo-anodes showed that the pressed pellet electrodes had the best solar performance. This was attributed to a lower defect concentration and thus wider depletion layer for the pressed pellets than for the electroplated or single crystal electrodes. Analysis of the spectral response indicated a bandgap of 1.73 eV for the single crystals, and a bandgap of 1.71 eV for both the pressed pellet and electroplated samples.

Dipping the CdSe electrodes in $ZnCl_2$ solution led to a pronounced increase in the open circuit voltage which was due to the decreased dark current; dipping in $HgCl_2$ solution revealed a decrease in the open circuit voltage. These effects were attributed to a large shift of the surface states arising from strongly adsorbed Zn^{2+} ions and a small shift from weakly adsorbed Hg^{2+} ions.

The efficiencies of both electroplated and single crystal CdSe electrodes were in the range of 2 to 4 % ; pressed electrodes seem most promising for solar energy conversion with efficiencies of up to 6.7 % . The thinnest pellets, 0.25±0.02 mm in thickness and ten times thicker than required from optical considerations, assure material costs of $ 8 per peak watt, which is comparable to the present cost of single crystal Si solar cells.

Cadmium selenide electrochemical photovoltaic cells will

only be economically competitive if they can be produced in large area arrays. Although electrodeposited CdSe electrodes have a greater potential for large-scale production than pressure sintered electrodes, the pressed electrodes can be prepared with higher purity, assuring better conversion efficiencies. The future of electrochemical solar cells most likely does not lie in photovoltaics since they may not be able to compete with polycrystalline solid state Si solar cells, but in photocatalysis and in solar assisted fuel cells.

In conclusion, this thesis demonstrates the superior solar performance of pressure sintered CdSe electrodes with respect to electrodeposited and single crystal photoanodes and the effect of annealing single crystal CdSe under vacuum or in Cd atmosphere on their solar performance.

Appendix A

Hole Diffusion Current in the Neutral Region

The hole density p in the bulk of the semiconductor (x>W) is determined from the diffusion equation, given by:

$$D_p \frac{d^2p}{dx^2} - \frac{p_o - p}{\tau} + g(x) = 0 \qquad (A1)$$

where τ is the hole lifetime, p_o is the equilibrium hole density and g(x) is the electron-hole pair generation represented by eq. (2.12). The diffusivity, D_p, is given by:

$$L_p^2 = D_p \tau \qquad (A2)$$

where L_p is the hole diffusion length. Substitution of eq. (A2) into (A1) yields:

$$\frac{d^2p}{dx^2} - \frac{p}{L_p^2} = -\frac{p_o}{L_p^2} - \frac{g(x)}{D_p} \quad . \qquad (A3)$$

The roots of the homogeneous differential equation are $\pm L_p^{-1}$ and thus the solution of eq. (A3) is given by:

$$p = c_1 \exp\left(\frac{x}{L_p}\right) + c_2 \exp\left(\frac{-x}{L_p}\right) + \frac{L_p}{2}\exp\left(\frac{x}{L_p}\right)\int f(x)\exp\left(\frac{-x}{L_p}\right)dx - \frac{L_p}{2}\exp\left(\frac{-x}{L_p}\right)\int f(x)\exp\left(\frac{x}{L_p}\right)dx \qquad (A4$$

where

$$f(x) = -\frac{p_o}{L_p^2} - \frac{g(x)}{D_p} \qquad (A5)$$

Solving eq. (A4) under the boundary conditions $p = p_o$ at $x = \infty$ and $p = 0$ at $x = W$ yields

$$c_1 = 0$$

and

$$c_2 = -p_o \exp\left(\frac{W}{L_p}\right) - \frac{\phi}{\alpha D_p}\,\frac{\alpha^2 L_p^2}{1 - \alpha^2 L_p^2}\exp\left(-\alpha W + \frac{W}{L_p}\right). \qquad (A6)$$

Thus eq. (A4) becomes:

$$p = p_o - p_o \exp\left(\frac{W - x}{L_p}\right) + \frac{\phi}{\alpha D_p} \frac{\alpha^2 L_p^2}{1 - \alpha^2 L_p^2} \exp(-\alpha x)$$

$$- \frac{\phi}{\alpha D_p} \frac{\alpha^2 L_p^2}{1 - \alpha^2 L_p^2} \exp(-\alpha W) \exp\left(\frac{W - x}{L_p}\right) \qquad \text{(A7)}$$

The diffusion current density, J_{Diff}, is related to the hole density by:

$$J_{Diff} = q D_p \left.\frac{dp}{dx}\right|_{x = W} \qquad \text{(A8)}$$

Differentiatng eq. (A7) with respect to x and evaluating at x = W yields:

$$\frac{dp}{dx}(x = W) = \frac{p_o}{L_p} + \frac{\phi}{D_p} \frac{\alpha L_p}{1 + \alpha L_p} \exp(-\alpha W) \; . \qquad \text{(A9)}$$

Substituting eq. (A9) into (A8) results in the diffusion current density, given by:

$$J_{Diff} = \frac{q p_o D_p}{L_p} + q\phi \frac{\alpha L_p}{1 + \alpha L_p} \exp(-\alpha W) \; . \qquad \text{(A10)}$$

The term proportional to p_o is very small and is neglected in the Gärtner/Butler expression in eq. (2.17).

Appendix B

Electrodeposition of CdSe

The electrodeposition mechanism of CdSe from an acidic bath containing $CdSO_4$, SeO_2, and H_2SO_4 was investigated by Kazacos and Miller [130] and Tomkievicz et al. [89]. Kazacos and Miller [130] observed that the reduction of seleneous acid, H_2SeO_3, in strong acidic medium depends on the electrode material. They reported the following reaction mechanism for Au, Pt, and C substrates:

$$H_2SeO_3 + 6\ H^+ + 6\ e^- \longrightarrow H_2Se + 3\ H_2O \qquad (B1)$$

and

$$2\ H_2Se + H_2SeO_3 \longrightarrow 3\ Se^o + 3\ H_2O\ . \qquad (B2)$$

The authors observed that the rate of the chemical reaction (B2) was dependent on concentration. For H_2SeO_3 concentrations greater than 5 mM, the formation of Se^o was extremely fast, so that the precipitation of CdSe at the electrode surface could not compete favorably with reaction (B2) even at high Cd^{2+} concentrations.

The reaction mechanism on AuHg, Ag, and Cu substrates is

represented by:

$$n\ M + H_2SeO_3 + 4\ H^+ + 4\ e^- \longrightarrow M_nSe + 3\ H_2O \qquad (B3)$$

where M represents the substrate metal [130].

Tomkievicz et al. [89] showed that a Ti substrate behaves electrochemically like the noble metal electrodes. They observed two morphologically distinct phases of CdSe by SEM technique; a smooth structure was formed at the beginning of the deposition, and a cauliflower morphology eventually formed out of the Se^o layer. This observation does not support the reduction mechanism reported by Kazacos and Miller [130].

Tomkievicz et al. [89] proposed the following deposition mechanism. The reduction of Cd^{2+} to Cd on the substrate surface,

$$Cd^{2+} + 2\ e^- \longrightarrow Cd, \qquad (B4)$$

was followed immediately by two reactions, the chemical oxidation of Cd,

$$4\ H^+ + 3\ Cd + H_2SeO_3 \longrightarrow CdSe + 3\ H_2O + Cd^{2+}, \qquad (B5)$$

and/or the electrochemical reduction of H_2SeO_3,

$$Cd + H_2SeO_3 + 4\ H^+ + 4\ e^- \longrightarrow CdSe + 3\ H_2O\ . \qquad (B6)$$

The smooth deposit on the substrate at the beginning of the deposition was attributed to reactions (B5) and (B6). The CdSe was then further attacked by H_2SeO_3 to form

$$2\ CdSe + H_2SeO_3 + 4\ H^+ \longrightarrow 2\ Cd^{2+} + 3\ Se^o + 3\ H_2O \quad . \quad (B7)$$

Reactions (B5), (B6), and (B7) yielded a deposit containing regions of CdSe as well as Se^o. At the point of contact between the two regions, the following two reactions can take place:

$$Se^{2-} + Se \longrightarrow Se_2^{2-} \quad (B8)$$

and

$$Se_2^{2-} + 2\ e^- \longrightarrow 2\ Se^{2-} \quad . \quad (B9)$$

The resulting formation of CdSe at the interface was associated with the cauliflower structure.

Tomkievicz et al. [89] supported the proposed deposition mechanism by the following experimental observations. At high current densities the formation of CdSe was favored while at low current densities, the formation of Se^o was predominant. The initial deposition potential for the reduction of Cd^{2+} to Cd became gradually less negative. After 60 s the potential for the reduction of polyselenide was reached, and at this point, formation of the cauliflower structure was observed.

Bibliography

1. R.E. Schwerzel, in "Third NASA Conference on Radiation Energy Conversion in Space", K.W. Billman (Ed.), p.626 (1978).

2. P.D. Maycock, E.N. Stirewalt, "Photovoltaics", Brick House Publishing Co., Andover, Massachusetts, p.182 (1981).

3. C.E. Backus, "Solar Cells", IEEE Press, New York, p.1 (1976).

4. P. Moon, J. Franklin Institute 230: 583 (1940).

5. J.J. Loferski, J. Appl. Phys. 27: 777 (1956).

6. J. Javetski, Electronics July 19: 105 (1979).

7. F.V. Wald, Photonics Spectra Sept: 42 (1983).

8. A. Heller, B. Miller, in "Energy Storage: Transactions of the First International Assembly Held at Dubrovnic, Yugoslavia", J. Silverman (Ed.), p. 405 (1978).

9. J. O'M. Bockris, "Energy: The Solar Hydrogen Alternative", John Wiley, New York (1975).

10. E. Becquerel, C. R. Acad. Sci. 9: 561 (1839).

11. W.H. Brattain, C.G.B. Garrett, Bell Syst. Tech. J. 34: 129 (1955).

12. H. Gerischer, Z. Phys. Chem. Neue Folge 26: 223 (1960).

13. H. Gerischer, Z. Phys. Chem. Neue Folge 27: 48 (1961).

14. H. Gerischer, Surf. Sci. 18: 97 (1969).

15. H. Gerischer, in "Physical Chemistry: An Advanced Treatise", H.Eyring, D. Henderson, W.Jost (Eds.), Academic Press, New York, 9A: 463 (1970).

16. H. Gerischer, J. Electroanal. Chem. 58: 263 (1975).

17. H. Gerischer, in "Topics in Applied Physics: Solar Energy Conversion", B.O. Seraphin (Ed.), Springer Verlag, Berlin 31: 115 (1979).

18. S.R. Morrison, "Electrochemistry at Semiconductor and Oxidized Metal Electrodes", Plenum Press, New York (1980).

19. S. Kar, K. Rajeshwar, P. Singh, J. DuBow, Solar Energy 23: 129 (1979).

20. B. Miller, A. Heller, M. Robbins, S. Menezes, K.C. Chang, J. Thomson Jr., J. Electrochem. Soc. 124: 1019 (1977).

21. J.J. Wysocki, P. Rappaport, J. Appl. Phys. 31: 571 (1960).

22. W. Gärtner, Phys. Rev. 116: 84 (1959).

23. M. Butler, J. Appl. Phys. 48: 1914 (1977).

24. R.H. Bube, "Photoconductivity of Solids", John Wiley, New York, p.211 (1960).

25. E.J. Johnson, in "Semiconductors and Semimetals", R.K. Willardson, A.C. Beer (Eds.), Academic Press, New York 3: 168 (1967).

26. H. Gerischer, J. Electroanal. Chem. 82: 133 (1977).

27. H. Gerischer, J. Vac. Sci. Tech. 15: 1422 (1978).

28. A. Bard, M.S. Wrighton, J. Electrochem. Soc. 124: 1706 (1977).

29. S.-M. Park, M.E. Barber, J. Electroanal. Chem. 99: 67 (1979).

30. B. Miller, A. Heller, Nature 262: 680 (1976).

31. A.B. Ellis, S.W.Kaiser, M.S. Wrighton, J. Am. Chem. Soc. 98: 1635 (1976).

32. A.B. Ellis, S.W. Kaiser, J.M. Bolts, M.S. Wrighton, J. Am. Chem. Soc. 99: 2839 (1977).

33. A.B. Ellis, J.M. Bolts, S.W. Kaiser, M.S. Wrighton, J. Am. Chem. Soc. 99: 2848 (1977).

34. K.C. Chang, A. Heller, B. Schwartz, S. Menezes, B. Miller, Science, N.Y. 196: 1097 (1977).

35. B.A. Parkinson, A. Heller, B. Miller, Appl. Phys. Lett. 33: 521 (1978).

36. S. Wagner, J. Shay, Appl. Phys. Lett. 31: 446 (1977).

37. A. Heller, Acc. Chem. Res. 14: 154 (1981).

38. C.A. Mead, Appl. Phys. Lett. 6: 103 (1965).

39. C.A. Mead, W.G. Spitzer, Phys. Rev. A 134: 713 (1964).

40. S.M. Sze, "Physics of Semiconductor Devices", John Wiley, New York, 2nd ed., (a)p. 275, (b)p. 9 (1981).

41. A.J. Bard, A.B. Bocarsly, F.F. Fan, E.G. Walton, M.S. Wrighton, J. Am. Chem. Soc. 102: 3671 (1980).

42. P.A. Kohl, A.J. Bard, J. Electrochem. Soc. 126: 59 (1979).

43. F.F. Fan, A.J. Bard, J. Am. Chem. Soc. 102: 3677 (1980).

44. A.B. Bocarsly, D.C. Bookbinder, R.N. Dominey, N.S. Lewis, M.S. Wrighton, J. Am. Chem. Soc. 102: 3683 (1980).

45. H. Tributsch, H. Gerischer, C. Clemen, E. Bucher, Ber. Bunsengesellschaft, Phys. Chem. 83: 655 (1979).

46. B.A. Parkinson, A. Heller, B. Miller, J. Electrochem. Soc. 126: 954 (1979).

47. W.D. Johnston, Jr., H.J. Leamy, B.A. Parkinson, A. Heller, B. Miller, J. Electrochem. Soc. 127: 90 (1980).

48. H.J. Reiss, J. Electrochem. Soc. 125: 937 (1978).

49. R. Wilson, J. Appl. Phys. 48: 4292 (1977)

50. J. Reichman, Appl. Phys. Lett. 36: 574 (1980).

51. F. El Guibaly, K. Colbow, B. Funt, J. Appl. Phys. 52: 3480 (1981).

52. F. El Guibaly, K. Colbow, Can. J. Phys. 59: 1682 (1982).

53. F. El Guibaly, K. Colbow, J. Appl. Phys. 54: 6488 (1983).

54. N. Tarr, D. Pulfrey, Solid State Electron. 22: 265 (1979).

55. F. El Guibaly, K. Colbow, J. Appl. Phys. 53: 1737 (1982).

56. F. El Guibaly, K. Colbow, J. Appl. Phys. 52: 5247 (1981).

57. R.N. Noufi, P.A. Kohl, A.J. Bard, J. Electrochem. Soc. 125: 375 (1978).

58. D. Haneman, G.H.J. Wantenaar, R.C. Kainthla, Solar Energy Mat. 10: 69 (1984).

59. D.M. Chizhikov, V.P. Shchastlivyi, "Selenium and Selenides", Collet's Ltd., London, England, p.225-242 (1968).

60. M.D. Heinz, E. Banks, J. Chem. Phys. 24: 391 (1956).

61. R.W. Parsons, W. Wardzynski, A.D. Yoffe, Proc. Roy. Soc. A 262: 120 (1961).

62. R.E. Schwerzel, E.W. Brooman, R.A. Craig, V.E. Wood, in "Semiconductor Liquid-Junction Solar Cells", A. Heller (Ed.), Proc. Electrochem. Soc. 77-3: 307 (1977).

63. R.H. Bube, Phys. Rev. 98: 431 (1955).

64. K. Hauffe, Annalen der Phys., 15: 141 (1954).

65. G. Hodes, J. Manassen, D. Cahen, Nature 261: 403 (1976).

66. J. Manassen, G. Hodes, D. Cahen, U.S. Patent No. 4 064 326 (1977).

67. S. Chandra, R.K. Pandey, Phys. Stat. Sol. (a) 59: 787 (1980).

68. B. L. Funt, M. Leban, A. Sherwood, Am. Chem. Soc. Symposium Series 90: 242 (9178).

69. D.J. Miller, D. Haneman, Solar Energy Mat. 4: 223 (1981).

70. G.J. Houston, J.F. McCann, D. Haneman, J. Electroanalyt. Chem. 134: 37 (1982).

71. M. Cocivera, A. Darkovski, B. Love, J. Electrochem Soc. 131: 2514 (1984).

72. M.S. Kazacos, J. Electroanalyt. Chem. 148: 233 (1983).

73. R.C. Kainthla, J.F. McCann, D. Haneman, Solar Energy Mat. 7: 491 (1983).

74. K. Rajeshwar, L.Thompson, P. Singh, R.C. Kainthla, K.L. Chopra, J. Electrochem. Soc. 128: 1744 (1981).

75. R.A. Boudreau, R.H. Rauh, J. Electrochem. Soc. 130: 513 (1983).

76. A. Mondal, T.K. Chaudhuri, P. Pramanik, Solar Energy Mat.

7: 431 (1983).

77. M. Russak, J. Reichman, H. Witzke, S.K. Deb, S.N. Chen, J. Electrochem. Soc. 127: 725 (1980).

78. J. Reichman, M. Russak, J. Electrochem. Soc. 128: 2025 (1981).

79. D. Bonnet, E. Rickus in "Fourteenth IEEE Photovoltaic Specialists Conference", San Diego, California (1980).

80. C.W. Liu, J. Ohlson, D.R. Saunders, J.W. Wang, J. Electrochem. Soc. 128: 1224 (1981).

81. C.J. Liu, J.W. Wang, J. Electrochem. Soc. 129: 719 (1982).

82. G. Hodes, D. Cahen, J. Manassen, M. David, J. Electrochem. Soc. 127: 2252 (1980).

83. X.R. Xiao, H.T. Tien, J. Electrochem. Soc. 130: 55 (1983).

84. Y. Ueno, H. Minoura, T. Nishikawa, M. Tsuiki, J. Electrochem. Soc. 130: 43 (1983).

85. M. Matsumura, K.W. Frese, Private Communication.

86. A. Mackintosh, S. Wessel, F. El Guibaly, K. Colbow, Solar Energy Mat. 9: 69 (1983).

87. J.R.C. Bhardwaj, C. M. Jadhav, M.M. Taquikhan, Solar Cells 13: 293 (1984/85).

88. J.S. Curran, R. Philippe, M. Roubin, L. Mosoni, Solar Energy Mat. 9: 329 (1983).

89. M. Tomkievicz, I. Ling, W.S. Parsons, J. Electrochem. Soc. 129: 2016 (1982).

90. K.T. De Silva, D.J. Miller, D. Haneman, Solar Energy Mat. 4: 233 (1981).

91. K.W. Frese, Jr., Appl. Phys. Lett. 40: 275 (1982).

92. R. Tenne, J. Electrochem. Soc. 130: 2163 (1983).

93. J. Reichman, M.A. Russak, J. Electrochem. Soc. 131: 796 (1984).

94. R. Noufi, D. Tench, L.F. Warren, J. Electrochem. Soc. 127: 2709 (1980).

95. R. Noufi, D. Tench, L.F. Warren, J. Electrochem. Soc. 128:

2363 (1981).

96. J. Manassen, G. Hodes, D. Cahen, Proc. Electrochem. Soc. 77-6: 110 (1977).

97. S. Licht, R. Tenne, HY. Flaisher, J. Manassen, J. Electrochem. Soc. 131: 950 (1984).

98. G. Hodes, in "Energy Resources through Photochemistry and Catalysis", M. Gratzel (Ed.), Academic Press, New York, p. 432 (1983).

99. D. Cahen, G. Hodes, J. Manassen, J. Electrochem. Soc. 125: 1623 (1978).

100. H. Gerischer, J. Gobrecht, Ber. Bunsengesellschaft, Phys. Chem. 82: 520 (1978).

101. A. Heller, G.P. Schwartz, G.R. Vadimsky, S. Menezes, B. Miller, J. Electrochem. Soc. 125: 1156 (1978).

102. R.N. Noufi, P.A. Kohl, J.W. Rogers, Jr., J.M.White, A.J. Bard, J. Electrochem. Soc. 126: 949 (1979).

103. K.T.L. De Silva, D. Haneman, J. Electrochem. Soc. 127: 1554 (1980).

104. G. Hodes, J. Manassen, D. Cahen, Solar Energy Mat. 4: 373 (1981).

105. D. Lando, J. Manassen, G. Hodes, D. Cahen, J. Am. Chem. Soc. 101: 3969 (1979).

106. J.F. McCann, M.S. Kazacos, D. Haneman, Nature 289: 780 (1981).

107. N. Müller, R. Tenne, J. Electroanalyt. Chem. 130: 373 (1981).

108. G. Hodes, J. Manassen, D. Cahen, J. Electrochem. Soc. 128: 2325 (1981).

109. R. Tenne, J. Electroanalyt. Chem. 143: 113 (1983).

110. A. Heller, K.C. Chang, B. Miller, J. Electrochem. Soc. 124: 697 (1977).

111. A. Heller, K.C. Chang, B. Miller, J. Am. Chem. Soc. 100: 684 (1978).

112. K.T.L. De Silva, D. Haneman, Thin Solid Films 79: L69 (1981).

113.R. Tenne, Ber. Bunsengesellschaft, Phys. Chem. 85: 413 (1981).

114.R. Tenne, N. Müller, Y. Mirovsky, D. Lando, J. Electrochem. Soc. 130: 852 (1983).

115.J. Reichman, M.A. Russak, J. Appl. Phys. 53: 708 (1982).

116.M.A. Russak, J. Reichman, J. Electrochem. Soc. 129: 542 (1982).

117.M. Leban, unpublished results.

118.B.L. Funt, A. Mackintosh, H. Kolny, G. Watkinson, Final Report on Contract 8SU79-00131 for the Defense Research Establishment, Ottawa (1979).

119.K.W. Frese, Jr., J. Appl. Phys. 53: 1571 (1982).

120.K.W. Frese, Jr., J. Electrochem. Soc. 130: 28 (1983).

121.J.G. Simmons, in "Handbook of Thin Film Technology", L.I. Maissel, R. Glang (Eds.), McGraw-Hill Inc,New york, p. 14-6, (1970).

122.CRC Handbook of Chemistry and Physics, 59th ed.,CRC Press, E 81 (1978 -1979).

123.A.H. Nethercot, Jr., Phys. Rev. Lett. 33: 1088 (1974).

124.A. Reisman, M. Berkenblit, m. Witzen, J. Phys. Chem., 66: 2210 (1962).

125.R. Haak, D. Tench, J. Electrochem. Soc. 131: 1442 (1984).

126.R. Haak, D. Tench, M. Russak, J. Electrochem. Soc. 131: 2709 (1984).

127.K. Colbow, D.J. Harrison, B.L. Funt, J. Electrochem. Soc. 128: 547 (1981).

128.E.A. Davis, J. Non-Cryst. Solids 4: 107 (1970).

129.W.M. Sears, S.R. Morrison, J. Phys. Chem. 88: 976 (1984).

130.M.S. Kazacos, B. Miller, J. Electrochem. Soc. 127: 869 (1980).